International School for Advanced Studies

PhD course in Statistical Physiscs

Academic Year 2015/2016

On entanglement negativity in $1+1$ and $2+1$ dimensional quantum systems

Thesis submitted for the degree of

Doctor Philosophiae

October 14$^{\text{th}}$ 2016

Supervisor

Dr. Erik Tonni

Candidate

Cristiano De Nobili

"Is this the real life? Is this just fantasy?"
— Bohemian Rhapsody, *Queen*

Contents

Chapter 1

Introduction

"The best possible knowledge of a whole does not necessary include the best possible knowledge of all its parts"
Schrödinger

In classical physics the idea of entropy quantifies the extent to which we are uncertain about the exact state of a physical system or equivalently the amount of information that is missing to identify the microstate of a system from all possibilities compatible with its macrostate. Differently from classical physics, in quantum mechanics positive entropies may arise even without an objective lack of information. In contrast to thermal states this entropy does not originate from an absence of knowledge about the microstate of the systems and even at zero temperature there is a surprising non-zero entropy contribution. This entropy arise form a fundamental property of the quantum realm: *Entanglement*. Entanglement has played a crucial role in the development of quantum physics and is mainly perceived as the qualitative features of quantum theory that most strikingly distinguishes it from our classical intuition, as Schrödinger said: "I would not call that *one* but rather *the* characteristic trait of quantum mechanics, the one that enforces its entire departure from classical lines of thought " [1]. At first attached to fundamental questions regarding the nature and foundation of quantum mechanics, the concept of entanglement has recently generated an enormous interests in several fields of theoretical physics, from quantum optics and quantum information to condensed matter, from mathematical physics to high energy physics, cosmology and recently also gravity.

Going back to the origins, Einstein, Podolsky and Rosen [2] soon understood that entanglement may allow for tasks which are impossible in the classical world. The core feature of entanglement is that the local action on a subsystem of a quantum system may instantaneously condition the state of all its other parts, even if spatially far apart. The word instantaneously sounds strange since this behavior is really different from the effect of classical correlations, where a local perturbation on a subregion is limited in its propagation to the rest of the system by some maximum speed [3]. For this reason entanglement is often referred as a *spooky* non-local phenomenon. Because of this, entanglement gave rise to severe skepticisms since the early days of quantum mechanics, whose status of complete physical theory was called into question. Theories introducing some hidden variables were proposed to solve the EPR paradox formulated in [2]. When these variables were added as new parameters, an experimenter who could know their value could also exactly predict the results of single experiments without the typical uncertainty of quantum mechanics. The ignorance of this variables is then the cause of the probabilistic nature of the quantum theory. It was only after the seminal contribution of John Bell [4] in 1964 that the fundamental questions related to the existence of entangled states could be tested experimentally. In fact, under fairly general assumptions, Bell derived a set of inequalities for correlated measurements of two physical observables that any local theory should obey. The overwhelming majority of experiments done so far are in agreement with quantum mechanics thus demonstrating that quantum entanglement is physical reality and it forbids an hidden variable interpretation without nonlocalities.

1.1 Quantum Information Point of View

Entanglement has gained renewed interest with the development of quantum information science since it started to be considered as a resource in quantum information processing, as much as energy is. Entanglement can be employed to perform tasks that are utopian or extremely inefficient in a pure classical world. Quantum teleportation [5] and quantum error correcting codes [6] are just some examples. To this end, necessary criteria for any entanglement measure to be fulfilled, tools to understand how entanglement can be characterized and manipulated were evident. In particular, it is extremely important to have a way to quantify the amount of entanglement associated to the bipartition a given quantum state. This leads to the problem of defining measures of entanglement. Being considered a resource, its definition has a strong operational point of view and it is related to the possible operations that can be performed on the system. One can consider the case where a quantum state is shared by two parties, usually denoted by Alice and Bob. They are spatially separated and each of them can act on the system locally, i.e. perform any measurement that is localized in their laboratory. Any state that cannot be created with these

operations becomes a resource. In order to be a good measure of entanglement there are some requirements to be satisfied [7, 8] and other ones that may be desirable. A precise picture is still ongoing, except from some specific cases, such the pure-state entanglement of a bipartite system.

1.1.1 Quantum operations: LOCC, separable and PPT transformations

Let's come back to Alice, Bob and the quantum state they share. The Hilbert space of the full system is bipartite, i.e. $\mathcal{H} = \mathcal{H}_A \otimes \mathcal{H}_B$. They can act locally only on their own subsystem, and they are also allowed to send their outcomes through classical communication one to another. The first set of transformations are called *local operations* (LO), while the second ones *classical communications* (CC) and all together are referred by LOCC. Entanglement is defined as the resource that cannot be created by these transformations only. LOCC can modify entanglement from one type to another, but cannot create it where it did not exist before. In other words *classical correlations* are the ones that can be created by LOCC, while *quantum correlations* are those which are already present in the system and cannot be attributed by a local action on one subsystem. LOCC operations do not allow for instance the exchange of quantum information between Alice and Bob. An example of LOCC is distinguishing two pairs of two entangled qubits in a Bell state, such as below:

$$\begin{aligned} |\psi_1\rangle &= \tfrac{1}{\sqrt{2}}\left(|0\rangle_A \otimes |0\rangle_B + |1\rangle_A \otimes |1\rangle_B\right) \\ |\psi_2\rangle &= \tfrac{1}{\sqrt{2}}\left(|0\rangle_A \otimes |1\rangle_B + |1\rangle_A \otimes |0\rangle_B\right) . \end{aligned}$$

Suppose that the two-qubit system is separated, where the first qubit is given to Alice and the second is given to Bob. Assume that Alice measures the first qubit (LO), and obtains the result 0. We still do not know which Bell pair we were given, $|\psi_1\rangle$ or $|\psi_2\rangle$. Alice sends the result to Bob over a classical channel (CC), where Bob measures the second qubit (LO), also obtaining 0. Bob now knows that since the joint measurement outcome is $|0\rangle_A \otimes |0\rangle_B$, the Bell pair is $|\psi_1\rangle$.

Another example of LOCC is *teleportation*, which using entanglement it allows to transfer a quantum state from one agent to another using only measurements and classical communications.

In the standard approach to quantum evolution, a system is evolved according to unitary operators or through projective measurements which cause eigenfunction collapse. In quantum information a more general set of quantum operations is considered. It can be divided in three steps: first one adds ancilla particles, then one performs joint unitary operations and measurements on both the systems and ancillae and finally some particles may be discarded depending on the measurement outcomes. If now one has total knowledge of the outcomes, then the state corresponding to measurement outcomes k occurs with probability $p_k = \mathrm{Tr}(A_k \rho A_k^\dagger)$ and

it is given by

$$\rho_k = \frac{1}{p_k} A_k \rho A_k^\dagger \,, \tag{1.1}$$

where ρ is the initial state and A_k are the so called Kraus operators (we have that $\sum_k A_k^\dagger A_k = \mathbb{1}$). Are also possible situations when a system is interacting with the environment and all measurement outcomes might not be accessible, so that the resulting system might be in a mixed states. At the end, the result of any operation on the density matrix ρ of the system can be described as follows

$$\rho_k = \sum_j \frac{1}{p_k} A_{k,j} \rho A_{k,j}^\dagger \,, \tag{1.2}$$

where the index k refers to the measuring operations, while the index j to the trace preserving ones.

After this overview of generalized quantum operations, we can be more precise in determining which operations are implementable by LOCC. A mathematical characterization of this kind of operations is still an open problem. A larger class of operations, which can be defined mathematically are called *separable operations*. They can be written in terms of Kraus operator with a product decomposition

$$\rho_k = \frac{A_k \otimes B_k \, \rho \, A_k^\dagger \otimes B_k^\dagger}{\mathrm{Tr}\left(A_k \otimes B_k \, \rho \, A_k^\dagger \otimes B_k^\dagger\right)} \,, \tag{1.3}$$

with $\sum_k A_k^\dagger A_k \otimes B_k^\dagger B_k = \mathbb{1} \otimes \mathbb{1}$. Since the individual action of Alice and Bob can be joined into a product of Kraus operators, any LOCC can be cast in the form of separable operation. However, it was demonstrated in [9] that the converse is not true and it was shown that exist separable operations which requires a finite amount of quantum communication to implement it. Therefore we have that LOCC $\subset$ separable.

Another class of quantum operations, called *positive partial transpose preserving operations* (PPT) [10, 11], are even more general, as we will soon see. They are extremely important for the definitions of the logarithmic negativity. Once a local orthonormal basis $|e_i^A, e_j^B\rangle$ is given, the density matrix can be expressed as

$$\rho = \sum_{ijkl} \rho_{ij,kl} \, |e_i^A, e_j^B\rangle\langle e_k^A, e_l^B| \,. \tag{1.4}$$

Its partial transposition with respect to the subsystem B is defined as the following matrix

$$\rho^{T_B} = \sum_{ijkl} \rho_{ij,kl} \, |e_i^A, e_l^B\rangle\langle e_k^A, e_j^B| \,, \tag{1.5}$$

While the density matrix ρ is a positive definite operator, it is not guaranteed that its partial transpose is also positive definite. The positivity of the partial transpose is a

necessary condition for a state to be separable [12–14]. Since there exist states with positive partial transpose that are not separable, the converse in not true. Besides, it is possible to prove that LOCC $\subset$ separable $\subset$ PPT. Therefore if one may find bounds on PPT operations, they will be achieved also by LOCC ones.

1.1.2 Entanglement measures: basic properties

What is a good measures to quantify entanglement? It is possible to provide some general statements which are valid regardless of what your favorite use of entanglement is.

Separable state contain no entanglement. A state $\rho_{AB...}$ of many parties $A, B, ...$ is said to be *separable* [15], if it can be written as

$$\rho_{AB...} = \sum_i p_i \, \rho_A^i \otimes \rho_B^i \otimes \cdots , \tag{1.6}$$

with p_i a probability distribution. These states can be created by LOCC. For instance, Alice samples from the distribution p_i, communicates to all other parties of the outcome i, then each party X locally creates its ρ_X^i and throws out the information about the outcome i. Any separable state can be converted in any other separable state by LOCC only [16] and hence they are all locally equivalent. Their correlations are classical and so they contain no entanglement.

The entanglement present in a state does not increase under LOCC transformations. By LOCC one can only create separable states and therefore LOCC cannot create entanglement from an unentangled state. In other words, from a quantum state ρ one can perform some LOCC and obtain another quantum state σ which is at least as entangled as ρ [17–19]. Moreover, since local unitary operations are reversible, any two states connected by them must have the same entanglement.

There are maximally entangled states. Since some states are more entangled than others, one can wonder whether there is a *maximally entangled state*. It is not easy to prove its existence in general, but for bipartite systems such state exists. Suppose to have a bipartite system consisting of two fixed d-dimensional subsystems. Any pure state which is locally equivalent to

$$|\Psi^{max}\rangle = \frac{|0,0\rangle + |1,1\rangle + ... + |d-1,d-1\rangle}{\sqrt{d}} , \tag{1.7}$$

is maximally entangled. From this state is possible, using only LOCC, to prepare any pure or mixed state of two d-dimensional systems. It is worth noticing that the non existence of an equivalent statement in multi-particle systems is the reason behind the difficulty in expressing a theory of multi-particle entanglement.

The problem of finding an order among quantum states according to their entanglement is very difficult. It was proven that there are incomparable states [20] and

LOCC can only induce a partial order in the set of quantum states. An operational approach is difficult to follow and the quantum information community replaced it with an axiomatic one [18]. From this point of view one can define real valued functions that satisfy the basic properties of entanglement listed above and at the same time quantify the amount of entanglement present in a quantum state. Various measures, some with physical interests others purely axiomatic, have been proposed over the last years, such as the entanglement distillation [17] and the entanglement cost [6, 17, 21, 22].

Now we will present some basic axioms that any measure of entanglement should satisfy.

1. A *bipartite* entanglement measure is a function $E(\rho)$ from density matrices into positive real numbers: $\rho \to E(\rho) \in \mathbb{R}^+$. The normalization is usually chosen such that the maximally entangled state (1.7) has $E(|\Psi^{max}\rangle) = \log d$.

2. If ρ is separable, then $E(\rho) = 0$.

3. E does not increase on average under LOCC

$$E(\rho) \geq \sum_i p_i E\left(\frac{A_i \rho A_i^\dagger}{\operatorname{Tr} A_i \rho A_i^\dagger}\right), \tag{1.8}$$

   where the A_i are Kraus operators which describe some LOCC task and $p_i = \operatorname{Tr} A_i \rho A_i^\dagger$ is the probability of obtaining the outcome i.

4. For pure state $\rho = |\Psi\rangle\langle\Psi|$ the measure becomes the entanglement entropy, which we are going to define in the next section.

Any function satisfying the first three items is usually called *entanglement monotone*. In quantum information an *entanglement measure* is a function which fulfills item $1, 2, 4$ and is monotone under any deterministic LOCC transformation

$$E(\rho) \geq E(\sum_j V_j \rho V_j^\dagger)\,. \tag{1.9}$$

There is some confusion in the literature about these two definitions, but we refer to the convention of [7, 8]. Other convenient additional requirements for an entanglement measure are sometimes required, such as convexity, additivity and continuity but we will not enter into these details. The main reason to add them is for mathematical convenience. About item 3, it is worth noticing that monotonicity is requested on average. This means that a particular measurement outcome may correspond to an increase of the entanglement. However this process cannot be used to systematically increase the amount of resources of the system. This property is less fundamental

than the deterministic version, in the sense that it describes the entanglement of an ensemble $\{p_k, \rho_k\}$, which is a less operational notion than the notion of a state, but is something mathematically easy to deal with. The monotonicity under LOCC operations implies that for any separable states, $E(\rho)$ takes a constant value, which is its minimal and we can set to zero without loss of generality [16].

Using this axiomatic approach, several other measures of entanglement has been defined satisfying monotonicity under LOCC transformations. A satisfactory list can be found in [7, 8]. We have understood that there is not a unique way to calculate the amount of entanglement: different states may contain different form of it and different measures quantify the amount of entanglement which is useful for different specific operational tasks.

1.2 Entanglement Entropy and Rényi Entropies

Given a quantum system in its ground state $|\Psi\rangle$, we want to measure the amount of entanglement associated to a bipartition $\mathcal{H} = \mathcal{H}_A \otimes \mathcal{H}_B$ of the Hilbert space (in Fig. 1.1 we show a spatial bipartition in two spatial dimensions). Entanglement entropy can quantify the resource, as previously explained. The key object to introduce is the reduced density matrix of the subsystem A, which is obtained by tracing out all the degrees of freedom that belong to B, i.e.

$$\rho_A = \mathrm{Tr}_B\, \rho\,, \tag{1.10}$$

where $\rho = |\Psi\rangle\langle\Psi|$ is the density matrix of the full system. The *entanglement entropy* is defined as the Von Neumann entropy associated to ρ_A [23–25]

$$S_A = -\,\mathrm{Tr}(\rho_A \log \rho_A)\,. \tag{1.11}$$

Similarly, we could have introduced S_B for the complement. By using the Schmidt decomposition one can show that $S_A = S_B$. The entanglement entropy can also be seen as the Shannon entropy of the eigenvalues of the reduced density matrix. Entanglement entropy is a measure of entanglement and in addition to the properties $(1-4)$ listed in §1.1.2, it is additive for product states ($S_A(\rho^{\otimes n}) = nS_A$). Besides, it satisfies also two really important inequalities [26, 27], subadditivity

$$S_{AB} \leq S_A + S_B \quad \forall A, B\,, \tag{1.12}$$

and strong subadditivity

$$S_{ABC} + S_B \leq S_{AB} + S_{BC} \quad \forall A, B, C \tag{1.13}$$

where S_{AB} is the entanglement entropy of $A \cup B$ and S_{ABC} of $A \cup B \cup C$.

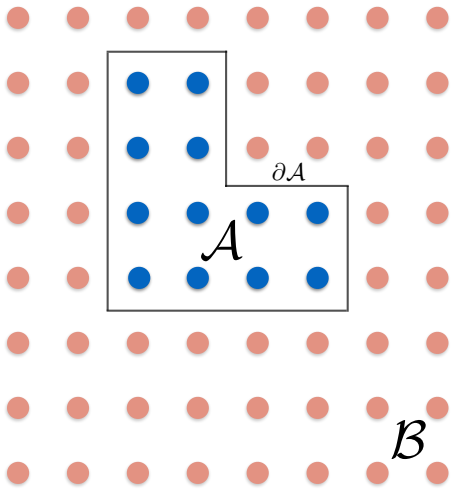

Figure 1.1: A discrete latticed quantum system with a Hilbert space at every site. We divided the lattice in two regions, A and B, and consequently the total Hilbert space can be factorized as $\mathcal{H} = \mathcal{H}_A \otimes \mathcal{H}_B$.

Moreover, it is also satisfied the Araki-Lieb inequality

$$|S_A - S_B| \leq S_{AB} \quad \forall A, B\,. \tag{1.14}$$

It is important to define also *Rényi entropies* [28]

$$S_A^n = \frac{1}{1-n} \operatorname{Tr}_A \rho_A^n\,, \tag{1.15}$$

where n is a non-negative real number. While it is natural to expect that the full set of Rényi entropies carries complete information about the pattern of correlations of a state, they do not have a simple operational meaning.

Rényi entropies are also entanglement monotone on pure state, in the range $0 \leq n \leq 1$, but they do not reduce to the entanglement entropy when ρ is pure [16]. It is also worth mentioning that Rényi entropies do not satisfy (1.12) and (1.13). We will see that, in order to compute entanglement entropy in quantum field theory, Rényi entropies with integer n are extremely important. Indeed, entanglement entropy can be recovered as the limit $n \to 1^+$ of the Rényi entropies (see §1.5).

1.3 Logarithmic Negativity

Entanglement entropy is a good measure to quantify entanglement in bipartite pure states, but what about mixed states. Is there a good measure for them? During the

years many measures for bipartite entanglement for mixed states have been proposed.

Entanglement of formation is one of the most important [6]. It is defined as the minimal average entanglement over all possible pure state decompositions of ρ

$$E_F(\rho) = \inf_{p_i,|\Psi_i\rangle} \{ \sum_i p_i S_A(|\Psi_i\rangle\langle\Psi_i|) \ : \ \rho = \sum_i p_i |\Psi_i\rangle\langle\Psi_i| \} \, . \tag{1.16}$$

It quantifies the asymptotic pure-state entanglement required to create ρ. Other measures are the *entanglement cost* E_C, which is a regularized version of $E_F(\rho)$, and the *entanglement distillation* E_D. The latter quantifies the asymptotic pure-state entanglement that can be extracted from ρ, by means of LOCC. All these measures are very difficult to compute for many-body systems, since they involve variational expressions.

The measure of bipartite mixed states which will play the major role in this thesis is negativity, mainly introduced in [29–31]. With respect to other measure, it is computable also for many-body quantum systems. The idea underline its introduction was to find out a quantitative version of *Peres' criterion for separability* [12–14]. If a state is separable, then its partial transpose ρ^{T_B}, defined in (1.5), with respect to the subsystem B is a positive definite operator

$$\rho \text{ is } \textit{separable} \quad \Rightarrow \quad \rho \text{ is } PPT \tag{1.17}$$

Except for very specific cases, the positivity of ρ^{T_B} is not a sufficient condition for separability. There exist entangled states with a positive partial transpose known as bound entangled states [14]. The only cases where it is a necessary and sufficient condition are for the smallest non trivial finite dimensional systems with dimension $2 \otimes 2$ and $2 \otimes 3$ [32], and for oscillators in a Gaussian state when A contains only one oscillator and B whatever [33]. Negativity essentially measures the degree to which ρ^{T_B} fails to be positive counting its negative eigenvalues

$$\mathcal{N}(\rho) = \frac{||\rho^{T_B}||_1 - 1}{2} \, , \tag{1.18}$$

where $||M||_1 = \mathrm{Tr}\sqrt{M^\dagger M}$ is the trace norm, which for Hermitian matrices can be computed as the sum of the modulus of eigenvalues λ_i of M. Since the sum of all eigenvalues of ρ^{T_B} is 1, $\mathcal{N}(\rho)$ corresponds to the absolute value of the sum of only the negative eigenvalues of ρ^{T_B}, as follows

$$\mathrm{Tr}\,|\rho^{T_2}| = \sum_i |\lambda_i| = \sum_{\lambda_i<0} |\lambda_i| + \sum_{\lambda_i>0} |\lambda_i| = 1 + 2\sum_{\lambda_i<0} |\lambda_i| \tag{1.19}$$

It was proven that negativity is an entanglement monotone under both deterministic and stochastic LOCC [31, 34–36] and it is convex. Unfortunately, it does not have a clear operational interpretation and it is not additive.

This last issue can be overcome simply defining the *logarithmic negativity*

$$\mathcal{E}(\rho) = \log ||\rho^{T_B}||_1 \,, \tag{1.20}$$

which is still an entanglement monotone and it is also additive. For both negativity and logarithmic negativity, it can be also shown the monotonicity under the more general class of PPT operations [34]. Logarithmic negativity does not respect the 4th item of subsection (1.1.2) and so it fails to reduce to the entanglement entropy on pure states. We will often refer to the logarithmic negativity as the entanglement negativity or simply negativity.

It is interesting to note that negativity satisfies a *disentangling theorem*. Let us consider a tripartite system ABC in a pure state with density matrix ρ_{ABC} and denote the negativity between A and BC as $\mathcal{N}_{A|BC}$ and the negativity between A and B as $\mathcal{N}_{A|B}$. It was recently proved in [37] that a partitioning of B into B_1 and B_2, such that the state of the whole system can be factorized as

$$\rho_{ABC} = \rho_{AB_1} \otimes \rho_{B_2C} \,, \tag{1.21}$$

exists if and only if $\mathcal{N}_{A|BC} = \mathcal{N}_{A|B}$. As a consequence of this theorem, the negativity $\mathcal{N}_{A|C}$ is zero. Equivalently the reduced density matrix obtained from ρ_{ABC} by tracing out B factorizes: $\rho_{AC} = \rho_A \otimes \rho_C$. Furthermore, in this particular case, one has the saturation of a monogamy inequality for the square of the negativity previously proved by [38] for systems of three qubits

$$\mathcal{N}^2_{A|BC} \geq \mathcal{N}^2_{A|B} + \mathcal{N}^2_{A|C} \tag{1.22}$$

In [37] it is conjectured that this inequality is true in general. Numerical results support this claim, but a proof is still lacking. It is important to underline that this inequality does not hold for negativity itself.

1.4 A Bird Eye View on Conformal Field Theory

In this section we review some very basics facts of Conformal Field Theories (CFT) [39]. The study of CFT has captured the attention of physicists and mathematicians for several years because of its wide application from string theory (where CFT naturally arises to describe the ground states of strings) to statistical physics and the study of critical phenomena, where the conformal symmetry may arise as an extended symmetry of scale invariance and Lorentz symmetry.

In general, when we are close to the quantum critical point, the correlation length of a system, which is the only relevant scale for the long-distance physics, behaves like

$$\xi \sim \frac{1}{|g - g_c|^\nu} \tag{1.23}$$

where g is a tunable experimental parameter of our system described by the Hamiltonian $H(g)$ (e.g. the magnetic field in the transverse direction in the case of the Ising model [40]), while g_c is the critical value corresponding to a quantum phase transition. The way the correlation length diverges is described by the critical exponent ν. When ξ diverges the system becomes *scale invariant*. The *universality hypothesis* states that some physical properties (that are called universal), close to the phase transition, do not depend on microscopic details, but only on global proprieties, such as symmetries and dimensionality. A fundamental result of two-dimensional CFT [41] is that the universality class is characterized just by a single quantity called central charge. For the minimal models, it assumes only some discrete values

$$c = 1 - \frac{6}{m(m+1)}\,, \qquad \text{with } m = 3, 4, \cdots, \infty \tag{1.24}$$

The Ising universality class has $c = 1/2$, the free boson $c = 1$ and for instance the three state Potts model $c = 4/5$. There exist also models of physical interest which correspond to different values from the allowed ones by Eq. (1.24).

In this thesis, we will treat one and two dimensional extended quantum systems where conformal symmetry may arise as an extended symmetry of scale invariance and Lorentz symmetry. Our systems are made by discrete variables at a critical point. Conformal symmetry is a property of continuous theories, which can be described by a Quantum Field Theory (QFT). Therefore, our discrete system has to be thought in the limit of many degrees of freedom and of a correlation length much larger than the lattice spacing $\xi \gg a$. This limit washes away the microscopic details so that *universality* arises: this means that many different lattice systems, with different features and properties, may display the same behavior in some critical regime, and therefore may be described by the same QFT. It is important to stress that from the continuum description of our many-body system we can only recover universal properties, like the central charge and the critical exponents.

As we will shortly see, the Hilbert space and the operator content of a conformally invariant theories in two dimensions are strongly conditioned by the symmetry. The classification of all CFT, even if still an extraordinary task, seems much more easy than the classification of all the QFT. This is a crucial step towards the classification of all the universality class. There are many CFTs known in two dimensions, among which there are the minimal models, the $c = 1$ compactified boson, Liouville theory, and many others. In the following we will try to give some fundamental notions on CFT. A detailed analysis of the various aspects of CFT can be found for example in Refs. [41–43], which contain also all the relevant references to the original literature.

1.4.1 Conformal invariance and primary fields

Let us consider a general d-dimensional spacetime endowed with a flat metric $g_{\mu\nu}(x) = \eta_{\mu\nu}$ with signature $(d-1,1)$. The metric tensor $g_{\mu\nu}$ transforms covariantly under a change of coordinates $x \to x'$. By definition, a *conformal transformation* is a coordinate transformation that leaves the metric invariant up to a scale change

$$g_{\mu\nu}(x) \to g'_{\mu\nu}(x') = \Lambda(x) g_{\mu\nu}(x). \tag{1.25}$$

These are the coordinate transformations that preserves the angle $v \cdot u/(v^2 u^2)^{1/2}$ between two vectors v, w, where $v \cdot u = g_{\mu\nu} v^\mu u^\nu$. It is worth noticing that the Poincaré group, which is the semidirect product of translation and Lorentz transformations of flat space, is always a subgroup of the conformal group since it leaves the metric invariant ($g'_{\mu\nu} = g_{\mu\nu}$).

An infinitesimal coordinate transformations $x^\mu \to x^\mu + \epsilon^\mu$, is conformal if it satisfies the following relation,

$$\partial_\mu \epsilon_\nu + \partial_\nu \epsilon_\mu = \frac{2}{d} (\partial \cdot \epsilon) \eta_{\mu\nu}. \tag{1.26}$$

In $d > 2$, this constraint forces $\epsilon^\mu(x)$ to be at most quadratic in x. Apart from the usual translations $\epsilon^\mu = a^\mu$, rotations $\epsilon^\mu = \omega^\mu{}_\nu x^\nu$ and dilatations $\epsilon^\mu = \lambda x^\mu$, the constraint (1.26) allows also for the special conformal transformations $\epsilon^\mu = b^\mu x^2 - 2x^\mu b \cdot x$. For each of these infinitesimal transformations it is possible to write the corresponding finite version by exponentiation, the generators of the algebra and their commutation relations. For a generic conformal transformation, the number of free parameters is $(d+1)(d+2)/2$.

From now on, our attention will be focused on two dimensional conformal field theories in Euclidean signature $g_{\mu\nu} = \delta_{\mu\nu}$, which can be recovered form the Lorentzian signature $(1,1)$ with the usual Wick rotation to imaginary time. In two dimensions, the constraint (1.26) reduces to the Cauchy-Riemann equation

$$\partial_1 \epsilon_1 = \partial_2 \epsilon_2, \qquad \partial_1 \epsilon_2 = -\partial_2 \epsilon_1. \tag{1.27}$$

This means that any conformal transformation is an analytic transformation $z \to f(z)$, $\bar{z} \to \bar{f}(\bar{z})$, of the coordinates $z = x^1 + \mathrm{i}x^2$, $\bar{z} = x^1 - \mathrm{i}x^2$. The complex coordinate z and $\bar{z}$ in Euclidean signature correspond to the light-cone coordinates $x \pm t$ in Minkowski space. If we consider all the analytic functions on the plane satisfying (1.27) without further specification, since they can all be expanded in Laurent series, we can take the following generators,

$$\ell_n = -z^{n+1} \partial_z, \qquad \bar{\ell}_n = -\bar{z}^{n+1} \partial_{\bar{z}}, \qquad n \in \mathbb{Z}, \tag{1.28}$$

which satisfy the following commutation relations

$$\big[\ell_m, \ell_n\big] = (m-n)\ell_{m+n}, \qquad \big[\bar{\ell}_m, \bar{\ell}_n\big] = (m-n)\bar{\ell}_{m+n}. \tag{1.29}$$

The ℓ_n's and the $\bar{\ell}_n$'s commute among each others, therefore the algebra is the direct sum of a holomorphic and an antiholomorphic subalgebras. The coordinates z and $\bar{z}$ are considered independent variables in $\mathbb{C}$, and only at the end the physical condition $\bar{z} = z^*$ is imposed.

Even if all the transformations satisfying Eq. (1.26) are locally analytic, they may not be so globally, due to singularities either at $z \to 0$ or at $z \to \infty$. In two dimension the global conformal group is defined to be the group of conformal transformation that are well-defined and invertible on the Riemann sphere. Therefore, the global conformal transformations correspond to well defined, invertible, globally analytic functions, whose generators are $\{\ell_0, \ell_{\pm 1}\}$, and $\{\bar{\ell}_0, \bar{\ell}_{\pm 1}\}$. This means that the infinitesimal globally analytic transformations are the ones at most quadratic in z, as discussed for the $d > 2$ case. Notice that ℓ_{-1} and $\bar{\ell}_{-1}$ generate the translations, $\mathrm{i}(\ell_0 - \bar{\ell}_0)$ generates the rotations, $\ell_0 + \bar{\ell}_0$ the dilatations, and finally ℓ_1 and $\bar{\ell}_1$ the special conformal transformations. The finite versions of these transformations are the only bijective biholomorphic automorphisms of the Riemann sphere, the so called Möbius transformations

$$z \to \frac{az + b}{cz + d}\,, \tag{1.30}$$

for a, b, c, $d \in \mathbb{C}$ and $ad - bc = 1$. This is the group $SL(2, \mathbb{C})/\mathbb{Z}_2 \approx SO(3, 1)$, where the quotient by $\mathbb{Z}_2$ is due to the fact that (1.30) is unaffected by taking all of a, b, c, d to minus themselves.

All locally analytic transformations satisfying Eq. (1.27) but without being Möbius (1.30), are still of great importance. From them we can define some fields which behave covariantly under these transformations. A *primary field* $\Phi(z, \bar{z})$ is defined such that the element $\Phi(z, \bar{z})\mathrm{d}z^h \mathrm{d}\bar{z}^{\bar{h}}$ is invariant, for some *conformal weight* $(h, \bar{h})$. Under a conformal transformation the primary fields transform as follows,

$$\Phi(z, \bar{z}) \to \left(\partial_z f\right)^h \left(\partial_{\bar{z}} \bar{f}\right)^{\bar{h}} \Phi\left(f(z), \bar{f}(\bar{z})\right). \tag{1.31}$$

One usually defines also quasi-primary operators, which transform as in (1.31) only for global conformal transformations. The quasi-primaries can be defined in an analogous way also in higher dimensional CFT.

The transformation properties (1.31) of the primaries put severe constraints on their two and three-point functions. Let us focus first on the two-point function of two primaries, $G^{(2)}(z_i, \bar{z}_i) = \langle \Phi_1(z_1, \bar{z}_1)\Phi_2(z_2, \bar{z}_2)\rangle$. Translational invariance implies that $G^{(2)}$ is a function of $z_{12} = z_1 - z_2$ and $\bar{z}_{12} = \bar{z}_1 - \bar{z}_2$, while rotational and scale invariance implies that $G^{(2)} \sim 1/\left(z_{12}^{h_1+h_2} \bar{z}_{12}^{\bar{h}_1+\bar{h}_2}\right)$. Finally, invariance under special conformal transformations fixes $h_1 = h_2 \equiv h$ and $\bar{h}_1 = \bar{h}_2 \equiv \bar{h}$. Putting all together, global conformal invariance forces the form of the two-point function of primaries to be

$$G^{(2)}(z_i, \bar{z}_i) = \frac{1}{z_{12}^{2h}\, \bar{z}_{12}^{2\bar{h}}}. \tag{1.32}$$

Notice that conformal invariance does not fix the proportionality constant in front of the last expression. This is instead fixed by the field normalization, which is uninteresting and we can choose it such that $G^{(2)}$ takes the form (1.32). Similar arguments lead to the following expression for the three-point function $G^{(3)} = \langle \Phi_1 \Phi_2 \Phi_3 \rangle$,

$$G^{(3)}(z_i, \bar{z}_i) = C_{123} \frac{1}{z_{12}^{2(h_1+h_2-h_3)} z_{23}^{2(h_2+h_3-h_1)} z_{13}^{2(h_1+h_3-h_2)}} \tag{1.33}$$

In the case of the three-point function we cannot fix the proportionality constant, since the fields are already normalized such that (1.32) is valid. This constant is a crucial model dependent quantity called structure constant.

At this stage, it might seem that conformal invariant theories are rather trivial since their Green functions thus far considered are entirely determined up to a constant. However, the N-point function for $N \geq 4$ cannot be fixed by conformal invariance only. Indeed, with four points we can construct invariant ratios under global conformal transformations, for example $x = z_{12} z_{23}/(z_{13} z_{24})$, and the corresponding $\bar{x}$. Therefore the dependence of the four-point function on such invariant ratios cannot be fixed by general argument, and we can write for example

$$G^{(4)}(z_i, \bar{z}_i) = \left(\frac{z_{13} z_{24}}{z_{12} z_{14} z_{23} z_{34}} \right)^{2h} \mathcal{F}(x, \bar{x}). \tag{1.34}$$

Conformally invariant theories are usually quantized by compactifying the 'spatial' Euclidean coordinate σ on a cylinder parametrized by the complex coordinate $\zeta = \tau + \mathrm{i}\sigma$ and $\bar{\zeta} = \tau - \mathrm{i}\sigma$. With the conformal map $\zeta \to z = \exp(\tau + \mathrm{i}\sigma)$ the cylinder is mapped onto the complex plane parametrized by $(z, \bar{z})$. Surfaces at equal time on the cylinder are mapped in the plane to circles centered in the origin, the origin $z = 0$ is therefore the infinite past, and the point at infinity $z = \infty$ is the infinite future. Hence, time and space translations on the cylinder correspond respectively to dilatations and rotations on the plane. Thus, the dilatation operator on the plane can be seen as the Hamiltonian of the system, while the linear momentum is given by the rotation operator.

1.4.2 Stress energy tensor and operator product expansion

The *stress-energy tensor* $T_{\mu\nu}$ plays a fundamental role in CFT. In general QFT, under an arbitrary change of coordinates $x^\mu \to x^\mu + \epsilon^\mu$, the action changes as follows,

$$\delta S = \frac{1}{2} \int \mathrm{d}^d x \, T^{\mu\nu} \left(\partial_\mu \epsilon_\nu + \partial_\nu \epsilon_\mu \right), \tag{1.35}$$

where we assumed that $T_{\mu\nu}$ is symmetric, which is always true for Lorentz invariant theories. Using Eq. (1.26), we see that for a conformal transformation

$$\delta S = \frac{1}{d} \int \mathrm{d}^d x \, T^\mu{}_\mu \partial_\rho \epsilon^\rho \,. \tag{1.36}$$

Thus the conformal invariance implies $T^{\mu}_{\mu} = 0$ at classical level.

The components of the stress-energy tensor on the complex plane parametrized by $z = x_1 + \mathrm{i}x_2$ are given by $T_{zz} = \frac{1}{4}\big(T_{22} - 2\mathrm{i}T_{12} - T_{11}\big)$, $T_{\bar{z}\bar{z}} = \frac{1}{4}\big(T_{22} + 2\mathrm{i}T_{12} - T_{11}\big)$ and $T_{z\bar{z}} = T_{\bar{z}z} = \frac{1}{4}\big(T_{11} + T_{22}\big)$. Using the traceless condition, $T_{z\bar{z}} = 0$, and imposing the conservation law $\partial_\mu T^{\mu\nu} = 0$, we can also show that $\partial_{\bar{z}} T_{zz} = \partial_z T_{\bar{z}\bar{z}} = 0$. Therefore, one defines the holomorphic and antiholomorphic components of the stress-energy tensor, respectively $T(z) \equiv T_{zz}(z)$ and $\overline{T}(\bar{z}) = T_{\bar{z}\bar{z}}(\bar{z})$. It is also possible to write down the set of Ward identities related to translational, rotational and scale invariance in a holomprphic form. For any product of n primary fields, the conformal Ward identities are given by

$$\begin{aligned}\langle T(z)\Phi_1(w_1,\bar{w}_1)\Phi_2(w_2,\bar{w}_2)\ldots\Phi_n(w_n,\bar{w}_n)\rangle = \\ \sum_{i=1}^{n}\left(\frac{h_i}{(z-w_i)^2} + \frac{1}{z-w_i}\partial_{w_i}\right)\langle\Phi_1(w_1,\bar{w}_1)\Phi_2(w_2,\bar{w}_2)\ldots\Phi_n(w_n,\bar{w}_n)\rangle\ ,\end{aligned} \tag{1.37}$$

where h_i is the conformal weight.

Another important ingredient is the operator product expansion (OPE), namely the representation of the product of two local operators as a (possibly infinite) sum over the local operators of the theory,

$$A(x)B(y) \sim \sum_i c_i(x-y)O_i(y), \tag{1.38}$$

where the O_i's are a complete set of regular local operators, and the c_i are (singular) numerical coefficient. When two local fields at position x and y respectively, approach one another $x \to y$, singularities may in general appear, and they must be encoded in the coefficients $c_i(x-y)$. For two-dimensional CFT, we can choose a basis of fields with fixed conformal weight, and one finds

$$\Phi_i(z,\bar{z})\Phi_j(w,\bar{w}) \sim \sum_k \frac{C_{ijk}}{(z-w)^{h_i+h_j-h_k}(\bar{z}-\bar{w})^{\bar{h}_i+\bar{h}_j-\bar{h}_k}}\Phi_k(w,\bar{w}). \tag{1.39}$$

When the Φ_i's are normalized such that the two-point function is given by Eq. (1.32), by using (1.39) in (1.33) for any two of the z_i's getting close one to the other, it is easy to see that the C_{ijk} appearing in the OPE and the ones appearing in the three-point functions are the same. The conformal Ward identities of Eq. (1.37) tell us the singular behavior of primary fields approaching the stress-energy tensor, therefore we can read off the divergent part of their OPE,

$$T(z)\Phi(w,\bar{w}) \sim \frac{h}{(z-w)^2}\Phi(w,\bar{w}) + \frac{1}{z-w}\partial_w\Phi(w,\bar{w}) + \text{regular terms}, \tag{1.40}$$

and analogously for $\overline{T}(\bar{z})\Phi(w,\bar{w})$.

1.4.3 Central charge, Virasoro algebra and the structure of the Hilbert space

As for the OPE of the holomorphic component of the stress-energy tensor one finds that

$$T(z)T(w) = \frac{c/2}{(z-w)^4} + \frac{2}{(z-w)^2}T(w) + \frac{1}{z-w}\partial_w T(w), \tag{1.41}$$

and analogously for the antiholomorphic component. The constant c is called the *central charge*, it cannot be fixed by symmetry requirements only and it is indeed theory dependent. The presence of the central charge term in Eq. (1.41) means that the energy-momentum tensor does not transform as a primary operator. Indeed under a conformal transformation, we have

$$T(z) \to \left(\frac{\partial w}{\partial z}\right)^2 T(w) + \frac{c}{12}\{w, z\}, \tag{1.42}$$

where $\{w, z\}$ is the Schwartzian derivative.

We can define a mode expansion of the stress-energy tensor, by expanding in Laurent series

$$T(z) = \sum_{n\in\mathbb{Z}} z^{-n-2} L_n, \qquad \overline{T}(\bar{z}) = \sum_{n\in\mathbb{Z}} \bar{z}^{-n-2} \bar{L}_n, \tag{1.43}$$

which can be inverted by

$$L_n = \oint \frac{\mathrm{d}z}{2\pi\mathrm{i}} z^{n+1} T(z), \qquad \bar{L}_n = \oint \frac{\mathrm{d}\bar{z}}{2\pi\mathrm{i}} \bar{z}^{n+1} \overline{T}(\bar{z})\,, \tag{1.44}$$

where the integral are performed over some circle of fixed radius and our sign convention is such that dz and $d\bar{z}$ integrations are taken in the counter-clockwise sense. The algebra of their commutators turns out to be exactly the one of the classical algebra, Eq. (1.28), a part for some terms proportional to the conformal anomaly,

$$\big[L_n, L_m\big] = (n-m)L_{n+m} + \frac{c}{12}(n^3 - n)\delta_{n+m,0}, \tag{1.45a}$$

$$\big[\bar{L}_n, \bar{L}_m\big] = (n-m)\bar{L}_{n+m} + \frac{\bar{c}}{12}(n^3 - n)\delta_{n+m,0}, \tag{1.45b}$$

$$\big[L_n, \bar{L}_m\big] = 0. \tag{1.45c}$$

These commutators describe two copies of an infinite dimensional algebra, called the *Virasoro algebra*. The modes L_n and $\bar{L}_n$ generate the conformal transformations on the Hilbert space, and in particular, as for the classical algebra, $L_0 + \bar{L}_0$ generates dilatation (and it is therefore proportional to the Hamiltonian) and $\mathrm{i}(L_0 - \bar{L}_0)$ generates rotations (and correspond to the linear momentum).

The modes of the stress-energy tensor play the role of ladder operators on the states of the conformal theory. The Hilbert space, albeit very intricate, shows some peculiar features common to all CFT. The vacuum $|0\rangle$ is defined by requiring that it is annihilated by all modes with index $n \geqslant -1$,

$$L_n |0\rangle = 0, \qquad \bar{L}_n |0\rangle = 0, \qquad n \geqslant -1. \tag{1.46}$$

This implies that the vacuum is invariant under any conformal transformation, and that the vacuum expectation values of $T(z)$ and $\overline{T}(\bar{z})$ vanish. When we act on the vacuum with primary fields $|h, \bar{h}\rangle \equiv \Phi(0,0)|0\rangle$ we get the eigenstates of the dilatation operator, and hence of the Hamiltonian. These states are called *highest weight states*,

$$L_0 |h, \bar{h}\rangle = h |h, \bar{h}\rangle , \qquad \bar{L}_0 |h, \bar{h}\rangle = \bar{h} |h, \bar{h}\rangle . \tag{1.47}$$

The eigenvalue of the dilatation operator $\Delta = h + \bar{h}$ is called the *scaling dimension*, while the eigenvalue of the momentum operator is the *conformal spin* of the field, $s = h - \bar{h}$. In virtue of the Virasoro algebra, $L_n |h, \bar{h}\rangle = 0$ and $\bar{L}_n |h, \bar{h}\rangle = 0$ for $n > 0$, the modes of the stress-energy tensor with $n < 0$ can be successively applied on a highest weight state to build a whole family of *descendant states* above it

$$|n_1, \ldots, n_k; h, \bar{h}\rangle = L_{-n_1} L_{-n_2} \ldots L_{-n_k} |h, \bar{h}\rangle , \qquad n_j \geqslant 1. \tag{1.48}$$

By using the Virasoro algebra (1.45) it is straightforward to see that they are still eigenstates of the dilatation and rotation generators, $L_0 |\{n_j\}; h, \bar{h}\rangle = (h+N) |\{n_j\}; h, \bar{h}\rangle$, and their conformal weight is increased with respect to the primary of an integer $N = \sum_j n_j$. The descendant states are eigenstates of the Hamiltonian and are organized in levels, labeled by the integer N. Every *conformal family*, generated by a highest weight state and its descendants, is closed under the action of the generators of the conformal transformations, and therefore corresponds to a realization of the Virasoro algebra. The corresponding subspace of the Hilbert space is usually called a *Verma module*. Primaries and descendants are all the eigenstates of the Hamiltonian and form a basis for the full Hilbert space.

Primary operators Φ are in one-to-one correspondence with highest weight states $|h, \bar{h}\rangle$. In the same way, for any descendant state we can define the corresponding descendant field, as the one that creates the state when applied to the vacuum. It can be seen that correlation functions involving descendant fields can be obtained by applying a specific set of differential operators to the correlation functions of their corresponding primaries.

The structure of the Hilbert space described so far is typical of every CFT, but specific theories can have different features. For example, the *minimal models* are characterized by a finite number of Verma modules, which makes the structure of the Hilbert space particularly regular. On the contrary, in general the number of

realizations of the Virasoro algebra is infinite. For example, the set of primaries of the free massless scalar boson is in one-to-one correspondence with the real numbers. However, if we compactify the target space of the boson on a circle of radius R, thus identifying $\phi \sim \phi + 2\pi R$, the set of primaries is still infinite, but discrete.

1.5 Entanglement Entropy in Conformal Field Theory

In the last years there has been a strong interest in formulating measures of entanglement and use them to extended quantum systems with many degrees of freedom. In quantum field theory entanglement is much less understood than in quantum mechanics. One could argue that quantum field theory is just the continuous limit of quantum mechanics, but several complications may arise. For instance, the infinite dimensionality of the Hilbert spaces and the fact that for gauge theories there are ambiguities in factorizing the Hilbert space are just some of these obstacles.

Although these issues and the fact that there are several measures of entanglement, entanglement entropy and entanglement negativity are among the few entanglement related quantities which have been studied in QFT. By tracing out part of the degrees of freedom of correlated quantum systems, useful and non-trivial information can be obtained by the study of the reduced density matrix. We recall that although ρ can be a pure state, $\rho_A = \mathrm{Tr}_B\, \rho$ is a mixed state.

In the framework of quantum field theory the entanglement entropy (1.11) can be computed by means of the replica trick. This procedure can be split in two steps. First one computes the trace of the n-th power of the density matrix $\mathrm{Tr}\, \rho_A^n$ and then performs an analytic continuation of the resulting expression to any complex n. The entanglement entropy (1.11) can be obtained as

$$S_A = -\lim_{n\to 1} \partial_n \,\mathrm{Tr}\, \rho_A^n \,. \tag{1.49}$$

The Rényi entropies are defined

$$S_A^{(n)} = \frac{1}{1-n} \log \mathrm{Tr}\, \rho_A^n \,. \tag{1.50}$$

Given the normalization condition $\mathrm{Tr}\, \rho_A = 1$, the replica trick says

$$S_A = \lim_{n\to 1} S_A^{(n)} \,. \tag{1.51}$$

It is important to emphasize that $S_A^{(n)}$ contains more information than S_A. Indeed from the Rényi entropies one can in principle extract the full spectrum of ρ_A [44].

A lot of effort has been devoted in understanding the behavior of entanglement entropy in critical systems. In this thesis we will focus our attention to the case of 1+1 and $2+1$ space-time dimensions, when A and B correspond to a spatial bipartition.

In [15, 45, 46] the simplest example was studied, namely the entanglement entropy of an interval A of length ℓ in an infinite line, finding

$$S_A = \frac{c}{3} \log \frac{\ell}{a} + c_1' \,, \tag{1.52}$$

where c is the central charge of the corresponding CFT, a is some UV regulator and c_1' is a non universal constant.

Let us consider the subregion A made by two subsystems A_1 and A_2 ($A = A_1 \cup A_2$), which can be either adjacent or disjoint (see Fig. 1.3 for a two spatial dimensional representation). We stress that, when A_1 and A_2 are separated, the entanglement entropy S_A quantifies only the entanglement between A and the remainder of the system B, but not the entanglement between A_1 and A_2. To measure the correlations between A_1 and A_2, which can be either adjoint or disjoint, an interesting quantity to consider is the *mutual information*

$$I_{A_1,A_2} \equiv S_{A_1} + S_{A_2} - S_{A_1 \cup A_2} \,, \tag{1.53}$$

and, the corresponding Rényi mutual information

$$I^{(n)}_{A_1,A_2} \equiv \frac{1}{n-1} \ln \left(\frac{\operatorname{Tr} \rho_A^n}{\operatorname{Tr} \rho_{A_1}^n \operatorname{Tr} \rho_{A_2}^n} \right) . \tag{1.54}$$

Applying the replica trick for the entanglement entropy it is easy to see that

$$I_{A_1,A_2} = \lim_{n \to 1} I^{(n)}_{A_1,A_2} \,, \tag{1.55}$$

where $I^{(n)}_{A_1,A_2} = S^{(n)}_{A_1} + S^{(n)}_{A_2} - S^{(n)}_{A_1 \cup A_2}$ is the corresponding combination of Rényi entropies. However, let us underline that the mutual information is not a measure of the entanglement between A_1 and A_2, but quantify the amount of global correlations between the two subsystem [47–49]. For instance, mutual information takes into account also the classical (thermal) correlations between the two regions.

1.5.1 Replica trick for entanglement entropy

In this subsection we explain how to compute $\operatorname{Tr} \rho_A^n$ in order to perform the above mentioned replica trick.

Consider a lattice quantum theory in $1+1$ space-time dimensions and denote by a the lattice spacing and label the lattice sites by a discrete variable x. The domain of x can be finite, semi-infinite or infinite, while time is considered to be continuous. We denote a complete set of local commuting observables with $\{\hat{\phi(x)}\}$, and their eigenvalues and eigenvectors respectively by $\{\phi(x)\}$ and $\otimes_x |\{\phi(x)\}\rangle$. The dynamics

of the theory is described by the hamiltonian H. The density matrix ρ in a thermal state with inverse temperature β can be expressed by

$$\rho(\{\phi^{''}_{x_2}|\phi^{'}_{x_1}\}) = Z(\beta)^{-1}\langle\{\phi^{''}_{x_2}|e^{-\beta H}|\phi^{'}_{x_1}\}\rangle\,, \tag{1.56}$$

where $Z(\beta) = \mathrm{Tr}\, e^{-\beta H}$ is the partition function. We can express it as an euclidean path integral

$$\rho(\{\phi^{''}(x_2)|\phi^{'}(x_1)\}) = Z^{-1}\int [d\phi(y,\tau)]\prod_y \delta(\phi(y,0)-\phi^{'}(x_1))\prod_y \delta(\phi(y,\beta)-\phi^{''}(x_2))e^{-S_E} \tag{1.57}$$

where $S_E = \int_0^\beta L_E d\tau$, with L_E the euclidean lagrangian. Setting $\{\phi^{''}(x)\} = \{\phi^{'}(x)\}$ and integrating over them, we find $\mathrm{Tr}\,\rho = 1$. This operation corresponds to sew together the edges along $\tau = 0$ and $\tau = \beta$ to form a cylinder of circumference β.

Consider now the case of a subsystem A composed by the points x in the disjoint intervals $(u_1, v_1), \cdots, (u_N, v_N)$. A similar expression for the reduced density matrix ρ_A may be found by sewing together only those points x which are not in A. This operation will leave along the line $\tau = 0$ some open cuts, one for each interval (u_i, v_i). By making now n copies of the above construction, each labelled by an integer k with $1 \leq k \leq n$, and sewing them together cyclically along the cuts so that $\phi^{'}(x)_k = \phi^{''}(x)_{k+1}$ and $\phi^{'}(x)_n = \phi^{''}(x)_1$ for all the $x \in A$ (see Fig. 1.2 for one interval). If we denote the path integral on this n-sheeted structure by $Z_n(A)$, then

$$\mathrm{Tr}\,\rho_A^n = \frac{Z_n(A)}{Z^n} \tag{1.58}$$

Since $\mathrm{Tr}\,\rho_A^n = \sum_j \lambda_j^n$, where $\{\lambda_j\} \in [0,1)$ are all the eigenvalues of ρ_A, then it follows that the left hand side is absolutely convergent and thus analytic for all $Ren > 1$. The derivative with respect to n therefore also exists and it is analytic. If the entropy $\rho_A = -\sum_j \lambda_j \log\lambda_j$ is finite, the limit as $n \to 1^+$ of the first derivative converges to this value. So, we conclude that the right hand side of Eq. (1.58) has a unique analytic continuation to $\mathrm{Re}(n) > 1$ and that its first derivative at $n = 1$ gives the required entropy

$$S_A = -\lim_{n\to 1}\frac{\partial}{\partial_n}\mathrm{Tr}\,\rho_A^n = -\lim_{n\to 1}\frac{\partial}{\partial_n}\frac{Z_n(A)}{Z^n}\,. \tag{1.59}$$

For the sake of simplicity, everything here has been done in the discrete space domain, but in [15, 45] it was shown that the continuum limit can be taken safely, since most of the UV divergences of the QFT cancels in the ratio (1.58).

Now, suppose to consider a subsystem $A = \cup_{i=1}^N A_i$ made of N disjoint intervals and denote by $A_i = [u_i, v_i]$ the endpoints of the i-th interval with $i = 1, \cdots, N$. In [45, 46] Calabrese and Cardy developed a method to compute $\mathrm{Tr}\,\rho_A^n$ as the $2N$

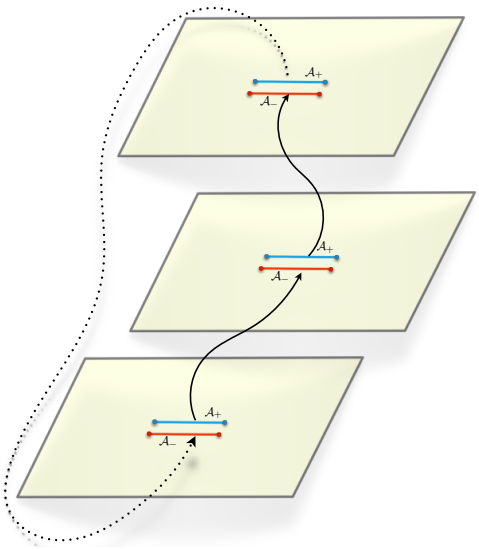

Figure 1.2: The Euclidean geometry for computing the matrix elements of powers of the reduced density matrix ρ_A. It is illustrated the situation where we glue three copies of the replicated path integrals to construct ρ_A^3 matrix elements with the identifications between boundary conditions on the replica copies indicate by the arrows. The final trace to compute the third Rényi entropy is indicated by the dotted line (This image is taken from [50]).

point function of twist fields

$$\operatorname{Tr}\rho_A^n = \langle \prod_{i=1}^{N} \mathcal{T}_n(u_i)\bar{\mathcal{T}}_n(v_i)\rangle \,. \tag{1.60}$$

In CFT the twist fields transform like primaries. These fields have been largely studied in the early days of string theory [51–57] and their crucial role for the entanglement computations has been exploited during the last decade.

In the simplest case of one interval $A = [u, v]$ in an infinite line, $\operatorname{Tr}\rho_A^n$ is given by a two point correlation function of twist field on the complex plane, which is completely fixed by global conformal invariance

$$\operatorname{Tr}\rho_A^n = \langle \mathcal{T}_n(u)\bar{\mathcal{T}}_n(v)\rangle = \frac{c_n}{|u-v|^{2\Delta_n}} \,. \tag{1.61}$$

Now, since the twist fields behave like primary operators they have the same scaling dimension

$$\Delta_n = \frac{c}{12}\left(n - \frac{1}{n}\right) \,. \tag{1.62}$$

The constant c_n is not universal and for the normalization condition we have that $c_1 = 1$. From (1.61) it is easy to recover (1.52).

In the case of four (two disjoint intervals) and higher point correlation functions, the global conformal invariance does not fix the precise dependence on u_i and v_i, because it is easy to construct invariant ratios involving these points. If we apply the conformal map such that $u_1 \to 0$, $u_N \to 1$ and $v_N \to \infty$, that is

$$w_N(z) = \frac{(u_1 - z)(u_N - v_N)}{(u_1 - u_N)(z - v_N)} \,, \tag{1.63}$$

then the other points u_i's and v_i's are sent into the $2N-3$ four-point rations $x_1 = w_N(v_1)$, $x_2 = w_N(u_2)$, $x_3 = w_N(v_2), \cdots, x_{2N-3} = w_N(v_{N-1})$, which are invariant under $SL(2,\mathbb{C})$ transformations. The ordering $0 < x_1 < x_2 < \cdots < x_{2N-3}$ is preserved by the map (1.63). Denoting by $\boldsymbol{x}$ the vector with elements the four-point ratios $x_1, \cdots, x_{2N-3}$ and by means of global conformal invariance, we can write the $2N$ point function (1.60) as [46]

$$\operatorname{Tr}\rho_A^n = c_n^N \left| \frac{\prod_{i<j}(u_j - u_i)(v_j - v_i)}{\prod_{i,j}(v_j - u_i)} \right|^{2\Delta_n} \mathcal{F}_{N,n}(\boldsymbol{x}) \,, \tag{1.64}$$

where $i, j = 1, \cdots, N$ and the function $\mathcal{F}_{N,n}(\boldsymbol{x})$ keeps track of the full operator content of the particular model and therefore it must be computed case by case. From the normalization condition $\operatorname{Tr}\rho_A = 1$ we have $\mathcal{F}_{N,1}(\boldsymbol{x}) = 1$.

The case of two interval is much more interesting and useful also when we will consider negativity. When the subsystem $A = A_1 \cup A_2$ is made by two disjoint intervals $A_1 = [u_1, v_1]$ and $A_2 = [u_2, v_2]$ (with the endpoints ordered as $u_1 < v_1 < u_2 < v_2$), a crucial role will be played by the function $\mathcal{F}_{2,n}(x)$ as we will see soon. In this setup we have $N = 2$ and there is only one four-point ration $0 < x < 1$

$$x = \frac{(u_1 - v_1)(u_2 - v_2)}{(u_1 - u_2)(v_1 - v_2)} \,. \tag{1.65}$$

Lots of efforts were put in the derivation of analytic expressions for the function $\mathcal{F}_{2,n}(x)$. In [51–58] some methods were developed to study CFT on higher genus Riemann surfaces and their results are expressed in terms of Riemann theta functions [59–61]. Their analytic continuation in n for the most general case is still an open problem and therefore we still miss an expression for the entanglement entropy S_A. Various numerical studies realized by means of different techniques [62–69] support these CFT predictions. As already said, it is important to emphasize the crucial difference between the case of one single interval and the case of multiple intervals. In the former $\mathrm{Tr}\,\rho_A^n$ and S_A are sensible only to the central charge of the CFT, as Eqs. (1.52) and (1.61) manifest. In the latter, these computations just mentioned above showed that when the subsystem A is composed by $N \geq 2$ disjoint intervals on the infinite line, the Rényi entropies encode all the data of the CFT, because $\mathrm{Tr}\,\rho_A^n$ is obtained as a four-point function of twist fields [70, 71]. Eq. (1.64) in the case $N = 2$ becomes

$$\mathrm{Tr}\rho_A^n = \langle \mathcal{T}_n(u_1)\bar{\mathcal{T}}_n(v_1)\mathcal{T}_n(u_2)\bar{\mathcal{T}}_n(v_2)\rangle \tag{1.66}$$

$$= c_n^2 \left[\frac{(u_2 - u_1)(v_2 - v_1)}{(v_1 - u_1)(v_2 - u_2)(u_2 - v_1)(v_2 - u_1)}\right]^{2\Delta_n} \mathcal{F}_{2,n}(x) \,. \tag{1.67}$$

The function $\mathcal{F}_{2,n}(x)$ has been studied for some explicit models [62–64, 67–76]. Other works were done using the holographic approach [74, 77–86] and in the framework of higher dimensional conformal field theories [87–93].

In the CFT describing the free boson compactified on a circle of radius r the function $\mathcal{F}_{2,n}(x)$ is exactly known. By introducing $\eta = r^2/2$, it can be written in terms of Riemann theta functions as follows

$$\mathcal{F}_{2,n}(x) = \frac{\Theta(\mathbf{0}|\eta\tau_2)\Theta(\mathbf{0}|\tau_2/\eta)}{[\Theta(\mathbf{0}|\tau_2)]^2} \,, \tag{1.68}$$

where $\tau_2 = \tau_2(x)$ is an $(n-1) \times (n-1)$ matrix, called the period matrix, with elements [70]

$$(\tau_2)_{i,j} = \mathrm{i}\,\frac{2}{n}\sum_{k=1}^{n-1} \sin(\pi k/n)\,\frac{F_{k/n}(1-x)}{F_{k/n}(x)}\,\cos[2\pi(k/n)(i-j)] \,, \tag{1.69}$$

where $F_s(x) \equiv {}_2F_1(s, 1-s; 1; x)$, being ${}_2F_1$ the hypergeometric function. Notice that $\mathcal{F}_{2,n}(0) = 1$. Since the ratio $x \in (0,1)$, the period matrix $\tau(x)$ is purely imaginary. The Riemann theta function is defined [59–61] as

$$\Theta(\boldsymbol{z}|M) \equiv \sum_{\boldsymbol{m}\in\mathbb{Z}^{n-1}} e^{\,\mathrm{i}\pi\,\boldsymbol{m}^{\mathrm{t}}\cdot M\cdot\boldsymbol{m}+2\pi\mathrm{i}\,\boldsymbol{m}^{\mathrm{t}}\cdot\boldsymbol{z}}\,. \tag{1.70}$$

where M is a $(n-1)\times(n-1)$ symmetric complex matrix with positive imaginary part and $\boldsymbol{z} \in \mathbb{C}^{n-1}/(\mathbb{Z}^{n-1} + \Omega\mathbb{Z}^{n-1})$ is a complex $(n-1)$ dimensional vector. It is worth observing that the analytic continuation of Θ is a hard task to be accomplished.

An interesting case is when the compactification radius is set to be $\eta = 1/2$. The free boson theory corresponds to the scaling limit of the XX spin chain, which is the so called Dirac point. Using theta functions identities it is possible to express Eq. (1.68) as

$$\mathcal{F}^{\mathrm{Dirac}}_{2,n}(x) = \frac{1}{2^{n-1}\,|\Theta(\boldsymbol{0}|\tau_2)|^2}\sum_{\boldsymbol{\varepsilon},\boldsymbol{\delta}}\left|\Theta\begin{bmatrix}\boldsymbol{\varepsilon}\\ \boldsymbol{\delta}\end{bmatrix}(\boldsymbol{0}|\tau_2)\right|^2, \tag{1.71}$$

where the period matrix τ_2 is the same as in (1.69), while Θ is the Riemann theta function with characteristic defined as [59–61]

$$\Theta[\boldsymbol{e}](\boldsymbol{z}|M) \equiv \sum_{\boldsymbol{m}\in\mathbb{Z}^{n-1}} e^{\,\mathrm{i}\pi(\boldsymbol{m}+\boldsymbol{\varepsilon})^{\mathrm{t}}\cdot M\cdot(\boldsymbol{m}+\boldsymbol{\varepsilon})+2\pi\mathrm{i}\,(\boldsymbol{m}+\boldsymbol{\varepsilon})^{\mathrm{t}}\cdot(\boldsymbol{z}+\boldsymbol{\delta})}, \qquad \boldsymbol{e} \equiv \begin{pmatrix}\boldsymbol{\varepsilon}\\ \boldsymbol{\delta}\end{pmatrix}, \tag{1.72}$$

where the vector $\boldsymbol{e}^{\mathrm{t}} \equiv (\boldsymbol{\varepsilon}^{\mathrm{t}}, \boldsymbol{\delta}^{\mathrm{t}})$ is the characteristic of the Riemann theta function (1.72), being $\boldsymbol{\varepsilon}$ and $\boldsymbol{\delta}$ two $(n-1)$ dimensional vectors whose elements are either 0 or $1/2$. The characteristic provides the parity of (1.72) as a function of $\boldsymbol{z}$, which is the same one of the integer number $4\boldsymbol{\varepsilon}\cdot\boldsymbol{\delta}$

$$\Theta[\boldsymbol{e}](-\boldsymbol{z}|\Omega) = (-1)^{4\boldsymbol{\varepsilon}\cdot\boldsymbol{\delta}}\,\Theta[\boldsymbol{e}](\boldsymbol{z}|\Omega)\,. \tag{1.73}$$

It is easy to realize that there are $2^{2(n-1)}$ characteristics: $2^{n-2}(2^{n-1}+1)$ are even and $2^{n-2}(2^{n-1}-1)$ are odd. In this thesis only the trivial vector $\boldsymbol{z} = \boldsymbol{0}$ occurs and therefore all the Riemann theta functions occurring in this work with odd characteristic vanish identically. We find convenient to define from now on $\Theta[\boldsymbol{e}](M) \equiv \Theta[\boldsymbol{e}](\boldsymbol{0}|M)$ and $\Theta(M) \equiv \Theta(\boldsymbol{0}|M)$ when the characteristic is vanishing. The Riemann theta functions throughout this thesis have been evaluated by using the builtt-in function *SiegelTheta*. Another model for which the scaling function $\mathcal{F}_{2,n}(x)$ is known is the critical Ising model

$$\mathcal{F}^{\mathrm{Ising}}_{2,n}(x) = \frac{1}{2^{n-1}\,|\Theta(\boldsymbol{0}|\tau_2)|}\sum_{\boldsymbol{\varepsilon},\boldsymbol{\delta}}\left|\Theta\begin{bmatrix}\boldsymbol{\varepsilon}\\ \boldsymbol{\delta}\end{bmatrix}(\boldsymbol{0}|\tau_2)\right|, \tag{1.74}$$

where all its element were explained already few lines above.

The generalization to N intervals has been discussed in [94]. In this case the genus of the Riemann surface becomes $g = (N-1)(n-1)$.

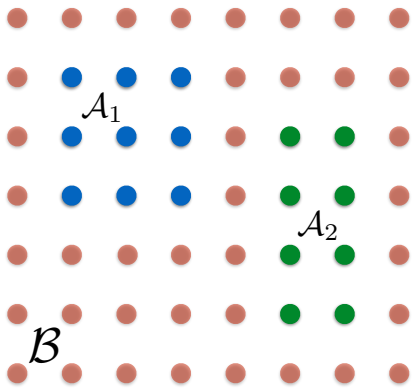

Figure 1.3: A discrete latticed quantum system with a Hilbert space at every site. We divided the lattice in three regions, A_1, A_2 and B, and consequently the total Hilbert space can be factorized as $\mathcal{H} = \mathcal{H}_{A_1} \otimes \mathcal{H}_{A_2} \otimes \mathcal{H}_B$.

1.6 Logarithmic Negativity in Conformal Field Theory

In this section we define negativity in the context of quantum field theory and then extend the replica approach to the computation of the logarithmic negativity.

We are now interested into the entanglement between two non-complementary parts A_1 and A_2. Indeed, the union $A = A_1 \cup A_2$ is in a mixed state with density matrix $\rho_A = \mathrm{Tr}_B\, \rho$, with B the complement of A. We have already discussed in §1.5 that the mutual information (1.53) is not a measure of entanglement between A_1 and A_2, but it takes into account also classical correlations between the two regions.

We are here interested only at quantum correlations, i.e the entanglement between A_1 and A_2. In 1.3 we discussed how the negativity provides a proper measure of entanglement in a bipartite mixed state [12, 16, 29–31, 36]. Let us recall its definition. The logarithmic negativity is defined through the partial transpose of ρ with respect to one of the two parts. Let us consider the partial transpose with respect to the A_2's degrees of freedom. Now, denoting by $|e_i^{(1)}\rangle$ and $|e_j^{(2)}\rangle$ two arbitrary bases in the Hilbert spaces corresponding to A_1 and A_2. The partial transpose of ρ_A with respect to A_2 degrees of freedom is defined as

$$\langle e_i^{(1)} e_j^{(2)} | \rho_A^{T_2} | e_k^{(1)} e_l^{(2)} \rangle = \langle e_i^{(1)} e_l^{(2)} | \rho_A | e_k^{(1)} e_j^{(2)} \rangle \,. \tag{1.75}$$

Since the spectrum of the Hermitian matrix $\rho_A^{T_2}$ can contain also negative eigenvalues, it is worth computing its trace norm $||\rho_A^{T_2}||_1 = \mathrm{Tr}\,|\rho_A^{T_2}| = \sum_i |\lambda_i|$, which is the sum of the absolute values of the eigenvalues of $\rho_A^{T_2}$. The *logarithmic* negativity is then defined as

$$\mathcal{E} \equiv \ln ||\rho_A^{T_2}||_1 = \ln \mathrm{Tr}\,|\rho_A^{T_2}| \,, \tag{1.76}$$

Notice that the negativity is symmetric under exchange of A_1 and A_2, as any good measure of the relative entanglement should be. For future convenience we also introduce

$$\mathcal{E}_n = \log(R_n)\,, \quad R_n \equiv \frac{\mathrm{Tr}(\rho_A^{T_2})^n}{\mathrm{Tr}\ \rho_A^n}\,. \tag{1.77}$$

It is not difficult to show that $R_2 = 1$ and therefore $\mathcal{E}_2 = 0$.

1.6.1 Replica trick for the logarithmic negativity

The QFT approach to the logarithmic negativity $\mathcal{E}$ is based on a replica trick [95, 96]. Let us consider the traces $\mathrm{Tr}(\rho_A^{T_2})^n$ of integer powers of $\rho_A^{T_2}$. For n even and odd, denoted by n_e and n_o respectively, we have

$$\mathrm{Tr}(\rho_A^{T_2})^{n_e} = \sum_i \lambda_i^{n_e} = \sum_{\lambda_i>0} |\lambda_i|^{n_e} + \sum_{\lambda_i<0} |\lambda_i|^{n_e}\,, \tag{1.78a}$$

$$\mathrm{Tr}(\rho_A^{T_2})^{n_o} = \sum_i \lambda_i^{n_o} = \sum_{\lambda_i>0} |\lambda_i|^{n_o} - \sum_{\lambda_i<0} |\lambda_i|^{n_o}\,, \tag{1.78b}$$

where λ_i are the eigenvalues of $\rho_A^{T_2}$. The functional dependence of $\mathrm{Tr}(\rho_A^{T_2})^n$ on $|\lambda_i|$ is a result of the parity of n. Setting $n_e = 1$ in (1.78a), we formally obtain $\mathrm{Tr}\,|\rho_A^{T_2}|$, whose logarithm gives the logarithmic negativity

$$\mathcal{E} = \lim_{n_e\to 1} \log \mathrm{Tr}\left(\rho_A^{T_2}\right)^{n_e}. \tag{1.79}$$

Instead, if we set $n_o = 1$ in (1.78b), we just get the normalization $\mathrm{Tr}\,\rho_A^{T_2} = 1$. Thus, the relevant fact is that the analytic continuations from even and odd values of n are different.

In the special case of a pure state $\rho = |\Psi\rangle\langle\Psi|$ acting on a bipartite Hilbert space, $\mathcal{H} = \mathcal{H}_{A_1} \otimes \mathcal{H}_{A_2}$, the moments of the partial transpose are related to the Rényi entropies as follows [95, 96]

$$\mathrm{Tr}\left(|\Psi\rangle\langle\Psi|^{T_2}\right)^n = \begin{cases} \mathrm{Tr}\,\rho_{A_2}^{n_o} & \text{odd } n = n_o\,, \\ \left(\mathrm{Tr}\,\rho_{A_2}^{n_e/2}\right)^2 & \text{even } n = n_e\,, \end{cases} \tag{1.80}$$

where $\rho_{A_2} = \mathrm{Tr}_{A_1}|\Psi\rangle\langle\Psi|$ is the reduced density matrix of the subsystem A_2. From the relation (1.80) and the replica limit (1.79), one easily gets that $\mathcal{E} = S_{A_2}^{(1/2)}$.

The logarithmic negativity and the moments $\mathrm{Tr}(\rho_A^{T_2})^n$ of the partial transpose are interesting quantities to compute for bipartite mixed states. In this thesis we will focus on a particular system in its ground state, considering the mixed state given by the reduced density matrix $\rho_A = \mathrm{Tr}_{\mathcal{H}_B}|\Psi\rangle\langle\Psi|$ of a spatial subsystem, whose corresponding Hilbert space $\mathcal{H}_A = \mathcal{H}_{A_1} \otimes \mathcal{H}_{A_2}$ is bipartite. Instead of the moments

of $\rho_A^{T_2}$, we find more convenient to consider the quantity $\mathcal{E}_n$ defined in (1.77). Given the normalization condition of ρ_A, the replica limit (1.79) simply tells that

$$\mathcal{E} = \lim_{n_e \to 1} \mathcal{E}_{n_e} \,. \tag{1.81}$$

For $1+1$ dimensional CFTs in the ground state, the logarithmic negativity and the moments of the partial transpose have been studied for both adjacent and disjoint intervals [95–101]. This analysis has been extended also to a bipartite system at finite temperature [102]. The moments of the partial transpose for some fermionic systems on the lattice have been studied through a method involving correlators in [103, 104] and the overlap matrix in [105]. The logarithmic negativity has been considered also for a non vanishing mass [96, 106] and out of equilibrium [107–110]. For two disjoint intervals at zero temperature $\mathrm{Tr}(\rho^{T_2}_{A_1\cup A_2})^n$ must be computed case by case because it encodes all the CFT data. The replica limit (2.6) for these expressions turns out to be difficult to compute, like for the mutual information. Indeed, analytic results have not been found for all the possible configurations of intervals. Numerical results for the logarithmic negativity have been found also for systems with impurities by employing DMRG techniques [111–114]. Other interesting numerical studies for various one dimensional lattice systems have been performed in [112, 115–122]. The same numerical method employed to get the mutual information from the replica limit has been used to get the logarithmic negativity from the replica limit (1.79), since similar difficulties occur [123].

In two spatial dimensions, the logarithmic negativity of topological systems has been considered [124–129] and recently interesting lattice analysis have been performed for both fermionic and bosonic systems [130, 131]. Some results have been found also in the context of holography [132, 133].

Finally, let us notice that the replica approach introduced in the context of CFT [95, 96], has been later applied to many other circumstances [97, 98, 122, 124–126, 132, 133].

1.7 Area Law, its violations and sub-leading corner terms

Originally, entanglement entropy gained a lot of attention after some works related to black hole physics by Bombelli *et al.* [134], Srednicki [135], Callan and Wilczek [136], Holzhey *et al.* [15], where it was realized that the geometric entropy (this was the original name, since the bipartition of $\mathcal{H}$ is spatial) of a free scalar bosonic field in its ground state obeys the so-called *area law*, *i.e* in d-space dimension it scales with the surface of the subsystem A, as follows

$$S_A \propto \left(\frac{\ell_A}{\epsilon}\right)^{d-1} + \cdots \,, \tag{1.82}$$

where ℓ_A is some size of the region A and ϵ some UV cutoff. We should remind that entanglement entropy and logarithmic negativity in QFT are UV divergent and thus they need to be regulated. This follows from the fact that any state in a local QFT has short-range correlations in the ultra-violet. The ellipses in (1.82) denote less divergent terms. This area law (1.82) is opposite to the *bulk or volume law*, $S_A \propto (\ell_A/\epsilon)^d$ obeyed by generic states in the many-body Hilbert space. For the ground state, the area law is the general behavior, but there are important exceptions and Eq. (1.82) needs to be discussed more deeply as we will do in this section. This leading area law term is non universal and therefore a lot of interest is also devoted to sub-leading terms and in particular to the logarithmic ones. In general one can argue that for states in the Hilbert space of a relativistic QFT, the UV behaviour of the entanglement entropy of a smooth region A takes the form:

$$S_A = a_{d-1}\left(\frac{\ell_A}{\epsilon}\right)^{d-1} + a_{d-3}\left(\frac{\ell_A}{\epsilon}\right)^{d-3} + \cdots + \begin{cases} a_d + O(\epsilon) & d \text{ even} \\ a_d \log(\ell_A/\epsilon) + O(1) & d \text{ odd} \end{cases} \tag{1.83}$$

The general rule is that the expansion of entanglement entropy in terms of the size of the systems may have terms which are universal and terms which instead depend on the UV cutoff, as the area law one. The former play a more fundamental game, but also the latter can be very interesting to better understand the nature of entanglement. Like the central charge in $1+1$, universal terms can potentially give insight into the low energy theories governing critical behavior, providing for example an effective measure of degrees of freedom in the CFT or bounds on renormalization group flow, depending on the geometry of A. It is worthwhile to notice for our future discussion that in Eq.(1.83) a logarithmic term appears for d odd, while it never appears for d even. For any d a logarithmic terms appears in the expansion of the entanglement entropy (and also logarithmic negativity), when the region A has a non-smooth boundary, i.e. at least one corner.

For one dimensional quantum systems, we have to make a distinction between critical and non-critical ground states. The area law in $1+1$-dimensions yields a constant entropy, independently of the system size. This only occurs for non-critical ground states characterized by a finite correlation length [137], such as the non-critical dimerized quantum spin-1/2 XY chain, which after a Jordan-Wigner transformation is equivalent to a free-fermion system.

On the other hand, critical (*i.e* gapless) chains described by a conformal field theory display a logarithmic violation of the strict area law. Rényi entropies grow with the subsystem length ℓ_A following the universal form

$$S_A^{(n)} = \frac{c}{6}\left(1+\frac{1}{n}\right)\log\left(\frac{L}{\pi}\sin\left[\frac{\pi\ell_A}{L}\right]\right) + s_n + \cdots \tag{1.84}$$

for periodic chains of length L. The constant term s_n is non-universal but in some

cases can be evaluated exactly [138], while the ellipses in the above equation represent subleasing correction to scaling and in general the vanish as power-laws of the subsystem size [139, 140]. Eq. (1.84) refers to finite size quantum systems of length L, but an equivalent behavior happens for the same system in the continuum limit

$$S_A^{(n)} = \frac{c}{6}\left(1+\frac{1}{n}\right)\log\frac{\ell_A}{\epsilon} + s_n + \cdots , \tag{1.85}$$

where ϵ is the UV cutoff and c is an universal term, more precisely the central charge that in a rough sense counts the number of low energy degrees of freedom. For instance, in the case of a CFT described by N free bosonic fields, c is equal to N [141].

Another important violation of the area law is given by free fermions in space dimensions $d > 1$, when there is a well defined Fermi surface [142–144]

$$S_A \propto (\ell_A/\epsilon)^{d-1}\log(\ell_A/\epsilon) \tag{1.86}$$

For non-critical fermions the entropy instead obeys a strict area law.

Intuitively, the area law expressed by Eq. (1.82) is understood as resulting from entanglement that involves degrees of freedom located near the boundary between regions A and B. In a similar way, the logarithmic correction of Eqs. (1.84), (1.85) and (1.86) has its origin in contributions to entanglement from degrees of freedom that are further away from the boundary between A and B.

More relevant for this thesis is the following case. For a relativistic free bosonic field theory, which is equivalent to a system of coupled harmonic oscillators, entanglement entropy and Rényi entropies scale with an area law in space dimension $d > 1$ [15, 134–136]. This was numerically confirmed for critical and non-critical systems where a strict area law is observed in both cases [145]

Now we focus our attention on subleasing terms appearing in higher dimensions ($d+1$, with $d > 1$) that go beyond the area law. A very interesting case, which will be discuss in Chap. 3, concerns subsystems having a non-smooth boundary with the particular example of sharp corners in $2+1$-dimensions which are responsible for additive logarithmic corrections to the area law [146–159], both for entanglement and logarithmic negativity. Now, suppose that the region A has a number i of sharp corners θ_i, then the area law for the Rényis entropies is corrected as follows

$$\Delta S_A^{(n)} = \left(\sum_i \tilde{b}_n(\theta_i)\right)\log P_A \tag{1.87}$$

where the sum is taken over all corner angles and P_A is the $1d$ shared boundary between A and B. For free scalar field theory, Casini and Huerta have provided an analytical solution [147] for integer $n > 2$, which involves a tricky numerical

solution of a set of non-linear differential equations valid for $\theta \in [0, \pi]$. The fact that the corner logarithmic terms universality emerges is really remarkable. It was then proposed that the prefactor of the logarithmic correction is an effective measure of the degrees of freedom of the underlying CFT [79, 147, 151]. Moreover, using CFT and some holographic approach, in [154, 157, 158] it was suggested that the ratio $\tilde{b}_n(\theta)/C_T$ is universal for a broad range of CFT, where C_T is the central charge of the stress tensor correlator.

1.8 Holographic Entanglement Entropy

The Bekenstein-Hawking formula for the entropy of a black hole is one of the most relevant results in theoretical physics. Their formula is

$$S_{BH} = k_B c^3 \frac{\mathcal{A}}{4G_N \hbar}\,, \tag{1.88}$$

where $\mathcal{A}$ is the area of the event horizon and it represents the first hint that suggested the idea that gravity might be *holographic*, namely all information about a region of space-time (in this case the black hole interior) is somehow encoded on its boundary. The astonishing fact about this equation is that it contains the fundamental constants $\hbar, k_B, c, G_N$, surprisingly connecting quantum mechanics, gravity and statistical mechanics.

A concrete realization of the *holographic principle* is the AdS/CFT correspondence, or gauge/gravity duality, proposed by Maldacena in [160]. This correspondence asserts that a gravity theory in the bulk of a $d+1$ space-time is dual to a conformal field theory (without gravity) which lives on the boundary of that space-time (i.e in one less dimension). This is a beautiful example of strong/weak coupling duality. In particular the strong coupling regime of the CFT is captured by the weak coupling regime of the gravity theory in the bulk. In the regime where the bulk dual is just classical gravity, one can ask if the correspondence is able to tell us anything about information theoretic quantities in the boundary field theory.

In 2006, Ryu and Takayanagi proposed that when an holographic dual of a CFT is available, the entanglement entropy of a boundary subregion is given by a nice geometric quantity in the bulk [77]. For the static situation, consider a time-slice of the asymptotically AdS geometry. Now, pick on the boundary a subregion A, with area ∂A, for which we want to compute entanglement entropy. The holographic prescription tells us to look for the bulk surface A_{min}, homologous to A and with boundary ∂A, that has minimal area. The entanglement entropy is then given by

$$S_A = \frac{\mathcal{A}(A_{min})}{4G_N}\,, \tag{1.89}$$

where G_N is the Newton constant in the bulk. This formula is an important tool to compute entanglement entropy in many situations where it would be inaccessible with other techniques. Moreover, the similarity with the Bekenstein-Hawking formula (in natural units $c = k_B = \hbar = 1$) is evident and this could be another hint that there is some striking connection between gravity and information theory.

The prescription introduced above satisfies all the properties of entanglement entropy. In particular, Eq. (1.89) satisfies the inequalities (1.12), (1.13), as shown in [161], and also (1.14) is guaranteed to be fulfilled by the homology constraint. Remarkably, for the static solution, the Ryu-Takayanagi prescription has now been proven in [162].

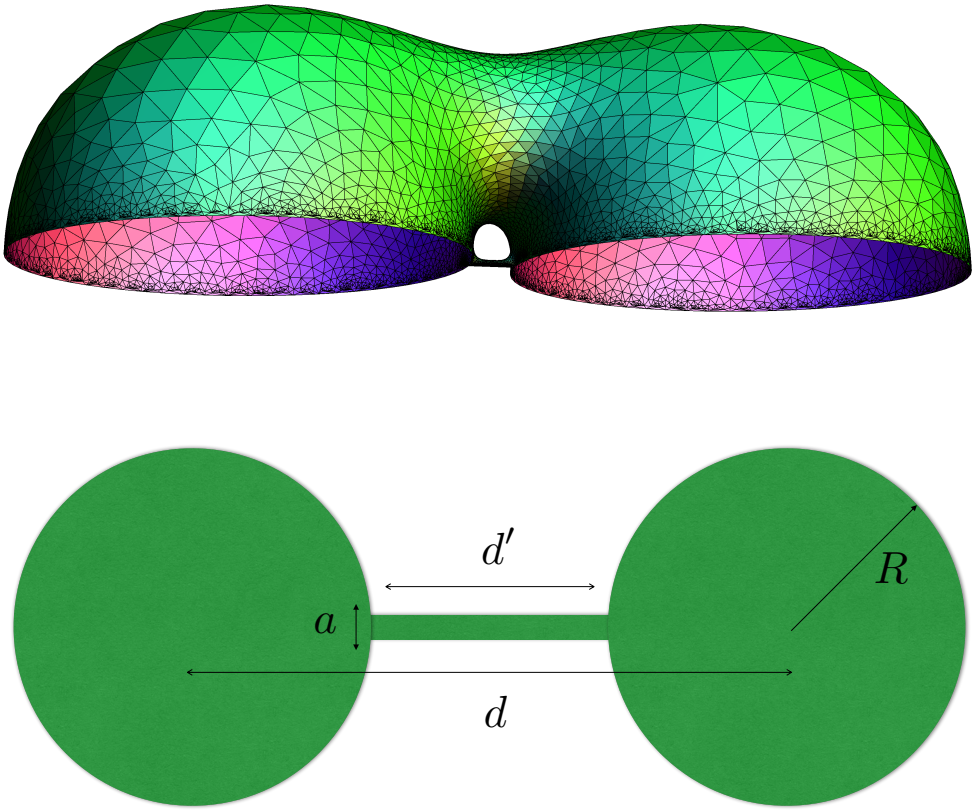

Figure 1.4: A Ryu-Takayanagi minimal surface in AdS_4 anchored to the region A showed in the lower part. The surface was made by using Surface Evolver.

During my PhD I have been involved also in a project to study the shape dependence of the Ryu-Takayanagi formula. The simplest case where such dependence is

non-trivial is AdS_4.

In Fig. 1.4 (upper panel) it is shown a Ryu-Takayanagi minimal surface in AdS_4 corresponding to the region A at the boundary of AdS_4 is depicted in the bottom panel. The fancy fact about this domain is that, for a particular range of the parameters a and the ratio d/R, the minimal surface develops an hole. This image was created using the program *Surface Evolver* [163], a widely used open source software for the modelling of liquid surfaces shaped by various forces and constraints. This program allows to numerically tackle the minimization procedure for entangling regions A having a generic shape and for which an analytic approach is very hard [86, 196].

1.9 Organization of the Thesis

The structure of this thesis follows the various arguments I have been dealing with during the years of my PhD research.

- In Chap. 2 we employ a numerical method based on rational interpolations to extrapolate the entanglement entropy of two disjoint intervals for the conformal field theories given by the free compact boson and the Ising model. We then investigate, using the same numerical approach, the case of three disjoint intervals for the Ising model and the non compact free massless boson. For the latter model, the logarithmic negativity of two disjoint intervals will be also considered. Some of our findings have been checked against existing numerical results obtained from the corresponding lattice models. This chapter is mainly based on the following work:

  [123] C. De Nobili, A. Coser, and E. Tonni, *"Entanglement entropy and negativity of disjoint intervals in CFT: Some numerical extrapolations"*, J. Stat. Mech. P06021 (2015).

- In Chap. 3 we study the logarithmic negativity and the moments of the partial transpose in the ground state of a two dimensional massless harmonic square lattice with nearest neighbour interactions for various configurations of adjacent domains. We will see that at leading order for large domains, the logarithmic negativity and the logarithm of the ratio between the generic moment of the partial transpose and the moment of the reduced density matrix at the same order satisfy an area law in terms of the length of the curve shared by the adjacent regions. We discuss also the case when the curve shared by the adjacent domains contains vertices. In this case a subleading logarithmic term occurs in these quantities and the numerical values of the corner function for some pairs of angles are obtained. In the special case of vertices corresponding to explementary angles, we will provide numerical evidence that the corner function of

the logarithmic negativity is given by the corner function of the Rényi entropy of order 1/2. This chapter is mainly based on the following work:

[164] C. De Nobili, A. Coser, and E. Tonni, *"Entanglement negativity in a two dimensional harmonic lattice: area law and corner contributions"*, J. Stat. Mech. P083102 (2016).

- In Chap. 4 we discuss some preliminary results about the spatial distribution of entanglement entropy od disjoint intervals and negativity. In particular we study the contour, which is a function providing a decomposition into single site contributions of an entanglement measure. We extend some results about the entanglement entropy contour already present in the literature to the case of disjoint intervals for the harmonic chain in $1+1$-dimensions. Moreover, we try to extend this notion to the logarithmic negativity and discuss some problems that arise in this context.

Chapter 2

Entanglement Entropy and negativity of disjoint intervals in CFT: some numerical extrapolations

This chapter is a reproduction of the paper *Entanglement Entropy and negativity of disjoint intervals in CFT: some numerical extrapolations* [123], written in collaboration with Andrea Coser and Erik Tonni.

It is well established that entanglement entropy and logarithmic negativity can be computed in quantum field theory through a method based on the replica limit. However, performing these analytic continuations in some cases is beyond our current knowledge, even for very simple models. In this chapter we employ a numerical method based on rational interpolations to extrapolate the entanglement entropy of two disjoint intervals for the conformal field theories given by the free compact boson and the Ising model. We also investigate, using the same numerical approach, the case of three disjoint intervals for the Ising model and the non compact free massless boson. For the latter model, the logarithmic negativity of two disjoint intervals will be also considered. Some of our findings have been checked against existing numerical results obtained from the corresponding lattice models.

2.1 Introduction

As already emphasized in the Introduction, entanglement measures have been the focus of an intense research activity in condensed matter theory, quantum information, quantum field theory and quantum gravity during the last decade. The most celebrated one among them is the entanglement entropy, which measures the entanglement between two complementary parts when the whole system is in a pure state.

It is probably useful to recall for completeness that the entanglement entropy S_A is the Von Neumann entropy associated to ρ_A, after tracing out the degrees of freedom of the region B as explained in §1.5 of the Introduction. We also remind that in quantum field theory, the entanglement entropy is usually computed by employing the replica limit, namely

$$S_A \equiv -\operatorname{Tr}(\rho_A \log \rho_A) = \lim_{n\to 1} S_A^{(n)}\,, \tag{2.1}$$

where $S_A^{(n)}$ are the Rényi entropies, which are defined as follows

$$S_A^{(n)} \equiv \frac{1}{1-n} \log \operatorname{Tr}(\rho_A^n)\,. \tag{2.2}$$

From this expression and the normalization condition for ρ_A, we find that $S_A = -\partial_n \operatorname{Tr}(\rho_A^n)|_{n=1}$. In §1.5 we saw that $S_A^{(n)}$ is typically known for positive integers n and therefore it must be analytically continued to real values of n in order to perform the replica limit (2.1). In quantum field theory, the entanglement entropy is a divergent quantity when $a \to 0$, being a the UV cutoff.

An important configuration we are going to study in this chapter is when the subsystem $A = A_1 \cup A_2$ is made by two disjoint spatial regions A_1 and A_2 (see Fig. 2.1, top panel, for one spatial dimension). In this case, it is convenient to deal with the mutual information (1.53) we introduced in §1.5, which we recall to be

$$I_{A_1,A_2} \equiv S_{A_1} + S_{A_2} - S_{A_1\cup A_2} = \lim_{n\to 1} I^{(n)}_{A_1,A_2}\,, \tag{2.3}$$

where in the last step we have emphasized that I_{A_1,A_2} can be found as the replica limit of the following combination of Rényi entropies

$$I^{(n)}_{A_1,A_2} \equiv S^{(n)}_{A_1} + S^{(n)}_{A_2} - S^{(n)}_{A_1\cup A_2} = \frac{1}{n-1}\,\log R_{2,n}\,, \qquad R_{2,n} \equiv \frac{\operatorname{Tr}\rho^n_{A_1\cup A_2}}{\operatorname{Tr}\rho^n_{A_1}\operatorname{Tr}\rho^n_{A_2}}\,. \tag{2.4}$$

The subadditivity of the entanglement entropy guarantees that $I_{A_1,A_2} \geqslant 0$ and the leading divergence of the different terms cancels in the combination (2.3) when the area law holds. Moreover, the mutual information (2.3) could contain more physical information with respect to the entanglement entropy of a single region. For instance, in two dimensional CFTs, while S_A of a single interval depends only on the central charge, the mutual information I_{A_1,A_2} encodes all the CFT data of the model (conformal dimensions of the primaries and OPE coefficients) [62–64, 66–71, 73, 165]. The mutual information has been studied also through the holographic approach [74, 77, 78].

Taking the limit $n \to 1$ in (2.1) and (2.3) in many interesting cases is highly non trivial. For instance, the analytic continuation of the Rényi entropies of a single

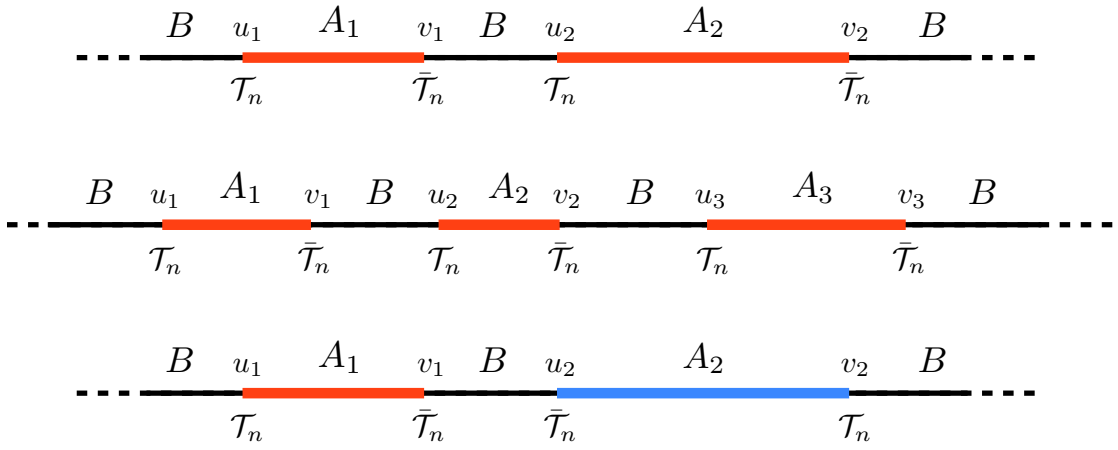

Figure 2.1: The configurations of intervals considered. Top and middle: the entanglement between a subsystem A made by either two (top) or three (middle) disjoint intervals and the remainder B. Bottom: the entanglement between two disjoint intervals A_1 and A_2 embedded in a larger system in its ground state made by $A_1 \cup A_2$ and the reminder B. In CFT correlation functions of branch-point twist fields $\mathcal{T}_n$ and $\bar{\mathcal{T}}_n$ placed at the endpoints of the intervals must be computed to get either the entanglement entropy (top and middle panels) or logarithmic negativity (bottom panel) through the proper replica limit.

interval for the excited states given by the primaries [166–168] has been studied in [169]. For the excited states given by the descendants, a closed expression for all the Rényi entropies is still not known [170]. Interesting features have been observed by considering the Rényi entropies of a single interval in critical one dimensional models for real n but no singularities have been found [65].

In this chapter we address the case of disjoint intervals for some models in one spatial dimension. The Rényi entropies for a subsystem A made by N disjoint intervals (see Fig. 2.1, middle panel for $N = 3$) are given by the partition function of the model on a Riemann surface of genus $g = (N-1)(n-1)$. These partition functions can be computed for some simple CFTs like the massless compact boson and the Ising model [70, 71, 94] but finding the corresponding analytic continuations in the most generic case is still beyond our knowledge. For two spatial dimensions, already the simple case of the entanglement entropy of a disk could lead to a difficult replica limit [171].

The other interesting quantity that we are going to consider in this chapter is the logarithmic negativity, which is a measure of entanglement for bipartite mixed states [12, 16, 29–31, 34, 36, 115, 172], as we already said in the Introduction. We remind

that the logarithmic negativity is given by

$$\mathcal{E} \equiv \log \mathrm{Tr}\, |\rho^{T_2}_{A_1 \cup A_2}| \,, \tag{2.5}$$

where $\mathrm{Tr}\, |\rho^{T_2}_{A_1 \cup A_2}|$ is the trace norm of the partial transpose (hermitian) matrix $\rho^{T_2}_{A_1 \cup A_2}$, which was defined in (1.5) and also in (1.75). The trace norm is the sum of the absolute values of its eigenvalues. Taking into account the traces $\mathrm{Tr}(\rho^{T_2}_{A_1 \cup A_2})^n$ of integer powers of $\rho^{T_2}_{A_1 \cup A_2}$, it is not difficult to observe the parity effect described in (1.78a) and (1.78b). In particular, considering the sequence of the odd powers $n = n_o$ and the one of the even powers $n = n_e$, the logarithmic negativity (2.5) can be found through the following replica limit [95, 96]

$$\mathcal{E} = \lim_{n_e \to 1} \log \mathrm{Tr} \left(\rho^{T_2}_{A_1 \cup A_2}\right)^{n_e} . \tag{2.6}$$

Notice that for $n_o \to 1$ one simply recovers the normalization condition $\mathrm{Tr}\, \rho^{T_2}_{A_1 \cup A_2} = 1$. For a bipartite pure state a relation occurs between $\mathrm{Tr}(\rho^{T_2}_{A_1 \cup A_2})^n$ and the Renyi entropies which tells us that the logarithmic negativity reduces to the Rényi entropy of order $n = 1/2$. However, we are interested in the logarithmic negativity of mixed states and the reduced density matrix is an important example. Thus, given a quantum system in a pure state and considering the reduced density matrix $\rho_{A_1 \cup A_2}$ of two adjacent or disjoint spatial regions, while $S_{A_1 \cup A_2}$ measures the entanglement between $A_1 \cup A_2$ and the complementary region B, the logarithmic negativity in (2.5) measures the entanglement between A_1 and A_2 (see Fig. 2.1, bottom panel, for one spatial dimension).

In this chapter we numerically extrapolate the entanglement entropy and the logarithmic negativity through their replica limits, which are respectively (2.1) and (2.6), for simple two dimensional CFT models and for configurations of intervals whose analytic continuations for S_A and $\mathcal{E}$ are not known. In particular, for the free massless boson, both compactified and in the decompactification regime, and for the Ising model, $\mathrm{Tr}\, \rho^n_A$ are known analytically for a generic number N of disjoint intervals [70, 71, 94], while $\mathrm{Tr}(\rho^{T_2}_{A_1 \cup A_2})^n$ is known analytically for two disjoint intervals [95–98]. We consider some of these models for two or three disjoint intervals (only some configurations in the latter case) and employ a numerical method based on rational interpolations to get the corresponding entanglement entropy or logarithmic negativity. This extrapolating method has been first suggested in this context by [171] (see [173] for other numerical methods). We checked our extrapolations against numerical results found through the corresponding lattice models whenever they are available in the literature, finding very good agreement; otherwise the method provides numerical predictions that could be useful benchmarks for future studies.

The chapter is organized as follows. In §2.2 we extrapolate the mutual information for the compact boson and for the Ising model comparing the results with the

corresponding ones found for the XXZ spin chain [63] and the critical Ising chain [64]. In §2.3 the entanglement entropy of three disjoint intervals is considered for the non compact boson and for the Ising model. While the extrapolations for the former model can be checked against exact results for the periodic harmonic chain, there are no results in the literature about the entanglement entropy of three disjoint intervals for the critical Ising chain to compare with. In §2.4 we focus on the logarithmic negativity of two disjoint intervals for the non compact boson. The appendix §2.A contains a discussion about the rational interpolation method that has been employed throughout the chapter.

2.2 Mutual information

In this section, after a quick review of the computation of $I^{(n)}_{A_1,A_2}$ in CFT, we focus on the compactified boson and on the Ising model because $I^{(n)}_{A_1,A_2}$ is known analytically in these cases. The numerical extrapolation of the analytic expressions for $I^{(n)}_{A_1,A_2}$ to $n \to 1$ leads to the mutual information, which can be compared with the corresponding numerical results found from the XXZ spin chain and the Ising chain in a transverse field.

Let us consider a two dimensional CFT with central charge c at zero temperature. As first studied in the seminal paper [45] and previously discussed in §1.5, $\operatorname{Tr}\rho_A^n$ for a subsystem A made by N disjoint intervals can be computed as the $2N$-point correlation function of *branch-point twist fields* $\mathcal{T}_n$ and $\overline{\mathcal{T}}_n$ placed at the endpoints of the intervals in an alternate sequence (see [174] for integrable quantum field theories).

When the subsystem $A = A_1 \cup A_2$ is made by two disjoint intervals $A_1 = [u_1, v_1]$ and $A_2 = [u_2, v_2]$, we recall that the expression (1.66) discussed in §1.5.1 expresses $\operatorname{Tr}\rho_A^n$. The function $\mathcal{F}_{2,n}(x)$ depends on the details of the model and therefore it must be computed case by case. From (1.62) and (1.66), one gets that (2.4) for a CFT is given by

$$I^{(n)}_{A_1,A_2} = -\frac{(n+1)c}{6n}\,\log(1-x) + \tilde{I}_n(x)\,, \qquad \tilde{I}_n(x) \equiv \frac{1}{n-1}\log[\mathcal{F}_{2,n}(x)]\,. \tag{2.7}$$

Since the mutual information I_{A_1,A_2} is the limit $n \to 1$ of (2.7), as stated in (2.3), it is the function of x given by

$$I_{A_1,A_2} = -\frac{c}{3}\,\log(1-x) + \tilde{I}_1(x)\,, \qquad \tilde{I}_1(x) \equiv \partial_n \mathcal{F}_{2,n}(x)\big|_{n=1}\,. \tag{2.8}$$

The explicit expression of $\mathcal{F}_{2,n}(x)$ is known for some simple models like the free compact boson and the Ising model (see (1.68) and (1.74)). In these cases $\mathcal{F}_{2,n}(x)$ is written in terms of the Riemann theta function introduced in (1.72).

As a first example, we recall from §1.5 the free boson compactified on a circle of radius r, which has $c = 1$. The corresponding $\mathcal{F}_{2,n}(x)$ for any integer $n \geqslant 2$ is given by [70]

$$\mathcal{F}_{2,n}(x) = \frac{\Theta(\eta\tau_2)\,\Theta(\tau_2/\eta)}{\Theta(\tau_2)^2}\,, \tag{2.9}$$

where $\eta \propto r^2$ and $\tau_2 = \tau_2(x)$ is the $(n-1)\times(n-1)$ purely imaginary period matrix of the Riemann surface which underlies the computation of $\mathrm{Tr}\rho_A^n$, whose elements were introduced in (1.69). We rewrite them here for the sake of comprehension

$$(\tau_2)_{ij} \equiv \mathrm{i}\,\frac{2}{n}\sum_{k=1}^{n-1}\sin(\pi k/n)\,\frac{F_{k/n}(1-x)}{F_{k/n}(x)}\,\cos[2\pi(i-j)k/n]\,, \tag{2.10}$$

where $F_s(x) \equiv {}_2F_1(s, 1-s; 1; x)$, being ${}_2F_1$ the hypergeometric function. Notice that $\mathcal{F}_{2,n}(0) = 1$. Moreover, $\mathcal{F}_{2,n}(x)$ is invariant under $\eta \to 1/\eta$ and $x \to 1-x$ separately. The latter symmetry is related to the well known property $S_A = S_B$ of the entanglement entropy for pure states in the case of A made by two disjoint intervals. It is worth remarking that (2.9) holds for $x \in (0,1)$. Indeed, when $x \in \mathbb{C}$ and $x \notin (0,1)$ the corresponding expression is slightly more complicated [96] and it enters in the computation of the logarithmic negativity for the compact boson.

In order to find the analytic expression of the mutual information for the compact boson, one has to compute $\tilde{I}_1(x)$ in (2.8) with $\mathcal{F}_{2,n}(x)$ given by (2.9). Since performing this analytic computation is still an open problem, we employ the numerical extrapolation method suggested by [171] (see §2.A) to get a result that can be compared with the numerical data found in [63] from the XXZ spin chain.

Before entering in the numerical analysis, it is worth discussing the decompactification regime, which can be addressed analytically. The non compact boson corresponds to the regime $\eta \gg 1$ (or $\eta \ll 1$ because of the symmetry $\eta \leftrightarrow 1/\eta$) in the above expressions. In [70] it has been found that, for $\eta \ll 1$, the terms $\tilde{I}_1(x)$ in (2.8) becomes

$$\tilde{I}_1(x)\big|_{\eta\ll 1} = -\frac{1}{2}\log\eta + \frac{D(x)+D(1-x)}{2}\,, \qquad D(x) \equiv -\int_{-\mathrm{i}\infty}^{\mathrm{i}\infty}\frac{dz}{\mathrm{i}}\,\frac{\pi z}{\sin(\pi z)}\log[F_z(x)]\,. \tag{2.11}$$

The Hamiltonian of the periodic XXZ spin 1/2 chain in a magnetic field h reads [175]

$$H_{\mathrm{xxz}} \equiv \sum_{j=1}^{L}\left(S_j^x S_{j+1}^x + S_j^y S_{j+1}^y + \Delta\, S_j^z S_{j+1}^z\right) - h\sum_{j=1}^{L} S_j^z\,, \tag{2.12}$$

where $S_j^a = \sigma_j^a/2$, being σ_j^a the standard Pauli matrices acting on the spin at the j-th site. The chain has L sites and Δ is the anisotropy. The mutual information for this lattice model has been computed in [63] by direct diagonalization for $L \leqslant 30$.

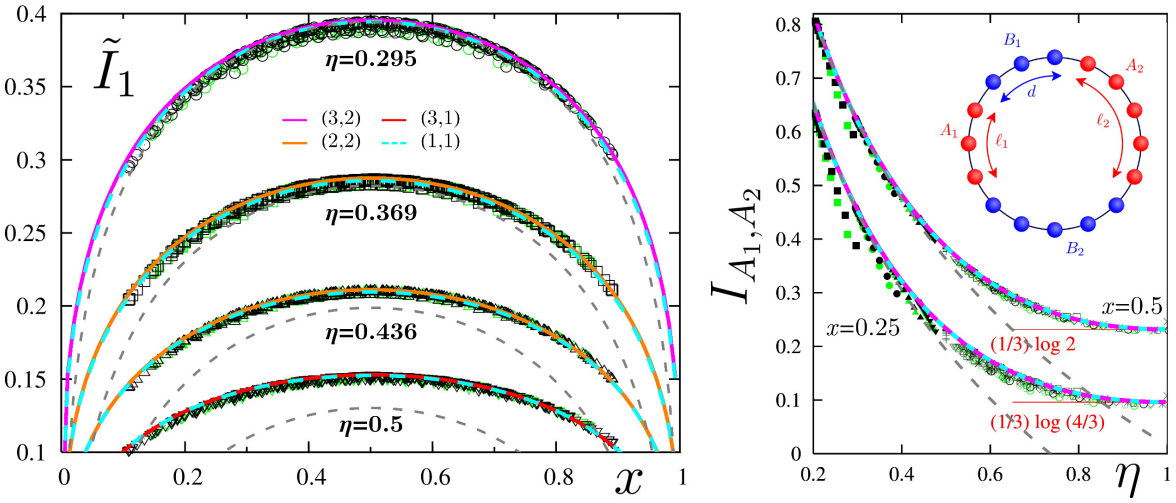

Figure 2.2: Mutual information for the XXZ model. The data points are extracted from [63] and the coloured curves are obtained from the rational interpolations of the analytic expressions (2.7) and (2.9) for the compact boson with the values of (p, q) indicated in the left panel. The dashed grey lines correspond to the decompactification regime, where the analytic continuation (2.11) is known. Left: $\tilde{I}_1$, defined in (2.8), as function of x for various values of η. Right: the mutual information I_{A_1,A_2} as function of η for two fixed values of x.

When $h = 0$ and $-1 < \Delta \leqslant 1$ the model in the continuum is described by the $c = 1$ compact boson with $\eta = 1 - (1/\pi) \arccos \Delta$, while for $h \neq 0$ an explicit formula providing η does not exist and therefore it must be found numerically. The CFT formulas reviewed above can be applied also to the case of a finite system of length L with periodic boundary conditions by employing a conformal mapping from the cylinder to the plane. As final result, the CFT formulas for this case are obtained by considering the expressions for the infinite line and replacing any length ℓ_i with the corresponding chord length $(L/\pi) \sin(\pi \ell_i / L)$ [45].

Let us consider the mutual information of the compactified boson as first example of our extrapolation method. For any fixed value of x, we have that $I^{(n)}_{A_1,A_2}$ are given analytically by (2.7) and (2.9) for any positive integer $n \geqslant 2$, while the corresponding analytic continuation to $n = 1$ is estimated by performing a numerical extrapolation of the known data through a rational function. The latter one is characterized by two positive integer parameters p and q, which are the degrees of the numerator and of the denominator respectively. As explained in §2.A, to perform a rational interpolation characterized by the pair (p, q) we need at least $p + q + 1$ known data. An important technical difficulty that one encounters is the evaluation of the Riemann theta functions for large genus period matrices, i.e. for high values of n. Given the

computational resources at our disposal, we were able to compute Riemann theta functions containing matrices whose size is at most 12. For the compactified boson this corresponds to $n_{\max} = 11$ and therefore $p + q + 1 \leqslant 10$.

In Fig. 2.2 we compared our numerical extrapolations of the analytic expressions of [70] with the numerical data for the XXZ spin chain computed in [63] by exact diagonalization, finding a very good agreement. In the left panel $\tilde{I}_1$ is shown as function of the four-point ratio x for different values of the parameter η, while in the right panel the mutual information I_{A_1,A_2} is shown as function of η for the two fixed configurations of intervals given by $\ell_1 = \ell_2 = d_1 = d_2 = L/4$ ($x = 0.5$) and $2\ell_1 = 2\ell_2 = d_1 = d_2 = L/3$ ($x = 0.25$), being L the total length of the periodic system. All the rational interpolations in the figure exhibit a good agreement with the numerical data, despite the low values of p and q. Increasing these parameters, a better approximation is expected but the result is already stable for these values and we provided two rational interpolations for each curve as a check. Some rational interpolations may display some spurious bahaviour in some regimes of x. As discussed in detail in §2.A, this possibility increases with q. These results have been discarded and we showed only rational interpolations which are well-behaved in the whole domain $x \in (0, 1)$. Notice that rational interpolations that are well-behaved for some η and x could display some bad behaviour changing them. Thus, the values of (p, q) must be chosen case by case. In Fig. 2.2 the dashed grey lines are obtained from the analytic continuation (2.11) found in [70], which corresponds to the decompactification regime and therefore it reproduces the numerical data from the XXZ chain and from the rational interpolations only for small η, as expected.

Another important case where the Rényi entropies of two disjoint intervals have been found analytically is the Ising model [71]. The Hamiltonian of the one dimensional spin chain defining the Ising model in a transverse field is

$$H_{\text{Ising}} \equiv -\sum_{j=1}^{L} \left(\sigma_j^x \sigma_{j+1}^x + h\, \sigma_j^z \right), \tag{2.13}$$

where periodic boundary conditions are imposed. This model has a quantum critical point at $h = 1$ and in the continuum it is a free Majorana fermion with central charge $c = 1/2$. The Rényi entropies for two disjoint intervals on the spin chain (2.13) have been studied in [64] through a Tree Tensor Network algorithm [148] and in [66] through the exact solution of the model in terms of free Majorana fermions. The former method allowed to find also the mutual information.

As for the Rényi entropies for two disjoint intervals in corresponding CFT, by employing known results about bosonization on higher genus Riemann surfaces for $c = 1$ models [51–57], the expression of $\mathcal{F}_{2,n}(x)$ for the Ising model can be written in terms of Riemann theta functions (1.72) evaluated for the period matrix τ_2 in (2.10).

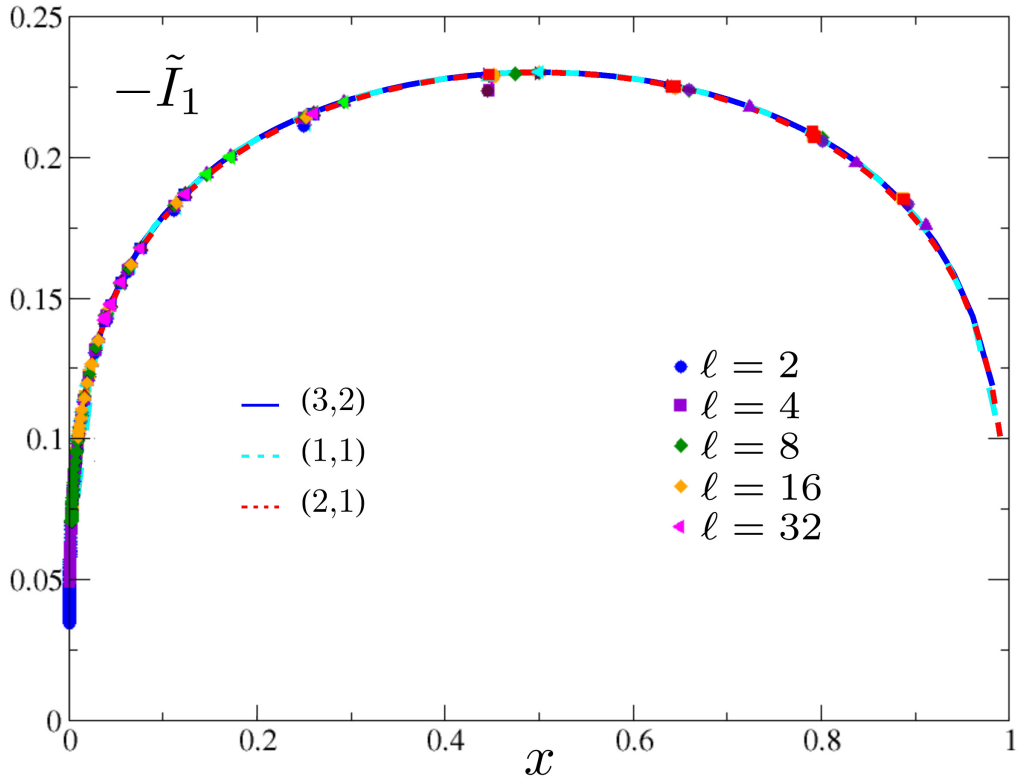

Figure 2.3: Extrapolations for $-\tilde{I}_1$, defined in (2.8), as function of x for the Ising model. The data points are extracted from [64] while the coloured curves are obtained through the rational interpolations with (p, q) indicated.

In particular, $\mathrm{Tr}\,\rho^n_{A_1\cup A_2}$ for the Ising model is given by (1.67) with $c = 1/2$ and [71]

$$\mathcal{F}_{2,n}(x) = \frac{\sum_{\boldsymbol{e}} |\Theta[\boldsymbol{e}](\tau_2)|}{2^{n-1}\,|\Theta(\tau_2)|}\,, \tag{2.14}$$

where the sum is performed over all the possible characteristics $\boldsymbol{e}^{\mathrm{t}} \equiv (\boldsymbol{\varepsilon}^{\mathrm{t}}, \boldsymbol{\delta}^{\mathrm{t}})$, being $\boldsymbol{\varepsilon}$ and $\boldsymbol{\delta}$ two $n-1$ dimensional vectors whose elements are either 0 or $1/2$. Let us remark that in the sum (2.14) only the $2^{n-2}(2^{n-1}+1)$ even characteristics occur. Thus, the mutual information for the Ising model is (2.8) with $\mathcal{F}_{2,n}(x)$ given by (2.14). Similarly to the case of the compact boson, also for the Ising model we are not able to compute $\tilde{I}_1(x)$ analytically and therefore we perform a numerical extrapolation through the rational interpolation method described in §2.A.

In Fig. 2.3 we show $-\tilde{I}_1(x)$ as function of $x \in (0, 1)$, which can be found by considering two disjoint intervals of equal length, and compare the numerical data obtained in [64] with the curve found through the numerical extrapolation of the correspond-

ing formula containing (2.14) through rational interpolations. Since (2.14) contains Riemann theta functions, we cannot consider high values for n, like for the compact boson. Moreover, in this case one faces an additional complication with respect to the compact boson because in (2.14) the sum over all the even characteristics occurs and the number of terms in the sum grows exponentially with n. Given our computational power, we have computed the Rényi entropies up to $n = 7$ and in Fig. 2.3 we show the rational interpolations found by choosing three different pairs (p, q) which are well-behaved among the available ones. Since the curves coincide, the final result is quite stable and, moreover, the agreement with the numerical data found in [64] through the Tree Tensor Network is very good.

2.3 Three disjoint intervals

In this section we partially extend the analysis done in §2.2 by considering the case of three disjoint intervals. After a brief review of the analytic results known for a generic number N of disjoint intervals, we focus on $N = 3$ and perform some numerical extrapolations for the non compact boson and for the Ising model.

Given a the spatial subsystem $A = \cup_{i=1}^{N} A_i$ made by the union of the N disjoint intervals $A_1 = [u_1, v_1]$, ..., $A_N = [u_N, v_N]$, a generalization of (2.4) to $N \geqslant 2$ reads **[ctt-14]**

$$I^{(n)}_{A_1,\cdots,A_N} \equiv \frac{(-1)^N}{n-1} \log R_{N,n} \,, \qquad R_{N,n} \equiv \prod_{p=1}^{N} \prod_{\sigma_{N,p}} \left(\operatorname{Tr} \rho^n_{\sigma_{N,p}} \right)^{(-1)^{N-p}} \,, \tag{2.15}$$

where $\sigma_{N,p}$ denotes the union of a generic choice of $1 \leqslant p \leqslant N$ intervals among the N ones. It is straightforward to observe that the analytic continuation $n \to 1$ of (2.15), i.e.

$$I_{A_1,\ldots,A_N} \equiv \lim_{n \to 1} I^{(n)}_{A_1,\ldots,A_N} \,, \tag{2.16}$$

provides a natural generalization to $N \geqslant 2$ of the mutual information (2.3). We find it useful to normalise the quantities introduced in (2.15) and (2.16) by themselves evaluated for some fixed configuration of intervals, namely

$$R^{\text{norm}}_{N,n} \equiv \frac{R_{N,n}}{R_{N,n}\big|_{\text{fixed}}} \,, \qquad I^{\text{sub}}_N \equiv I_N - I_N\big|_{\text{fixed}} = \lim_{n \to 1} R^{\text{norm}}_{N,n} \,, \tag{2.17}$$

where we have adopted the shorthand notation $I_N \equiv I_{A_1,\ldots,A_N}$.

In two dimensional CFTs, the expression of $\operatorname{Tr} \rho^n_A$ for N disjoint intervals can be written as a $2N$-point function of twist fields [45, 46]. Similarly to the two intervals case, the global conformal invariance cannot fix the dependence on u_i and v_i. In

particular, given the endpoints $u_1 < v_1 < \cdots < u_N < v_N$, one can employ the following conformal map

$$w_N(z) = \frac{(u_1 - z)(u_N - v_N)}{(u_1 - u_N)(z - v_N)}\,, \tag{2.18}$$

which sends $u_1 \to 0$, $u_N \to 1$ and $v_N \to \infty$. The remaining endpoints are mapped into the $2N-3$ four-point ratios $x_1 = w_N(v_1)$, $x_2 = w_N(u_2)$, $x_3 = w_N(v_2), \ldots, x_{2N-3} = w_N(v_{N-1})$ which are invariant under $SL(2,\mathbb{C})$. Notice that $x_j \in \mathbb{R}$ and the order is preserved, namely $0 < x_1 < x_2 < \cdots < x_{2N-3} < 1$.

The global conformal invariance allows us to write $\operatorname{Tr}\rho_A^n$ for N disjoint intervals as follows [46]

$$\operatorname{Tr}\rho_A^n = \langle \prod_{i=1}^{N} \mathcal{T}_n(u_i)\bar{\mathcal{T}}_n(v_i)\rangle = c_n^N \left| \frac{\prod_{i<j}(u_j - u_i)(v_j - v_i)}{\prod_{i,j}(v_j - u_i)} \right|^{2\Delta_n} \mathcal{F}_{N,n}(\boldsymbol{x})\,, \tag{2.19}$$

where $i, j = 1, \ldots, N$, the scaling dimension Δ_n is given in (1.62) and $\boldsymbol{x}$ is the vector whose elements are the $2N-3$ four-point ratios introduced above. It is worth remarking that $\mathcal{F}_{N,n}(\boldsymbol{x})$ encodes the full operator content of the model and therefore its computation depends on the features of the model. From (2.15) and (2.19), one finds that $R_{N,n}$ and $R_{N,n}^{\text{norm}}$ in CFT become respectively [94]

$$R_{N,n}(\boldsymbol{x}) = \prod_{p=2}^{N} \prod_{\sigma_{N,p}} \left[\mathcal{F}_{p,n}(\boldsymbol{x}^{\sigma_{N,p}})\right]^{(-1)^{N-p}}, \qquad R_{N,n}^{\text{norm}}(\boldsymbol{x}) = \frac{R_{N,n}(\boldsymbol{x})}{R_{N,n}(\boldsymbol{x}_{\text{fixed}})}\,, \tag{2.20}$$

where $\boldsymbol{x}^{\sigma_{N,p}}$ is the vector made by the $2p-3$ four-point ratios obtained with the endpoints of the p intervals selected by $\sigma_{N,p}$.

The function $\mathcal{F}_{N,n}(\boldsymbol{x})$ for the compactified boson has been studied in [94] by generalizing the construction of [70] and, again, it is written in terms of the Riemann theta function (1.72). For $N > 2$ disjoint intervals the Riemann surface occurring in the computation of $\operatorname{Tr}\rho_A^n$ has genus $g = (N-1)(n-1)$. The corresponding $g \times g$ period matrix $\tau_N = \mathcal{R} + \mathrm{i}\,\mathcal{I}$, which is symmetric and complex with positive imaginary part, is complicated and, since we do not find instructive to report it here, we refer to [94] for any detail about it. The expression of $\mathcal{F}_{N,n}(\boldsymbol{x})$ for the compactified boson reads [51–57, 94]

$$\mathcal{F}_{N,n}(\boldsymbol{x}) = \frac{\Theta(T_\eta)}{|\Theta(\tau_N)|^2}\,, \qquad T_\eta \equiv \begin{pmatrix} \mathrm{i}\,\eta\,\mathcal{I} & \mathcal{R} \\ \mathcal{R} & \mathrm{i}\,\mathcal{I}/\eta \end{pmatrix}, \tag{2.21}$$

where η is the parameter containing the compactification radius introduced in §2.2. Notice that (2.21) is invariant under $\eta \leftrightarrow 1/\eta$.

As done in §2.2 for the two intervals case, also for N disjoint intervals it is interesting to consider the decompactification regime. When $\eta \gg 1$ the expression in (2.21) becomes

$$\mathcal{F}_{N,n}^{\eta\to\infty}(\boldsymbol{x}) = \frac{\eta^{g/2}}{\sqrt{\det(\mathcal{I})}\,|\Theta(\tau_N)|^2} \equiv \eta^{g/2}\,\widehat{\mathcal{F}}_{N,n}(\boldsymbol{x})\,. \tag{2.22}$$

For computational purposes, it is important to observe that in (2.22) the Riemann theta function is evaluated for τ_N, which is $g \times g$, while for finite η, when (2.21) holds, the matrix occurring in the Riemann theta function is $2g \times 2g$. This implies that for the non compact boson we can reach higher values of n and therefore the corresponding numerical extrapolation is more precise. In the decompactification regime we can also appreciate the convenience of considering the normalization (2.17). Indeed, plugging (2.22) into (2.20) one obtains an expression which is η independent

$$\widehat{R}_{N,n}^{\text{norm}}(\boldsymbol{x}) \equiv \frac{R_{N,n}^{\eta\to\infty}(\boldsymbol{x})}{R_{N,n}^{\eta\to\infty}(\boldsymbol{x}_{\text{fixed}})} = \prod_{p=2}^{N}\prod_{\sigma_{N,p}}\left[\frac{\widehat{\mathcal{F}}_{p,n}(\boldsymbol{x}^{\sigma_{N,p}})}{\widehat{\mathcal{F}}_{p,n}(\boldsymbol{x}_{\text{fixed}}^{\sigma_{N,p}})}\right]^{(-1)^{N-p}}\,. \tag{2.23}$$

As for the Ising model, since the results of [51–57] about the bosonization on higher genus Riemann surfaces for $c = 1$ models hold for a generic genus, we can straightforwardly write the generalization to $N \geqslant 2$ of the $N = 2$ formula (2.14). Indeed, given the period matrix τ_N employed for the compact boson in (2.21), we have that $\operatorname{Tr}\rho_A^n$ for the Ising model is (2.19) with $c = 1/2$ and [51–57, 94]

$$\mathcal{F}_{N,n}(\boldsymbol{x}) = \frac{\sum_{\boldsymbol{e}}|\Theta[\boldsymbol{e}](\tau_N)|}{2^g\,|\Theta(\tau_N)|}\,. \tag{2.24}$$

The Riemann theta functions in this formula are evaluated for the $g \times g$ period matrix and a sum over all the characteristics occurs. It is worth remarking that the Riemann theta functions in (2.24) with odd characteristics vanish and therefore the sum contains $2^{g-1}(2^g + 1)$ terms. In [94] the formula (2.24) has been checked numerically on the lattice for $n = 2$, various N and different configurations of intervals by employing the Matrix Product States. To our knowledge, numerical results for I_N with $N \geqslant 3$ are not available in the literature for the critical Ising chain in transverse field.

In this chapter, for simplicity, we consider only $N = 3$ disjoint intervals and therefore let us specify some of the formulas given above to this case. The generalization of the mutual information to the case of three disjoint intervals is given by

$$I_{A_1,A_2,A_3} \equiv S_{A_1} + S_{A_2} + S_{A_3} - S_{A_1\cup A_2} - S_{A_1\cup A_3} - S_{A_2\cup A_3} + S_{A_1\cup A_2\cup A_3} = \lim_{n\to 1} I^{(n)}_{A_1,A_2,A_3}\,, \tag{2.25}$$

where $I^{(n)}_{A_1,A_2,A_3}$ can be written by specifying the expressions in (2.15) to $N = 3$, namely

$$I^{(n)}_{A_1,A_2,A_3} \equiv \frac{\log(R_{3,n})}{1-n} = S^{(n)}_{A_1} + S^{(n)}_{A_2} + S^{(n)}_{A_3} - S^{(n)}_{A_1\cup A_2} - S^{(n)}_{A_1\cup A_3} - S^{(n)}_{A_2\cup A_3} + S^{(n)}_{A_1\cup A_2\cup A_3}\,, \tag{2.26}$$

with

$$R_{3,n} \equiv \frac{\operatorname{Tr}\rho^n_{A_1\cup A_2\cup A_3}\big(\operatorname{Tr}\rho^n_{A_1}\operatorname{Tr}\rho^n_{A_2}\operatorname{Tr}\rho^n_{A_3}\big)}{\operatorname{Tr}\rho^n_{A_1\cup A_2}\operatorname{Tr}\rho^n_{A_1\cup A_3}\operatorname{Tr}\rho^n_{A_2\cup A_3}}\,. \tag{2.27}$$

Considering CFTs, when $N = 3$ the vector $\boldsymbol{x} = (x_1, x_2, x_3)$ is made by three four-point ratios and (2.20) becomes

$$R_{3,n}(\boldsymbol{x}) = \frac{\mathcal{F}_{3,n}(x_1,x_2,x_3)}{\mathcal{F}_{2,n}(\frac{x_1(x_3-x_2)}{x_2(x_3-x_1)})\,\mathcal{F}_{2,n}(x_1)\,\mathcal{F}_{2,n}(\frac{x_3-x_2}{1-x_2})}\,, \tag{2.28}$$

where $\mathcal{F}_{3,n}(\boldsymbol{x})$ is (2.19) for $N = 3$ and $\mathcal{F}_{2,n}(x)$ has been introduced in (1.67).

The non compact boson is the CFT describing the massless harmonic chain in the continuum. The Hamiltonian of the harmonic chain with L lattice sites and with nearest neighbour interaction reads

$$H = \sum_{n=0}^{L-1}\left(\frac{1}{2M}\,p_n^2 + \frac{M\omega^2}{2}\,q_n^2 + \frac{K}{2}(q_{n+1}-q_n)^2\right), \tag{2.29}$$

where periodic boundary conditions are imposed. Rewriting (2.29) in terms of $a \equiv \sqrt{M/K}$ and ω through a canonical transformation, one can observe that it provides the lattice discretization of the free boson with mass ω and lattice spacing a. Thus, the continuum limit of the $\omega = 0$ case is the decompactified boson discussed above. The method to compute Rényi entropies for the lattice model (2.29) is well known [145, 176–181] and $\operatorname{Tr}\rho^n_A$ can be found from the correlators $\langle q_r q_s\rangle$ and $\langle p_r p_s\rangle$. Let us recall that setting ω to zero leads to a divergent expression for $\langle q_r q_s\rangle$ because of the zero mode occurring for periodic boundary conditions. In [94] the method discussed in [145, 176–181] has been applied to perform various checks of the CFT formulas for the non compact boson at fixed n. Moreover, also I^{sub}_N has been found from the harmonic chain data, but a comparison with the analytic results has not been done because the analytic continuation of the corresponding Rényi entropies is not known yet. Indeed, the Riemann theta function occurs in (2.22) and its analytic continuation in n is still an open problem. As for the values of ω, in [94] it has been checked that $\omega L = 10^{-5}$ is small enough to capture the CFT regime through the periodic harmonic chain. The numerical data for the periodic harmonic chain have been found by setting $M = K = 1$ and $\omega L = 10^{-5}$ in (2.29). The same quantities evaluated for $\omega L = 10^{-3}$ turned out to be indistinguishable.

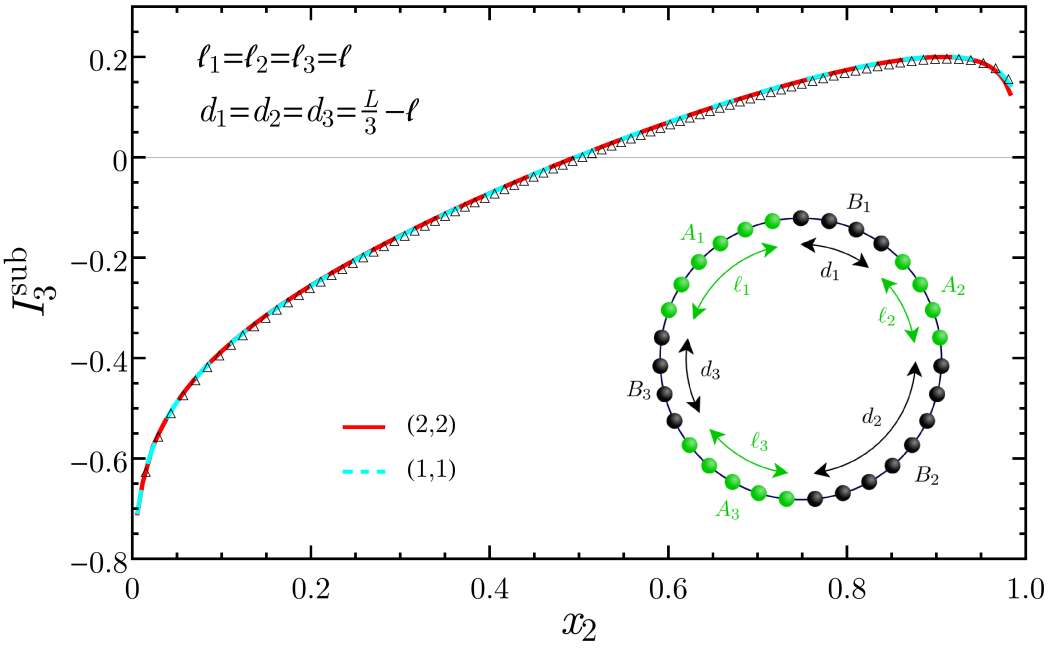

Figure 2.4: Extrapolations of $I_3^{\rm sub}$ (see (2.17) with $N = 3$) as function of the four-point ratio x_2 for the non compact boson. The points are the data obtained in [94] from the periodic harmonic chain (2.29) with $L = 5000$ and $\omega L = 10^{-5}$. The configuration chosen here is made by equal intervals separated by equal distances, while the fixed configuration normalizing $I_3^{\rm sub}$ is given in the text. The coloured lines correspond to two different extrapolations obtained through rational interpolations with (p, q) indicated.

In the remaining part of this section we focus on the case of three disjoint intervals and perform some numerical extrapolations of the analytic results reviewed above to $n = 1$ through rational interpolations, comparing them with the corresponding numerical data from the lattice models, whenever they are available.

In Figs. 2.4 and 2.5 we consider $I_3^{\rm sub}$ (see (2.17)) for the decompactified boson, comparing the results obtained for the periodic harmonic chain with the numerical extrapolations found for the corresponding configurations of intervals obtained through the rational interpolation (see §2.A). The dots are numerical data obtained in [94] from the periodic harmonic chain given by (2.29) with $L = 5000$ and different sets of data correspond to different configurations of the three intervals. In particular, referring to the inset of Fig. 2.4 for the notation, the configuration considered in Fig. 2.4 is the one where all intervals are equal $\ell_1 = \ell_2 = \ell_3$ and they are placed at the same distance $d_1 = d_2 = d_3 = L/3 - \ell$. Varying the length ℓ of the intervals, one

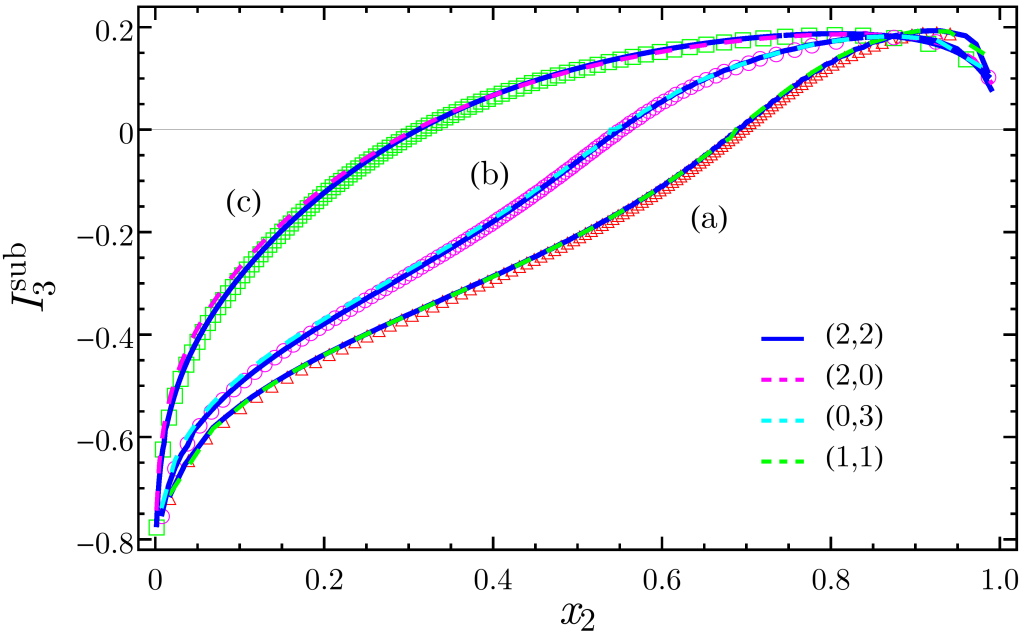

Figure 2.5: Extrapolations of $I_3^{\rm sub}$ for the non compact boson. The harmonic chain is the same one of Fig. 2.4 while the configurations of intervals are given by (2.30). The data for the periodic harmonic chain have been extracted from [94].

finds the result, which is plotted as function of the four-point ratio x_2. In Fig. 2.5, the data are labeled according to the following configurations of the three intervals:

$$\begin{aligned} &\text{(a)} \quad \ell_i = \lambda_i \ell,\ d_i = (L - \textstyle\sum_{i=1}^{3} \ell_i)/3 \text{ with } \lambda_1 = 1,\ \lambda_2 = 2,\ \lambda_3 = 8; \\ &\text{(b)} \quad \text{with } \lambda_1 = 1,\ \lambda_2 = 11,\ \lambda_3 = 11; \\ &\text{(c)} \quad \ell_i = \gamma_i \ell,\ d_i = \gamma_i d,\ d = L/(\textstyle\sum_{i=1}^{3} \gamma_i) - \ell \text{ with } \gamma_1 = 1,\ \gamma_2 = 3,\ \gamma_3 = 6; \end{aligned} \tag{2.30}$$

where the parameter ℓ is varied and the results are plotted as functions of $x_2 \in (0, 1)$. As for the fixed configuration normalizing $I_3^{\rm sub}$ in (2.17) we have chosen $\ell_1 = \ell_2 = \ell_3 = d_1 = d_2 = \text{int}(L/6)$, where int(...) denotes the integer part. The coloured curves in Figs. 2.4 and 2.5 are the numerical extrapolations of the CFT formulas for the non compact boson (2.22) and (2.23) through the rational interpolation method. For each set of data, we show two different rational interpolations which are well-behaved in order to check the stability of the result. The differences between different well-behaved rational interpolations are very small and the agreement with the numerical data from the harmonic chain is very good, supporting the validity of the extrapolating method. In Figs. 2.4 and 2.5 we have employed $2 \leqslant n \leqslant 6$. It is worth remarking at this point that the Riemann theta functions occurring in the CFT expression (2.28) for the non compact boson contain at most $g \times g$ matrices ($g = 2(n-1)$ for $N = 3$)

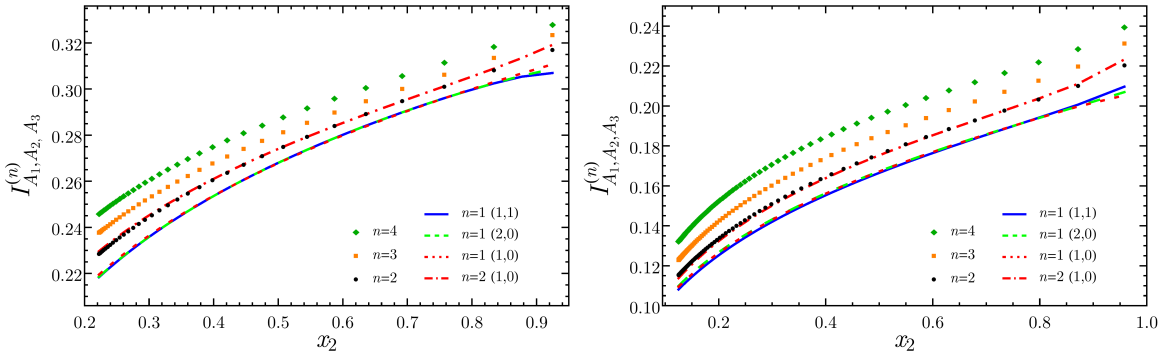

Figure 2.6: Extrapolations of I_{A_1,A_2,A_3}, defined in (2.25), for the Ising model. Two configurations of intervals have been considered, namely (2.31) with $\alpha = 0.25$ (left) and $\alpha = 2$ (right). The dots correspond to $I^{(n)}_{A_1,A_2,A_3}$ in (2.26) with $n \in \{2,3,4\}$ while the lines are the extrapolations obtained through the rational interpolation method with the values of (p,q) indicated. The dot-dashed line is the extrapolation to $n = 2$ performed as a check of the method, while the remaining lines correspond to I_{A_1,A_2,A_3}.

while for the compact boson their size is at most $2g \times 2g$ (see (2.21)). From the computational viewpoint, this is an important difference because the higher is n that can be addressed, the higher is the number of different (p,q) that can be considered in the rational interpolations. Thus, the maximum n that we can deal with is related to the maximum size of the matrices in the Riemann theta functions occurring in the model. Nevertheless, from Figs. 2.4 and 2.5 we observe that, for this case, rational interpolations with low values of (p,q) are enough to capture the result expected from the lattice data.

In Fig. 2.6 we show I_{A_1,A_2,A_3}, defined in (2.25), for the Ising model. We have considered the following configurations of three intervals specified by a parameter α (see the inset of Fig. 2.4 for the notation)

$$\text{(d)} \qquad \ell_i = \ell,\; d_1 = d_2 = \alpha\ell,\; d_3 = L - (3+2\alpha)\ell\,. \tag{2.31}$$

In particular, the results in Fig. 2.6 correspond to $\alpha = 0.25$ (left panel) and $\alpha = 2$ (right panel), where the dots denote the values of $I^{(n)}_{A_1,A_2,A_3}$ for $n \in \{2,3,4\}$. Unfortunately, with the computational resources at our disposal, we could not compute Rényi entropies for higher values of n. Indeed, besides the problem of computing the Riemann theta function numerically for large period matrices, the additional obstacle occurring for the Ising model is that the number of elements in the sum (2.24) grows exponentially with n. Given the few n's available, only few rational interpolations can be employed to approximate the analytic continuation to $n = 1$ and they are depicted in Fig. 2.6 through solid and dashed lines (in general we never use $(p,q) = (0,1)$

because is often not well-behaved).

It is interesting to observe that the three different rational interpolations provide the same extrapolation to $n = 1$ for a large range of x_2 (they differ when x_2 is close to 1). Since, to our knowledge, numerical results about I_{A_1,A_2,A_3} for the Ising model are not available in the literature, the curves in Fig. 2.6 are predictions that would be interesting to test through other methods. We remark that we are not guaranteed that this extrapolation method provides the correct analytic continuation. Nevertheless, the fact that extrapolations with different values of (p, q) give very close outputs is a strong indication that the result should be trusted, assuming that no singularities occurs for real n between 1 and the maximum value of n employed in the extrapolations. Another check of the reliability of the numerical method is the following: we have performed rational interpolations considering only $n \in \{3, 4\}$ to extrapolate the value at $n = 2$, which is known analytically. Since only two points are available, only the rational interpolation with $(p, q) = (1, 0)$ can be done, which is given by the dot-dashed curve in Fig. 2.6. Despite the roughness of the extrapolation due to the few input points, the agreement with the expected values computed with the analytic expression (black dots) is very good.

2.4 Entanglement negativity of two disjoint intervals

In this section we consider the logarithmic negativity of two disjoint intervals for the non compact massless free boson, whose analytic formula is not known.

The method to compute the logarithmic negativity $\mathcal{E}$ in quantum field theory and in conformal field theory has been described in [95, 96] (see [102] for the finite temperature case) and we refer to these papers for all the details and the discussion of further cases. In order to briefly mention the main idea, let us consider a subsystem $A = \cup_{i=1}^{N} A_i$ made by N disjoint intervals $A_i = [u_i, v_i]$. The traces $\mathrm{Tr}\,\rho_A^n$ in CFT are given by the correlators of twist fields in (2.19). Denoting by $A_0 \subsetneq A$ a set of $N_0 < N$ disjoint intervals among the ones in A and by $\rho_A^{T_0}$ the partial transpose of ρ_A with respect to A_0, we have that $\mathrm{Tr}(\rho_A^{T_0})^n$ in CFT is the correlation function of twist fields obtained by placing $\mathcal{T}_n$ in u_i and $\bar{\mathcal{T}}_n$ in v_i when $A_i \in A \setminus A_0$, and $\bar{\mathcal{T}}_n$ in u_i and $\mathcal{T}_n$ in v_i when $A_i \in A_0$. The corresponding logarithmic negativity $\mathcal{E}$, which measures the entanglement between A_0 and $A \setminus A_0$, can be computed by considering the sequence of the even integers n_e and taking the replica limit (2.6). Configurations containing adjacent intervals are obtained as limiting cases and the fields $\mathcal{T}_n^2$ and $\bar{\mathcal{T}}_n^2$ occur.

In the simplest example, starting from two disjoint intervals $A = A_1 \cup A_2$, whose endpoints are ordered as $u_1 < v_1 < u_2 < v_2$ like in §2.2, one considers e.g. the partial

transpose with respect to A_2. In this case we have that [95, 96]

$$\begin{aligned} \mathrm{Tr}(\rho_A^{T_2})^n &= \langle \mathcal{T}_n(u_1)\bar{\mathcal{T}}_n(v_1)\bar{\mathcal{T}}_n(u_2)\mathcal{T}_n(v_2)\rangle & (2.32) \\ &= c_n^2 \left[\frac{(u_2-u_1)(v_2-v_1)}{(v_1-u_1)(v_2-u_2)(u_2-v_1)(v_2-u_1)}\right]^{2\Delta_n} \mathcal{G}_n(x)\,, & (2.33) \end{aligned}$$

where $x \in (0,1)$ is the four-point ratio (**??**) and Δ_n has been introduced in (1.62). Since (2.32) is obtained from (1.66) by exchanging $\mathcal{T}_n \leftrightarrow \bar{\mathcal{T}}_n$ for the endpoints of A_2, the function $\mathcal{G}_n$ in (2.33) is related to the function $\mathcal{F}_{2,n}$ in (1.67) as follows

$$\mathcal{G}_n(x) \equiv (1-x)^{4\Delta_n}\, \mathcal{F}_{2,n}\big(x/(x-1)\big)\,, \tag{2.34}$$

where we remark that $x/(x-1) \in (-\infty, 0)$. Plugging (2.34) into (2.33) and taking the replica limit (2.6) of the resulting expression, since $\Delta_1 = 0$ and $c_1 = 1$, we find that the logarithmic negativity of two disjoint intervals in CFT is given by

$$\mathcal{E}(x) = \lim_{n_e \to 1} \log \mathcal{G}_{n_e}(x) = \lim_{n_e \to 1} \log \mathcal{F}_{2,n_e}\big(x/(x-1)\big)\,, \tag{2.35}$$

telling us that the logarithmic negativity is scale invariant, being a function of the ratio x only. In order to get rid of the prefactor in (2.33), it is convenient to consider the following ratio

$$\widetilde{R}_n \equiv \frac{\mathrm{Tr}(\rho_A^{T_2})^n}{\mathrm{Tr}(\rho_A)^n} = \frac{\mathcal{G}_n(x)}{\mathcal{F}_{2,n}(x)} = (1-x)^{4\Delta_n}\, \frac{\mathcal{F}_{2,n}\big(x/(x-1)\big)}{\mathcal{F}_{2,n}(x)}\,, \tag{2.36}$$

where (2.34) has been employed in the last step. Since $\mathcal{F}_{2,1}(x) = 1$ for $x \in (0,1)$ because of the normalization of ρ_A, the logarithmic negativity can be found also by taking the replica limit of (2.36), namely

$$\mathcal{E}(x) = \log \lim_{n_e \to 1} \widetilde{R}_{n_e}(x)\,, \tag{2.37}$$

Notice that, since for $n = 2$ we have that $\mathcal{T}_2 = \bar{\mathcal{T}}_2$, one concludes that $\widetilde{R}_2 = 1$ identically.

The simplest model we can deal with for which analytic expressions for $\mathrm{Tr}(\rho_A^{T_2})^n$ are available in the literature is the non compact free massless boson. For this model it has been found that [95, 96]

$$\widetilde{R}_n(x) = (1-x)^{(n-1/n)/3} \left[\frac{\prod_{k=1}^{n-1} F_{k/n}(x) F_{k/n}(1-x)}{\prod_{k=1}^{n-1} \mathrm{Re}\big(F_{k/n}(\frac{x}{x-1})\bar{F}_{k/n}(\frac{1}{1-x})\big)}\right]^{1/2}. \tag{2.38}$$

When $n = n_e$ is even, it could be convenient to isolate the term $k/n = 1/2$ in the product in order to get rid of the square root in the remaining part of the product

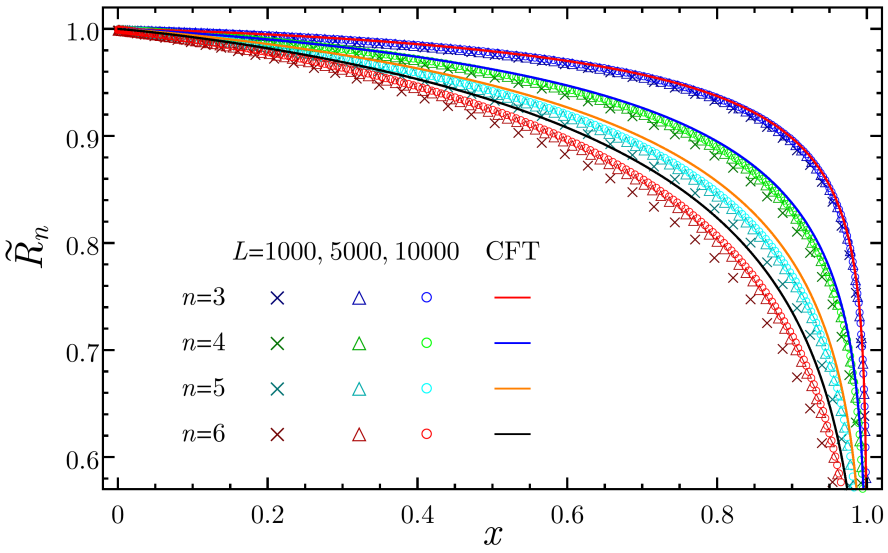

Figure 2.7: The ratio $\widetilde{R}_n(x)$ in (2.36) for the non compact boson. The data points come from the periodic harmonic chain with $\omega L = 10^{-5}$, while the curves are given by CFT formula (2.38).

because of the symmetry $k \leftrightarrow n-k$ in $F_{k/n}$. Notice that when $n = 2$ we have that $\widetilde{R}_2(x) = 1$ identically.

In Fig. 2.7 we compare the CFT result (2.38) for $\widetilde{R}_n(x)$ with the corresponding quantity computed for the periodic harmonic chain (2.29), where $\mathrm{Tr}(\rho_A^{T_2})^n$ is computed through the correlators $\langle q_r q_s \rangle$ and $\langle p_r p_s \rangle$ as explained in [145, 176–181]. Notice that we have improved this check with respect to [96], indeed the data in Fig. 2.7 correspond to chains whose total length L is significantly larger than the ones considered in [96], where $L \leqslant 300$. All the data reported in the figure have $\omega L = 10^{-5}$. We have considered also harmonic chains with $\omega L = 10^{-3}$ and $L = 10000$, finding the same results reported in Fig. 2.7 for $L = 10000$. For $n = 3$ the agreement is very good, while it gets worse as n increases. This is expected because of the unusual corrections to the scaling [139, 140, 182].

It is more convenient to consider (2.35) than (2.37) for the computation of the replica limit, and for the logarithmic negativity of the non compact boson we have that [96]

$$\mathcal{E}(x) \;=\; -\frac{1}{2}\log\big[K(x)K(1-x)\big] - \frac{3}{8}\log(1-x) + \log(\pi/2) - \lim_{n_e\to 1}\sum_{k=1}^{n_e/2-1}\log G_{k/n_e}(x)\,, \tag{2.39}$$

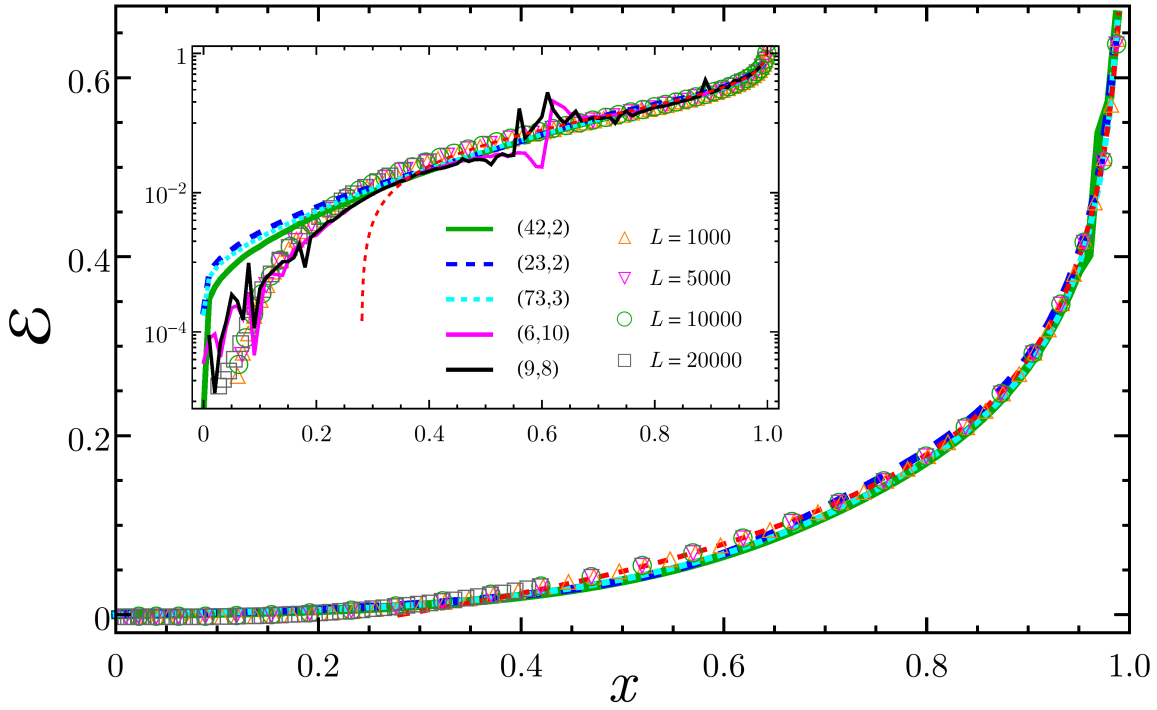

Figure 2.8: Logarithmic negativity of two disjoint intervals for the non compact boson (2.39) as function of the four-point ratio x. The dots are numerical data obtained for the periodic harmonic chains with $\omega L = 10^{-5}$ and increasing total lengths. All data collapse on the same curve, which corresponds to the continuum limit. The red dashed curve is the analytic continuation found in [96] in the regime $x \to 1^-$. The remaining curves are extrapolations obtained from different rational interpolations having (p, q) indicated. In the inset we show the same plot in logarithmic scale in order to highlight the behaviour of the different extrapolated curves when $x \sim 0$.

where

$$G_\beta(x) \equiv {}_2F_1(\beta,\beta,1;x)\left[\frac{\Gamma(1-2\beta)}{\Gamma(1-\beta)^2}\,(1-x)^\beta\,{}_2F_1(\beta,\beta,2\beta;1-x) - (\beta \leftrightarrow 1-\beta)\right], \tag{2.40}$$

being $K(x)$ the elliptic integral of the first kind. The sum in (2.39) is defined for $n_e \geqslant 4$ and for $n_e = 2$ that term is zero. The analytic continuation in (2.39) is not known for the entire range $x \in (0, 1)$. In [96] the analytic continuation has been found for the regime $x \to 1^-$, obtaining an expression that surprisingly works down to $x \sim 0.3$ (see the dashed red curve in Fig. 2.8).

Here we numerically extrapolate $\mathcal{E}(x)$ through the formula (2.39) by using the rational interpolation method, which has been discussed in §2.A and employed in

the previous sections for the entanglement entropy of disjoint intervals. It is worth remarking that, since the replica limit (2.6) for $\mathcal{E}(x)$ involves only even n's, to perform a rational interpolation characterized by some (p, q) we need higher values of n with respect to the ones employed for the entanglement entropy in the previous sections. In particular, for the logarithmic negativity $p + q + 1 \leqslant n_{e,\max}/2$.

In Fig. 2.8 we report the extrapolations found for some values of (p, q). Since the numerical data from the harmonic chain are accurate enough to provide the curve in the continuum limit that should be found through the analytic continuation (2.39), we can check the reliability of our numerical extrapolations against them. For the non compact boson the expression (2.40) is not difficult to evaluate numerically. Thus, we can deal with high values of n and therefore we have many possibilities for (p, q). It turns out that an accurate extrapolation for the logarithmic negativity requires high values of p and q, in particular for the regime of small intervals $x \sim 0$ (see Fig. 2.11 in §2.A for extrapolations having low p and q). As already remarked in [95, 96], the behaviour of $\mathcal{E}(x)$ when $x \sim 0$ is not power-like. We observed, as a general behaviour, that increasing q leads to extrapolations which are closer to the numerical data, but spurious fluctuations or even singularities in some regimes of x can occur (see the black and magenta curves in the inset of Fig. 2.8, and the dashed magenta and cyan curves in Fig. 2.11). This happens whenever one of the q poles of the rational function is close to the range $(1, n_{\max})$ of the interpolated data and not too far from $n = 1$ (it may be real or have a small imaginary part). Let us emphasize that these singularities are simply a feature of the extrapolating function and have nothing to do with true singularities of the analytic continuation. If any true singularity is present in the extrapolating region, we do not expect the method to be able to decribe it correctly. More details are reported in §2.A. Taking low q's, one usually gets smooth curves but even high values of p's are not sufficient to capture the behaviour of $\mathcal{E}(x)$ when $x \sim 0$.

Thus, the logarithmic negativity is more difficult to find through the rational interpolation method than the entanglement entropy. Indeed, while for the latter one few Rényi entropies are enough to capture the expected result in a stable way, for the logarithmic negativity more input data are needed to reproduce the regime of distant intervals. Maybe other numerical methods are more efficient. It is worth remarking that the fact that high values of n's in $\mathrm{Tr}(\rho_A^{T_2})^n$ are required to perform accurate extrapolations of the logarithmic negativity leads to a computational obstacle whenever $\mathcal{G}_n(x)$ in (2.33) is written in terms of Riemann theta functions, like for the compact boson [96] and for the Ising model [97, 98]. Given our computational resources, we have not been able to deal with those analytic expressions for n high enough to guarantee convincing extrapolations.

Appendices

2.A Rational interpolations

In this appendix we discuss the numerical method that we have employed throughout this chapter, which is based on rational interpolations, and the issues we encountered to address the replica limits for the entanglement entropy and negativity considered in the main text. Its use in this context has been first suggested in [171].

The rational interpolation method consists in constructing a rational function which interpolates a finite set of given points labeled by a discrete variable. Once the rational function is written, one simply lets the discrete variable assume all real values. The needed extrapolation is found by just evaluating the rational function obtained in this way for the proper value of the variable.

For the quantities we are interested in, the discrete variable is an integer number n. As a working example, let us consider the case of two disjoint intervals, where the variable $x \in (0,1)$ characterizes the configuration of intervals. For any integer $n \geqslant 2$ we have a real function of x and typically we have access only to $n \leqslant n_{\max}$ for computational difficulties. The rational function interpolating the given data reads

$$W^{(n)}_{(p,q)}(x) \equiv \frac{P(x;n)}{Q(x;n)} \equiv \frac{a_0(x) + a_1(x)n + a_2(x)n^2 + \cdots + a_p(x)n^p}{b_0(x) + b_1(x)n + b_2(x)n^2 + \cdots + b_q(x)n^q}\,, \tag{2.41}$$

being $p \equiv \deg(P)$ and $q \equiv \deg(Q)$ the degrees of the numerator and of the denominator respectively as polynomials in n. The extrapolations are performed pointwise in the domain $x \in (0,1)$. Thus, for any given $x \in (0,1)$, in (2.41) we have $p+q+2$ coefficients to determine. Nevertheless, since we can divide both numerator and denominator by the same number fixing one of them to 1, the number of independent parameters to find is $p+q+1$. Once the coefficients in (2.41) have been found, the extrapolation is easily done by considering n real and setting it to the needed value. It is important to stress that, having access only to a limited number m of data points, we can only perform rational interpolations whose degrees (p,q) are such that $p+q+1 \leqslant m$. This method is implemented in *Wolfram Mathematica* through the *Function Approximations* package and the command *RationalInterpolation*.

In Fig. 2.9 we consider an explicit example where we extrapolate the $\tilde{I}_1(x)$ in (2.8) of the compact boson ($c=1$) for a particular value of the compactification radius corresponding to $\eta = 0.295$ (see also Fig 2.2). For $n \geqslant 2$ the analytic expressions are (2.7) and (2.9) and we take into account $2 \leqslant n \leqslant 6$ only (in Fig. 2.2 we employ also $n=7$). Given these data, we can perform rational interpolations with $p+q+1 \leqslant 5$. The blue curve in Fig. 2.9 is the extrapolation to $n=1$ of the rational interpolation with $(p,q)=(2,2)$. We find it instructive to describe the details for a specific value of x. Let us consider, for instance, a configuration corresponding to $x = \tilde{x} \equiv 0.2101$ (see

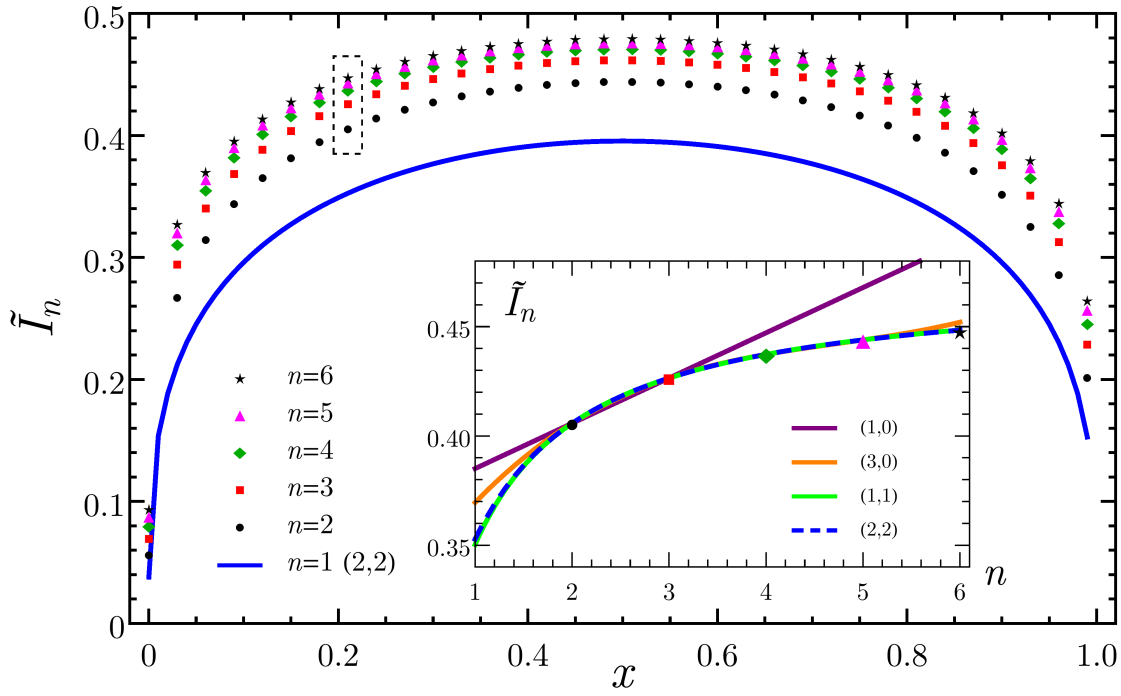

Figure 2.9: The quantity $\tilde{I}_n$ in (2.7) and the corresponding $n \to 1$ limit (2.8) for the compact boson ($c = 1$) with $\eta = 0.295$. The blue line is the extrapolation $n = 1$ of the rational interpolation with $(p, q) = (2, 2)$ obtained through the analytic expressions given by (2.9) and (2.10) with $2 \leqslant n \leqslant 6$, whose values for $\tilde{I}_n$ are shown by points for some values of the four point ratio x. In the inset, considering the configuration having $x = 0.2101$ (highlighted by the dashed rectangle in the main plot), we show $\tilde{I}_n$ as function of n for rational interpolations having different (p, q). The extrapolations having $q > 0$ capture the expected value better than the ones having $q = 0$.

the dashed rectangle in Fig. 2.9). First one has to compute the rational interpolation with $(p, q) = (2, 2)$, then the limit $n \to 1$ must be taken. For these two steps, we find respectively

$$W^n_{(2,2)}(\tilde{x}) = \frac{0.358 - 0.480\, n + 3.689\, n^2}{1 + 1.347\, n + 7.870\, n^2}\,, \qquad \lim_{n\to 1} W^n_{(2,2)}(\tilde{x}) = 0.349\,. \tag{2.42}$$

In the inset of Fig. 2.9 we show how adding more data improves the final extrapolation and how it becomes stable. Focusing again on $x = \tilde{x}$, we can start by taking only $n \in \{2, 3\}$, which allow to perform a rational interpolation with $(p, q) = (1, 0)$ (a line). Since rational interpolations having $p = 0$ often provide wrong predictions, we prefer to avoid them, if possible. The extrapolation to $n = 1$ corresponding to $(p, q) = (1, 0)$ cannot be trusted and therefore we consider four input data $n \in \{2, 3, 4, 5\}$

which allow to consider a rational interpolation with, for instance, $(p,q)=(3,0)$ and also $(p,q)=(1,1)$. These two different rational interpolations do not provide the same extrapolation to $n=1$ and therefore we must take into account more input data. Considering $2 \leqslant n \leqslant 6$ we can choose also $(p,q)=(2,2)$ finding that the corresponding rational interpolation basically coincides with the one with $(p,q)=(1,1)$ (their difference is of order 10^{-3}). Thus, the extrapolation to $n=1$ obtained with $(p,q)=(2,2)$ is quite stable. Repeating this analysis for the whole range of $x \in (0,1)$, one can find the blue curve in Fig. 2.9. As a further check, in Fig. 2.2 we have used $(p,q)=(3,2)$ using more input data, finding that the final extrapolation is basically the same. Plots like the one shown in the inset of Fig. 2.9 are very useful to understand the stability of the extrapolation to $n=1$. Increasing the values of p and q in the rational interpolations leads to more precise extrapolations, as expected. Rational interpolations with $q>0$ provide extrapolations which are closer to the expected value with respect to the ones with $q=0$. When q is strictly positive, q poles occur in the complex plane parameterized by $n \in \mathbb{C}$. Nevertheless, if these poles are far enough from the real interval $(1, n_{\max})$ containing all the n's employed as input data for the interpolation, the extrapolations to $n=1$ are reliable. Increasing q, we have higher probability that one of the poles is close to the region of interpolation, spoiling the extrapolation. Plotting $W^n_{(p,q)}(x)$ as function of n is useful to realize whether this situation occurs (see the inset of Fig. 2.10 for an explicit example).

The issue of evaluating Riemann theta functions which involve large matrices becomes important when we want to compute I_{A_1,A_2,A_3} (see (2.25) and (2.26)) for a compact boson. Indeed, $\mathcal{F}_{3,n}(\boldsymbol{x})$ in (2.28) is given by (2.21) for $N=3$ and therefore the matrix occurring in the Riemann theta function is $2g \times 2g$ with $g=2(n-1)$. Given our computational power, we computed $I^{(n)}_{A_1,A_2,A_3}$ for $n \in \{2,3\}$ for all the needed configurations of intervals, while for $n=4$ we got results only for small intervals. In Fig. 2.10 we show our data and some numerical extrapolations. In the whole range of x_2 we performed only the rational interpolation with $(p,q)=(1,0)$ (blue line) because only two input data are available, while for $x_2 \in (0, 0.22)$, where also $n=4$ is available, we could employ higher values of p and q. When we have more extrapolations, unfortunately they do not overlap, indicating that we cannot trust these curves to give a prediction, even if they are quite close. Another indication that $n=4$ is not enough to get a precise extrapolation comes from the fact that, given the data with $n \in \{3,4\}$ and extrapolating to $n=2$ (orange curve in Fig. 2.10) we did not recover exactly the expected values (purple circles) found with the analytic expressions. In the inset we focus on a configuration of three intervals corresponding to $x_2=0.224$ and show the dependence of $I^{(n)}_{A_1,A_2,A_3}$ on n for various (p,q). While the extrapolations to $n=1$ associated to $(1,0)$ (for this one only $n \in \{2,3\}$ have been used), $(1,1)$ and $(2,0)$ are very close, the one corresponding to $(p,q)=(0,2)$ provides a completely different extrapolation to $n=1$. Considering the two poles of

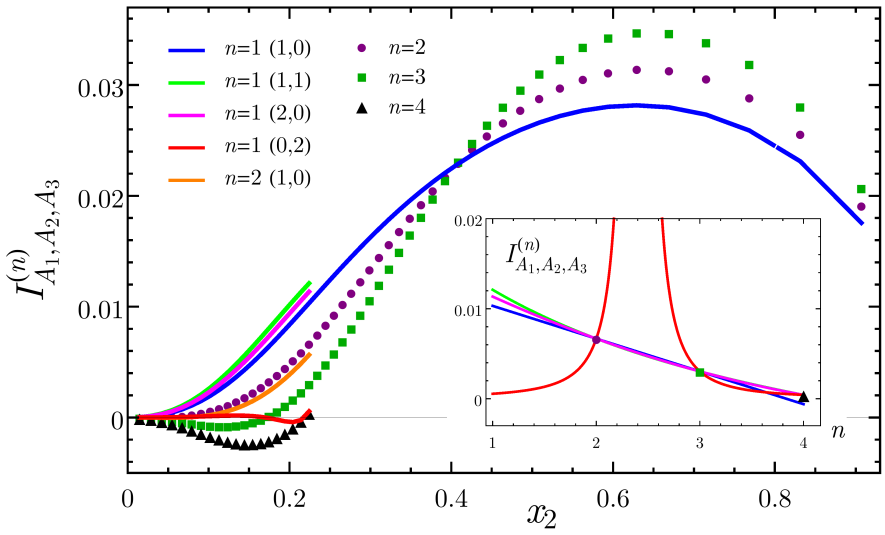

Figure 2.10: Three disjoint intervals: The quantity $I^{(n)}_{A_1,A_2,A_3}$ in (2.26) for the compact boson, computed through (2.28) and (2.21) for $n \geqslant 2$. Our limited computational power in evaluating Riemann theta functions for large matrices prevented us to consider $n = 4$ in the whole range of configurations and this limits also the possible rational interpolations that can be employed. The blu line is the extrapolation found by using only $n \in \{2, 3\}$, which should not be considered as a prediction because more n's are needed to find stable extrapolations. The orange line is a check of the method for $n = 2$: the fact that the expected points are not precisely recovered is due to low number of n's ($n \in \{3, 4\}$) available. In the inset, considering the configuration having $x_2 = 0.224$, we show $I^{(n)}_{A_1,A_2,A_3}$ as function of n for rational interpolations having different (p, q). The rational interpolation with $(p, q) = (0, 2)$ (red line) shows a bad behaviour and the extrapolation to $n = 1$ cannot be trusted; indeed, the red curve in the main plot is different from the other extrapolations.

the interpolating function in the regime of x_2 where also $n = 4$ is available, we find that they are real and at least one of them is inside the domain $n \in (1, 4)$. Thus, the function cannot be considered a good approximation of the true analytic continuation and the extrapolation cannot be trusted. This behaviour does not occur for the case considered in the inset of Fig. 2.9. Thus, it is useful to plot the n dependence of the functions obtained through the rational interpolation method in order to check the occurrence of singularities that could lead to wrong extrapolations.

We find it instructive to discuss some details about the extrapolations of the logarithmic negativity of two disjoint intervals (see §2.4). The simplest case we can deal with is the non compact boson and the replica limit to perform for this model is (2.39). The analytic expression (2.40) contains only hypergeometric functions and

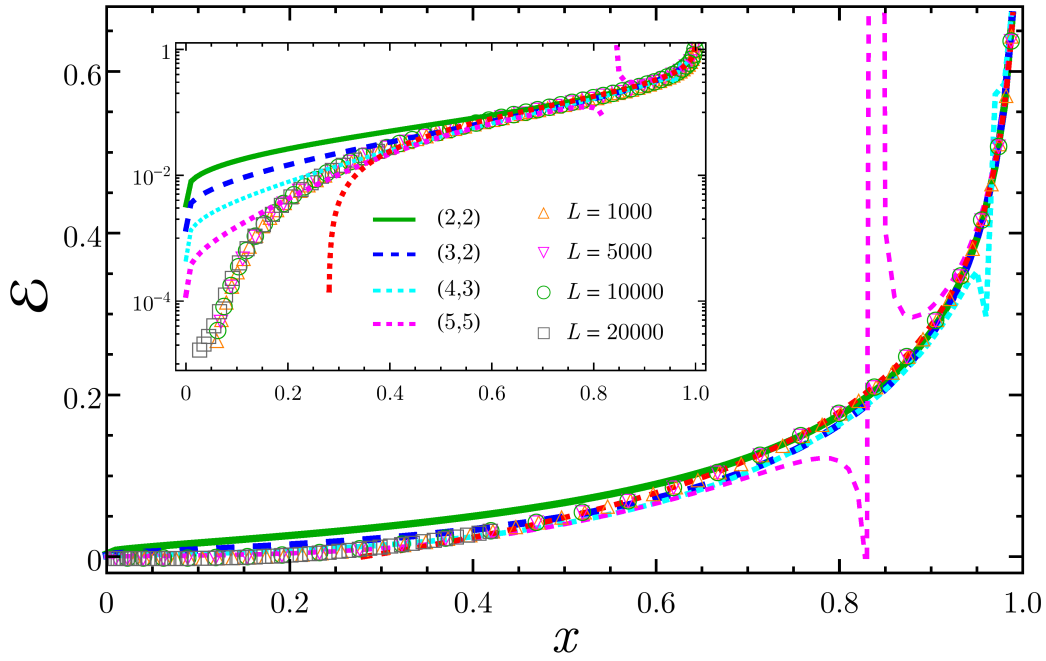

Figure 2.11: Logarithmic negativity of two disjoint intervals for the non compact boson: Extrapolations having low values of p and q. This plot should be compared with Fig. 2.8, where higher values of p and q have been considered. Increasing q improves the extrapolation but in some regimes of x wrong results can be found. The dashed red curve is the analytic continuation for the regime $x \to 1^-$ found in [96], while the points are obtained through a periodic harmonic chain (2.29) with L sites.

therefore it can be evaluated for high values of n. Some extrapolations performed through the rational interpolation method explained above are shown in Figs. 2.8 and 2.11. The first difference between the logarithmic negativity and the mutual information in the extrapolation process is that for the former quantity we need to consider higher values of p and q with respect to the latter one to recover the expected result. Moreover, in the regime of small intervals or large separation (i.e. $x \sim 0$), where the logarithmic negativity falls off to zero faster than any power, it is very difficult to capture its behaviour in a clean way, despite the high values of p and q. In Fig. 2.11 we show some extrapolations characterized by low values of p and q. The most difficult regime to capture is the one with $x \sim 0$. Thus, in Fig. 2.8 we show some extrapolations having higher values of p and q. Comparing the curves in these figures, one observes that with low q's it is difficult to capture the regime of small x, even for very high values of p. Increasing q, the agreement slightly improves for small x, but, as already remarked, it is more probable that the singularities of the rational

interpolation fall close to the domain of the interpolated data. For example, in the case of the dashed magenta curve of Fig.2.11, all the poles of the rational function are real. Varying the parameter x, they move on the real axis and, whenever one of them comes close to the interpolation region $(1, n_{\max})$ and it is not too far from $n = 1$, the extrapolated function to $n = 1$ cannot be trusted as approximation of the true analytic continuation. This leads to fluctuations or singularities in the extrapolation curve as function of x (e.g. see also the dashed cyan curve in Fig. 2.11 and the black and magenta curves in Fig. 2.8).

In order to test the method, in some cases we have performed two further checks. Firstly we have employed as input for the extrapolations the numerical Rényi entropies obtained from the harmonic chain with the largest value of L at our disposal, rather than the analytic ones. The former naturally contains some systematic finite size errors, but the results agree with the ones obtained from the corresponding analytic expressions. Secondly, we added some randomness to the analytic expressions for the Rényi entropies to mimic some statistical errors which may arise when they are computed through approximated techniques such as Monte Carlo. The extrapolations obtained are in agreement with the expected ones up to the same amount of randomness.

Chapter 3

Entanglement negativity in a two dimensional harmonic lattice: Area law and corner contributions

In this chapter it will be reproduced the paper *Entanglement negativity in a two dimensional harmonic lattice: Area law and corner contributions* [164], written in collaboration with Andrea Coser and Erik Tonni.

In the following lines, we are going to study the logarithmic negativity and the moments of the partial transpose in the ground state of a two dimensional massless harmonic square lattice with nearest neighbour interactions for various configurations of adjacent domains. We will see that at leading order for large domains, the logarithmic negativity and the logarithm of the ratio between the generic moment of the partial transpose and the moment of the reduced density matrix at the same order satisfy an area law in terms of the length of the curve shared by the adjacent regions. We will then give numerical evidences that the coefficient of the area law term in these quantities is related to the coefficient of the area law term in the Rényi entropies. Whenever the curve shared by the adjacent domains contains vertices, a subleading logarithmic term occurs in these quantities and the numerical values of the corner function for some pairs of angles are obtained. In the special case of vertices corresponding to explementary angles, we will provide numerical evidence that the corner function of the logarithmic negativity is given by the corner function of the Rényi entropy of order $1/2$.

3.1 Introduction

For some quantum systems on the lattice, the entanglement entropy S_A grows like the area of the boundary of the subsystem A as its size increases [134, 135, 145, 180, 183–185]. This area law behaviour of S_A has been proved for gapped systems on the lattice [49], but for critical systems the situation is more complicated: important exceptions are the critical systems in one spatial dimension, where S_A diverges logarithmically with the length of the interval A [186, 187], and free fermions in higher dimensions [142, 144].

When the continuum limit is described by a quantum field theory, an ultraviolet (UV) cutoff ε must be introduced and S_A is a divergent quantity for $\varepsilon \to 0$. The area law behaviour can occur in the coefficient of the most divergent term, which is non universal and turns out to be proportional to the area of ∂A (i.e. the boundary of A) in these cases. A quantum system in the continuum at criticality is described by a conformal field theory (CFT). Considering a $1+1$ dimensional CFT on a line at zero temperature and an interval A of length ℓ, we have that $S_A = (c/3)\log(\ell/\varepsilon) + \text{const}$, where c is the central charge of the model [15, 45, 46, 136]. Instead, the mutual information (1.53) of two disjoint intervals is UV finite and it depends on the full operator content of the model [62, 63, 70, 71, 74, 94]. Performing the replica limit to get analytic expressions for S_A and I_{A_1,A_2} from the ones for $S_A^{(n)}$ and $I_{A_1,A_2}^{(n)}$ can be a very difficult task (see [123, 171] for a numerical approach).

As we already discussed in §1.7, in $2+1$ dimensional CFTs and for domains A whose boundary is smooth, the expansion of the Rényi entropies reads

$$S_A^{(n)} = \tilde{\alpha}_n \, \frac{P_A}{\varepsilon} + \text{const}\,, \quad \text{as} \quad \varepsilon \to 0\,, \tag{3.1}$$

where P_A is the perimeter of A and the coefficient $\tilde{\alpha}_n$ depends on the model and on the details of the UV regularisation. The replica limit implies that $S_A = \tilde{\alpha}\, P_A/\varepsilon + \text{const}$ as $\varepsilon \to 0$, where $\lim_{n\to 1} \tilde{\alpha}_n = \tilde{\alpha}$. When the two dimensional spatial domain A has a non smooth boundary, $S_A^{(n)}$ contains also a subleading logarithmic term whose coefficient is independent of the regularisation details. Such coefficient is obtained as the sum of the contributions of the vertices of the curve ∂A, where each term is given by a model dependent function (corner function) evaluated on the opening angle in A of the corresponding vertex. Many interesting studies have been done on such corner functions in various lattice models [147, 150, 151, 153, 155, 188–193]. For a CFT in $2+1$ dimensions, it has been recently found that the leading term in the expansion of the corner function as the opening angle θ is close to π provides the constant characterising the two-point function of the stress tensor [154, 157, 158]. Within the context of the AdS/CFT correspondence, the prescription to compute holographically the entanglement entropy in the regime where classical gravity can be employed has been found in [77, 78]. In the case of $\text{AdS}_4/\text{CFT}_3$, such holographic prescription

provides also the expected subleading logarithmic divergence whenever ∂A contains vertices [86, 194–196].

The mutual information (1.53) of disjoint domains with smooth boundaries is a UV finite quantity because the area law terms cancel. When the separation between the regions is large with respect to their sizes, analytic results have been found [87]. In the case of two dimensional adjacent domains A_1 and A_2, both the mutual information and its generalisation involving the Rényi entropies display an area law behaviour in terms of the length of the curve shared by the adjacent regions. In particular, $I^{(n)}_{A_1,A_2} = 2\tilde{\alpha}_n P_{\text{shared}}/\varepsilon + \dots$ and $I_{A_1,A_2} = 2\tilde{\alpha}\, P_{\text{shared}}/\varepsilon + \dots$ as $\varepsilon \to 0$, where $P_{\text{shared}} \equiv \text{length}(\partial A_1 \cap \partial A_2)$.

In this chapter we consider a two dimensional square harmonic lattice with nearest neighbour interactions in its ground state. We focus on the regime of massless oscillators, whose continuum limit is described by the CFT given by the massless scalar field in $2+1$ dimensions. In the thermodynamic limit, we study the logarithmic negativity and the quantity (1.77) for various configurations of adjacent domains in the regime where they become large. At leading order, these quantities follow an area law behaviour in terms of the length of the curve shared by the adjacent regions. This observation for the logarithmic negativity has been already done for this model in [130], where the configuration given by two halves of a square has been considered. We notice that the coefficient of the area law term is related to the coefficient of the area law term in the Rényi entropies. We study also the subleading logarithmic term, which occurs whenever the curve shared by the adjacent regions contains vertices. Such term is very interesting because it is independent of the regularisation details.

The layout of this chapter is as follows. In §3.2 we review the method to compute S_A, $S^{(n)}_A$, $\mathcal{E}$ and $\mathcal{E}_n$ for this bosonic lattice. In §3.3 we investigate the area law behaviour in the leading term of $\mathcal{E}$ and $\mathcal{E}_n$ for various configurations of large adjacent domains in the infinitely extended lattice. In §3.4 we study the subleading logarithmic term of $\mathcal{E}$ due to the occurrence of vertices in the curve shared by the adjacent domains and in §3.5 we draw some conclusions.

3.2 Harmonic lattice

In this section we introduce the lattice model considered throughout this chapter, its correlators in the thermodynamic limit and their role in computing the entanglement entropies, the moments of the partial transpose and the logarithmic negativity.

3.2.1 Hamiltonian and correlators

We consider the two dimensional square lattice made by harmonic oscillators coupled through the nearest neighbour spring-like interaction. Denoting by L_x and L_y the

number of sites (oscillators) along the two orthogonal directions, such lattice contains $N = L_x L_y$ oscillators. The Hamiltonian of the model reads

$$H = \sum_{\substack{1\leqslant i\leqslant L_x \\ 1\leqslant j\leqslant L_y}} \left\{ \frac{p_{i,j}^2}{2M} + \frac{M\omega^2}{2}\, q_{i,j}^2 + \frac{K}{2}\Big[\big(q_{i+1,j} - q_{i,j}\big)^2 + \big(q_{i,j+1} - q_{i,j}\big)^2 \Big] \right\}, \tag{3.2}$$

where the pair of integers (i, j) identifies a specific lattice site. The canonical variables $q_{i,j}$ and $p_{i,j}$ satisfy the canonical commutation relation $[q_{i,j}, q_{r,s}] = [p_{i,j}, p_{r,s}] = 0$ and $[q_{i,j}, p_{r,s}] = \mathrm{i}\,\delta_{i,r}\delta_{j,s}$. We assume periodic boundary conditions along both the spatial directions, namely $q_{L_x+k,j} = q_{k,j}$, $p_{L_x+k,j} = p_{k,j}$, $q_{j,L_y+k} = q_{j,k}$ and $p_{j,L_y+k} = p_{j,k}$ for a generic integer k.

The model described by (3.2) contains three parameters ω, M and K, but not all of them are independent. Indeed, by performing the canonical rescaling $(q_{i,j}, p_{i,j}) \to (\sqrt[4]{MK}\, q_{i,j},\, p_{i,j}/\sqrt[4]{MK})$ and introducing $a = \sqrt{M/K}$, the Hamiltonian (3.2) becomes

$$H = \sum_{\substack{1\leqslant i\leqslant L_x \\ 1\leqslant j\leqslant L_y}} \left\{ \frac{p_{i,j}^2}{2a} + \frac{a\omega^2}{2}\, q_{i,j}^2 + \frac{1}{2a}\Big[\big(q_{i+1,j} - q_{i,j}\big)^2 + \big(q_{i,j+1} - q_{i,j}\big)^2 \Big] \right\}. \tag{3.3}$$

From this expression, one can easily observe that (3.2) gives the Hamiltonian of a free scalar field with mass ω in two spatial dimensions discretised on a square lattice with lattice spacing a. The continuum limit corresponds to take simultaneously the limits $L_x \to \infty$, $L_y \to \infty$ and $a \to 0$, while $L_x a$ and $L_y a$ are kept fixed. In our lattice computations, without loss of generality, we set $K = M = 1$. The Hamiltonian (3.2) can be diagonalised in a standard way, finding the following dispersion relation

$$\omega_{\boldsymbol{k}} \equiv \sqrt{\omega^2 + 4\Big[\sin^2(\pi k_x/L_x) + \sin^2(\pi k_y/L_y) \Big]} \;\geqslant\; \omega\,, \tag{3.4}$$

where $\boldsymbol{k} = (k_x, k_y)$ is a pair of integers such that $0 \leqslant k_x < L_x$ and $0 \leqslant k_y < L_y$. Because of the translation invariance of the model, the zero mode with $\boldsymbol{k} = (0, 0)$ occurs, for which the equality holds in (3.4).

In our analysis we need the following vacuum correlators

$$\langle 0|q_{i,j}q_{r,s}|0\rangle \;=\; \frac{1}{2\,L_x L_y} \sum_{\substack{0\leqslant k_x<L_x \\ 0\leqslant k_y<L_y}} \frac{1}{\omega_{\boldsymbol{k}}}\, \cos[2\pi k_x(i-r)/L_x]\, \cos[2\pi k_y(j-s)/L_y]\,, \tag{3.5}$$

$$\langle 0|p_{i,j}p_{r,s}|0\rangle \;=\; \frac{1}{2\,L_x L_y} \sum_{\substack{0\leqslant k_x<L_x \\ 0\leqslant k_y<L_y}} \omega_{\boldsymbol{k}}\, \cos[2\pi k_x(i-r)/L_x]\, \cos[2\pi k_y(j-s)/L_y]\,, \tag{3.6}$$

which are the matrix elements of the correlation matrices $\mathbb{Q}$ and $\mathbb{P}$ respectively (where (i, j) and (r, s) are the raw and column indices respectively). These matrices satisfy

$\mathbb{Q} \cdot \mathbb{P} = \mathbb{I}/4$, being $\mathbb{I}$ is the identity matrix. We remark that the term in (3.5) corresponding to the zero mode reads $1/(2L_xL_y\omega)$, which is divergent for $\omega \to 0$. This implies that we cannot take $\omega = 0$ in a finite lattice.

Since from our computations on the lattice we would like to extract information about the model in the continuum limit, we need to consider the regime where $L_x, L_y \gg \ell \gg 1$, being ℓ the linear size of the subsystem. Thus, it is convenient to consider the thermodynamic limit, where $L_x \to \infty$ and $L_y \to \infty$, while the lattice spacing a is kept finite. In order to perform the thermodynamic limit of the correlators (3.5) and (3.6), we define $q_r = 2\pi k_r/L_r$ for $r \in \{x, y\}$. In the thermodynamic limit q_r becomes a continuous variable $q_r \in [0, 2\pi)$ and the sum in (3.5) and (3.6) is replaced by an integration according to $\frac{1}{L_r}\sum_{k_r} \to \int_0^{2\pi} \frac{dq_r}{2\pi}$. Thus, the correlators (3.5) and (3.6) in the thermodynamic limit become respectively

$$\langle 0|q_{i,j}q_{r,s}|0\rangle \;=\; \frac{1}{8\pi^2}\int_0^{2\pi} \frac{1}{\omega_{\boldsymbol{q}}}\,\cos[q_x(i-r)]\,\cos[q_y(j-s)]\,dq_x dq_y\,, \tag{3.7}$$

$$\langle 0|p_{i,j}p_{r,s}|0\rangle \;=\; \frac{1}{8\pi^2}\int_0^{2\pi} \omega_{\boldsymbol{q}}\,\cos[q_x(i-r)]\,\cos[q_y(j-s)]\,dq_x dq_y\,, \tag{3.8}$$

where $\omega_{\boldsymbol{q}} = \sqrt{\omega^2 + 4[\sin^2(q_x/2) + \sin^2(q_y/2)]}$, with $\boldsymbol{q} = (q_x, q_y)$. When $\omega = 0$ the integral in (3.7) is convergent and therefore, in principle, the massless regime can be considered without any approximation. Nevertheless, in order to avoid divergent integrands, in our numerical calculations we have set $\omega \leqslant 10^{-6}$, checking in some cases that smaller values of ω do not lead to significant changes in the final result.

3.2.2 Entanglement entropies

Following [176, 178, 179, 181], we can compute the Rényi entropies $S_A^{(n)}$ for this model by considering the matrices $\mathbb{Q}_A$ and $\mathbb{P}_A$, which are obtained by restricting $\mathbb{Q}$ and $\mathbb{P}$ respectively to the subsystem A. Their size is $N_A \times N_A$, being N_A the number of lattice points inside the region A.

The matrix product $\mathbb{Q}_A \cdot \mathbb{P}_A$ has positive eigenvalues $\{\mu_1^2, \ldots, \mu_{N_A}^2\}$ with $\mu_i^2 \geqslant 1/4$ and the moments of the reduced density matrix are given by

$$\operatorname{Tr}\rho_A^n \;=\; \prod_{j=1}^{N_A}\left[\left(\mu_j + \frac{1}{2}\right)^n - \left(\mu_j - \frac{1}{2}\right)^n\right]^{-1}. \tag{3.9}$$

From this expression it is straightforward to get the Rényi entropies

$$S_A^{(n)} = \frac{1}{1-n}\,\log \operatorname{Tr}\rho_A^n \;=\; \frac{1}{n-1}\sum_{j=1}^{N_A}\log\left[\left(\mu_j + \frac{1}{2}\right)^n - \left(\mu_j - \frac{1}{2}\right)^n\right], \tag{3.10}$$

while the entanglement entropy is given by

$$S_A = \sum_{j=1}^{N_A} \left[\left(\mu_j + \frac{1}{2}\right) \log\left(\mu_j + \frac{1}{2}\right) - \left(\mu_j - \frac{1}{2}\right) \log\left(\mu_j - \frac{1}{2}\right) \right] . \tag{3.11}$$

By employing these formulas for disjoint domains on the lattice, one gets $I^{(n)}_{A_1,A_2}$ and the mutual information I_{A_1,A_2}.

3.2.3 Moments of the partial transpose and logarithmic negativity

In [33, 177] it was shown that the partial transposition with respect to A_2 for a bosonic state corresponds to the time reversal applied only to the degrees of freedom in A_2, while the remaining ones are untouched. In particular, in A_2 the positions are left invariant $q_{i,j} \to q_{i,j}$ everywhere, while the momenta are reversed $p_{i,j} \to -p_{i,j}$ if $(i,j) \in A_2$. Given a bosonic Gaussian state, like the ground state of the harmonic chain we are considering, the resulting operator after such transformation will be Gaussian as well. It is worth remarking that this is not true for fermionic systems. For instance, for free fermions the partial transpose of the ground state density matrix can be written as a sum of two Gaussian operators [103].

The above observations are implemented on our lattice model by introducing the following matrix

$$\mathbb{P}_A^{T_2} = \mathbb{R}_{A_2} \cdot \mathbb{P}_A \cdot \mathbb{R}_{A_2} \,, \tag{3.12}$$

where $\mathbb{R}_{A_2}$ is the $N_A \times N_A$ diagonal matrix having -1 in correspondence of the sites belonging to A_2 and $+1$ otherwise. Since $\mathbb{R}_{A_1} = -\mathbb{R}_{A_2}$, it is easy to observe that $\mathbb{P}_A^{T_1} = \mathbb{P}_A^{T_2}$, as expected. The matrix $\mathbb{Q}_A \cdot \mathbb{P}_A^{T_2}$ has also positive eigenvalues $\{\nu_1^2, \ldots, \nu_{N_A}^2\}$, but if the state is entangled some of them can be smaller than $1/4$. From the eigenvalues ν_j one gets the moments of the partial transpose of the reduced density matrix as in (3.9) for the moments of the reduced density matrix, namely

$$\mathrm{Tr}\left(\rho_A^{T_2}\right)^n = \prod_{j=1}^{N_A} \left[\left(\nu_j + \frac{1}{2}\right)^n - \left(\nu_j - \frac{1}{2}\right)^n \right]^{-1} . \tag{3.13}$$

The trace norm of $\rho_A^{T_2}$ reads

$$\left\|\rho_A^{T_2}\right\| = \prod_{j=1}^{N_A} \left[\left|\nu_j + \frac{1}{2}\right| - \left|\nu_j - \frac{1}{2}\right| \right]^{-1} = \prod_{j=1}^{N_A} \max\left(1, \frac{1}{2\nu_j}\right) , \tag{3.14}$$

which leads straightforwardly to the logarithmic negativity

$$\mathcal{E} = \sum_{j=1}^{N_A} \log\left[\max\left(1, (2\nu_j)^{-1}\right)\right] . \tag{3.15}$$

In the remaining part of the chapter we discuss the numerical results obtained by employing the above lattice formulas.

3.3 Area law

In this section we consider various configurations of adjacent domains for the harmonic lattice in the thermodynamic limit described in §3.2. For large domains, we show that at leading order the logarithmic negativity and $\mathcal{E}_n$ satisfy an area law in terms of the length of the curve shared by the adjacent domains. We observe that the coefficient of such term in these quantities is related to the coefficient of the area law term in the Rényi entropies.

3.3.1 Logarithmic negativity

We begin our analysis by considering the logarithmic negativity of two equal adjacent rectangles A_1 and A_2 which share an edge along the vertical y axis, as shown in the inset of the left panel in Fig. 3.1, where the adjacent domains are highlighted by blue dots and red circles. These rectangles have the natural orientation induced by the underlying lattice, namely their edges are parallel to the vectors generating the square lattice. Denoting by ℓ_x and ℓ_y the lengths of the edges along the x and y directions respectively, the numerical data for $\mathcal{E}$ of this configuration of adjacent domains are plotted in Fig. 3.1.

In the left panel we show the ratio $\mathcal{E}/\ell_y$ as function of ℓ_x when ℓ_y is kept fixed. For any given ℓ_y, such ratio reaches a constant value when ℓ_x is sufficiently large. This confirms the intuition that the main contribution to a quantity characterising the entanglement between two adjacent regions A_1 and A_2 should come from the degrees of freedom localized along their shared boundary, namely the curve $\partial A_1 \cap \partial A_2$. In the right panel of Fig. 3.1, the logarithmic negativity of the same configuration is plotted as function of ℓ_y for fixed values of ℓ_x. If ℓ_x is sufficiently large, a neat linear growth can be observed. The fact that the asymptotic value of $\mathcal{E}/\ell_y$ depends on ℓ_y in the left panel of Fig. 3.1 is mainly due to the subleading corner contributions, which will be largely discussed in §3.4.

These results tell us that, given two equal and large enough adjacent regions A_1 and A_2, at leading order the logarithmic negativity $\mathcal{E}$ between them increases like the length of the curve $\partial A_1 \cap \partial A_2$ shared by their boundaries as their size increases. Such length will be denoted by $P_{\text{shared}} \equiv \text{length}(\partial A_1 \cap \partial A_2)$ throughout this chapter. Thus, the logarithmic negativity between large adjacent domains satisfies an area law in terms of the region shared by their boundaries. This observation has been recently done for this model also by Eisler and Zimborás [130], who have considered the logarithmic negativity between the two halves of a square as the length of its edge increases.

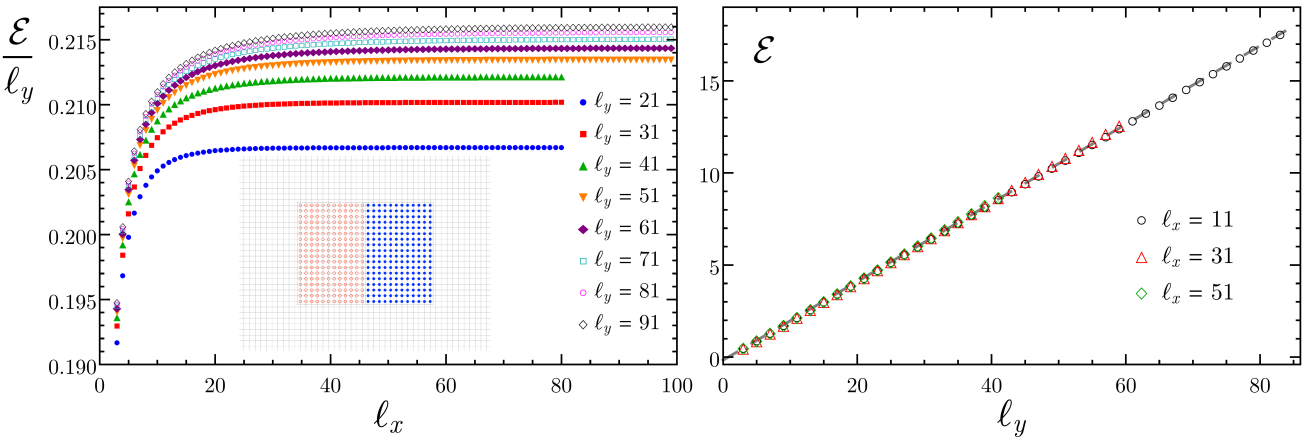

Figure 3.1: Area law behaviour for the logarithmic negativity $\mathcal{E}$ between two equal rectangles, whose edges have lengths ℓ_x and ℓ_y, which are adjacent along the vertical edge (inset of the left panel). Left: For fixed values of ℓ_y, the ratio $\mathcal{E}/\ell_y$ reaches a constant value as ℓ_x increases. Right: For fixed and large enough values of ℓ_x, the logarithmic negativity grows linearly as ℓ_y increases (the dashed line is obtained by fitting all the data corresponding to $\ell_x = 11$).

In order to improve our analysis of the area law behaviour for the logarithmic negativity between adjacent regions A_1 and A_2, let us consider the six configurations of adjacent domains on the lattice shown in Fig. 3.2, where the sites belonging to A_1 and A_2 are highlighted by blue dots and red circles. In these examples the curve $\partial A_1 \cap \partial A_2$ is not given by a simple line segment. The domains identified by the red circles in Fig. 3.2 are convex, while the ones corresponding to the blue dots are not.

It is well known that the curve separating adjacent domains on the lattice is not unique. For these configurations we have chosen the dashed lines, which are the lines whose length has been used to get the perimeter. The three configurations in the top panels of Fig. 3.2 are natural to define on the square lattice because their edges are parallel to the orthogonal vectors generating the lattice. Instead, the three configurations in the bottom panels of Fig. 3.2 are made by adjacent domains where the line $\partial A_1 \cap \partial A_2$ either is curved or it contains a line segment which is oblique with respect to the vectors generating the lattice. Notice that a disk of given radius on the lattice could include a different number of sites depending on whether the centre of the disk is located on a lattice site or within a plaquette. Such ambiguity does not affect the leading order behaviour of the quantities that we are considering, but it could be relevant for subleading terms [189, 197].

Also for the logarithmic negativity of the adjacent domains shown in Fig. 3.2 we have observed the same qualitative behaviour described in the left panel of Fig. 3.1

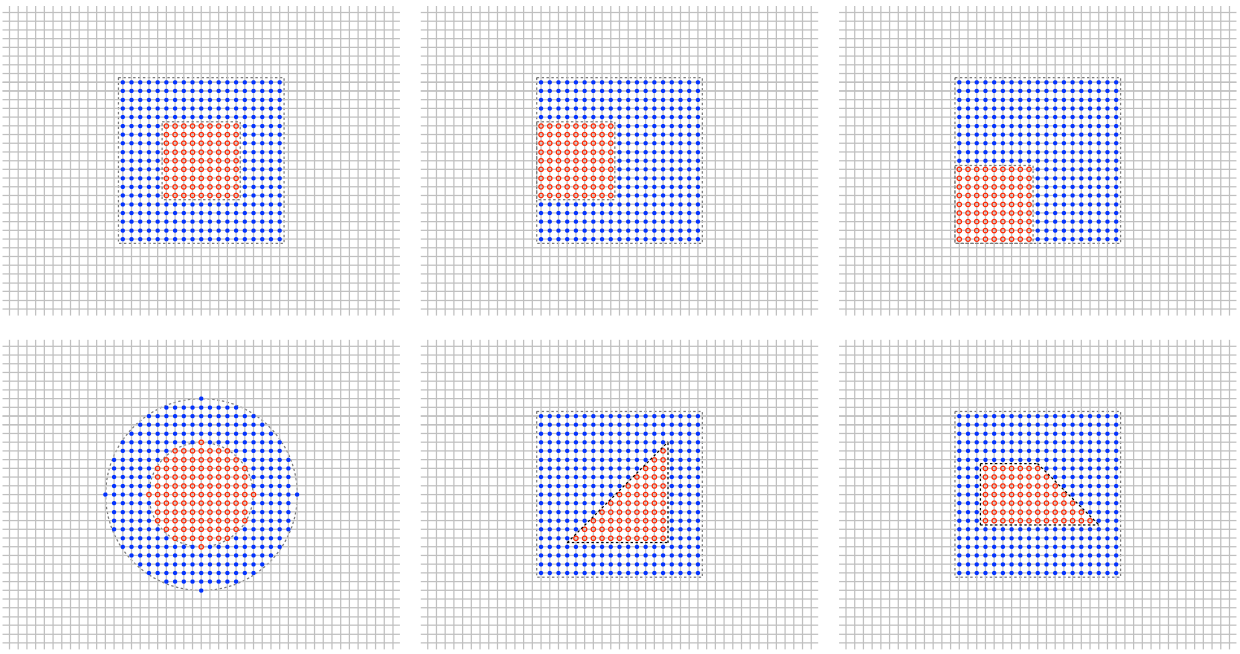

Figure 3.2: Configurations of adjacent domains on the lattice, identified by red circles and blue dots, which have been employed to study the area law behaviour (see §3.3 and Figs. 3.3 and 3.4) and the corner contributions for explementary angles (see §3.4 and Fig. 3.5).

for the equal adjacent rectangles: by keeping fixed the region corresponding to the red circles while the sizes of the region characterised by the blue dots increase, $\mathcal{E}$ saturates to a constant value.

In Fig. 3.3 we show some quantitative results for the logarithmic negativity of the configurations in Fig. 3.2. In particular, let us consider the configuration in the top left panel, which is characterised by the lengths $\ell_{\text{in}} < \ell_{\text{out}}$ of the edges of the internal square and of the whole subregion $A_1 \cup A_2$ respectively. In the left panel of Fig. 3.3 we show $\mathcal{E}/\ell_{\text{out}}$ as function of the ratio $\ell_{\text{in}}/\ell_{\text{out}} < 1$ when ℓ_{out} is kept fixed and the internal square increases. For large enough ℓ_{out}, the area law behaviour in terms of ℓ_{in} is observed. It is worth remarking that $\mathcal{E} \to 0$ when $\ell_{\text{in}}/\ell_{\text{out}} \to 1$. This is expected because in this limit the internal convex domain becomes the whole A. For any fixed and large enough value of ℓ_{out} there is a critical size of the internal square after which the logarithmic negativity deviates from the linear growth predicted by the area law. The numerical data tell us that such critical value of ℓ_{in} increases by increasing ℓ_{out}. This suggests that in the continuum limit, where both ℓ_{in} and ℓ_{out} diverge but their ratio is finite, the linear behaviour occurs for any ratio $\ell_{\text{in}}/\ell_{\text{out}} < 1$. From the plot in the left panel of Fig. 3.3 one can also notice that the ratio $\ell_{\text{in}}/\ell_{\text{out}} \simeq 1/3$ is a

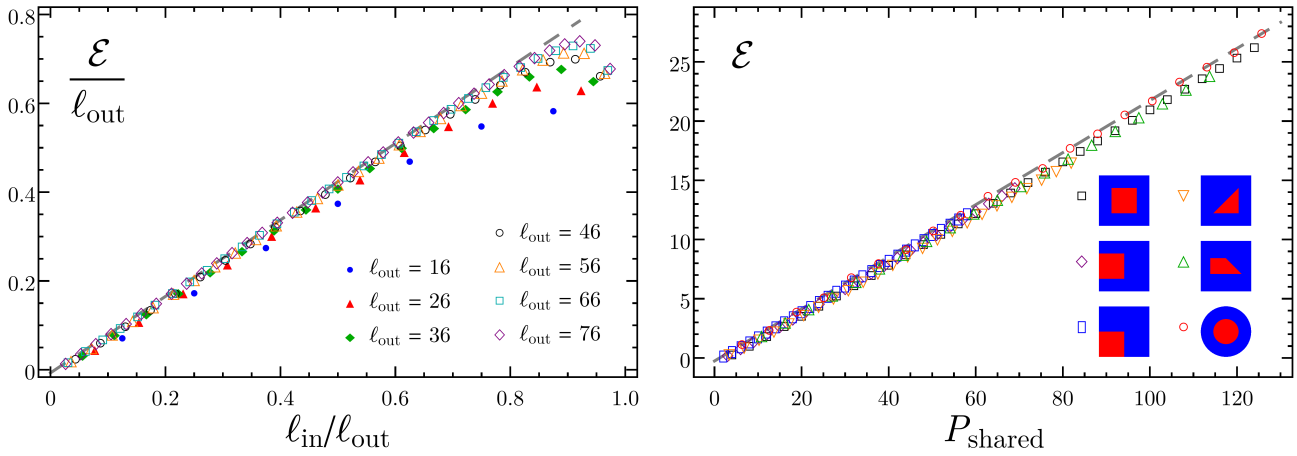

Figure 3.3: Left: Logarithmic negativity for the configuration in the top left panel of Fig. 3.2, where $\ell_{\rm in}$ and $\ell_{\rm out}$ are the sizes of the edges of the red square and of the square $A_1 \cup A_2$ respectively. The dashed line is obtained by fitting the data corresponding to $\ell_{\rm out} = 76$ up to $\ell_{\rm in}/\ell_{\rm out} \simeq 0.7$. Right: Logarithmic negativity of adjacent domains for the configurations shown in Fig. 3.2, which involve different shapes for the curve $\partial A_1 \cap \partial A_2$. The sizes of the domains increase while their ratios are kept fixed. The data correspond to configurations where the linear size of the convex domains (highlighted by red circles) is 1/3 of the size of the corresponding $A_1 \cup A_2$. The dashed line has been found by fitting the data obtained for the configuration in the bottom left panel of Fig. 3.2.

good regime to explore the area law behaviour even for relatively small domains. Given the latter observation, we have considered the logarithmic negativity of all the configurations in Fig. 3.2 with a ratio of 1/3 between the size of the internal convex domain and the one of the whole subsystem A (for the triangle we refer to its shortest edge and for the trapezoid to its height). By increasing the sizes of both the domains while their ratio is kept fixed to 1/3, we find the results collected in the right panel of Fig. 3.3, which nicely confirm the area law behaviour in terms of $P_{\rm shared}$ observed above. Notice that the different configurations in the right panel of Fig. 3.3 provide linear growths with almost the same slope. Moreover, the data corresponding to the configuration in the bottom left panel of Fig. 3.2 do not provide a neat straight line, as expected whenever domains with a curved boundary on a square lattice are involved.

Summarising the numerical results presented above, we can conclude that at the leading order the logarithmic negativity of two large adjacent domains A_1 and A_2 on a lattice of massless harmonic oscillators with nearest neighbour spring-like interactions in the ground state satisfies an area law in terms of the length $P_{\rm shared}$ of the curve

shared by the adjacent regions, namely

$$\mathcal{E} \,=\, a\, P_{\text{shared}} + \dots \,, \tag{3.16}$$

where the dots indicate subleading terms for large values of P_{shared}. The area law (3.16) is consistent with the fact that $\mathcal{E}$ measures the bipartite entanglement between A_1 and A_2 for the mixed state characterised by the reduced density matrix $\rho_{A_1\cup A_2}$. The coefficient a in (3.16) is non universal, i.e. it depends on the ultraviolet details.

Given the two adjacent regions A_1 and A_2 considered above, another very interesting quantity to study is their mutual information I_{A_1,A_2}, which has been defined in (**??**). Since the area law of the entanglement entropy for large domains tells us that $S_A = \tilde{a}\, P_A + \dots$, it is straightforward to find that I_{A_1,A_2} of adjacent domains satisfies an area law in terms of P_{shared}. In particular, we have that

$$I_{A_1,A_2} \,=\, 2\tilde{a}\, P_{\text{shared}} + \dots \,, \tag{3.17}$$

where, as above, the dots stand for subleading terms.

3.3.2 Moments of the partial transpose

The moments $\text{Tr}(\rho_A^{T_2})^n$ of the partial transpose for integer values of n are interesting quantities to study because they provide the logarithmic negativity through the replica limit (1.79) [95, 96].

Given the configurations of adjacent domains described in §3.3.1, instead of considering the n-th moment of the partial transpose, we find it more interesting the ratio $\mathcal{E}_n$ defined in (1.77), which also provides the logarithmic negativity through the replica limit (1.81) because of the normalisation condition $\text{Tr}\,\rho_A = 1$. In our model, the main reason to consider $\mathcal{E}_n$ instead of $\log \text{Tr}(\rho^{T_2})^n$ occurring in (1.79) is that, by repeating the analysis described in §3.3.1, we find that, at leading order for large adjacent domains, $\mathcal{E}_n$ follows an area law in terms of the length of the curve shared by the adjacent domains, i.e.

$$\mathcal{E}_n \,=\, a_n\, P_{\text{shared}} + \dots \,, \tag{3.18}$$

where the non universal coefficient a_n depends on the integer n and the dots denote subleading terms. We recall that the Rényi entropies of our model satisfy the area law $S_A^{(n)} = \tilde{a}_n\, P_A + \dots$, where the coefficient $\tilde{a}_n$ is non universal as well and $\lim_{n\to 1} \tilde{a}_n = \tilde{a}$.

From (3.18) and the area law of the Rényi entropies it is straightforward to find the leading term of the logarithm of the moments of the partial transpose, which is given by

$$\log \text{Tr}\left(\rho_A^{T_2}\right)^n = \, a_n\, P_{\text{shared}} + (1-n)\tilde{a}_n\, P_A + \dots \,. \tag{3.19}$$

Thus, the quantities $\log \text{Tr}(\rho_A^{T_2})^n$ contain an area law contribution also from the boundary of $A = A_1 \cup A_2$. Since $\lim_{n_e\to 1}(n_e - 1)\tilde{a}_{n_e} = 0$, such term cancels in

the replica limit (1.79). A similar cancellation occurs also for adjacent intervals in $1+1$ dimensional CFTs. Indeed, considering the divergent terms for $\varepsilon \to 0$, in $\mathcal{E}_n$ only the ones giving a non trivial contribution after the replica limit survive, while $\log \mathrm{Tr}(\rho^{T_2})^n$ contains also other terms [96], which vanish in the replica limit (1.79). The quantity $\mathcal{E}_n$ for adjacent intervals in $1+1$ dimensional CFTs has been studied in [102, 107] and for free fermions on a two dimensional lattice in [130].

In the left panel of Fig. 3.4 we show $\tilde{a}_n$ as function of n for disks and squares on the infinite lattice. The centres of the disks have been chosen either on a lattice site (like in the bottom left panel of Fig. 3.2) or in the central point of a plaquette. As for the squares, we have considered both the ones whose edges are parallel to the vectors generating the lattice and the ones obtained by rotating of $\pi/4$ the previous ones (denoted as rhombi in the plot). In this plot we have $150 \leqslant P_{\text{shared}} \leqslant 200$, depending on the configuration. A slight dependence of $\tilde{a}_n$ on the shape can be observed from our data points. The asymptotic $\tilde{a}_n \sim 1/n^2$ as $n \to 0$ [198, 199] is consistent with our numerical results. For the Ising model a numerical analysis for $\tilde{a}_n$ as $n \to 0$ has been done in [65]. The numerical data in the left panel of Fig. 3.4 have been found by employing a fitting function which includes also a logarithmic term, as it will be discussed in detail in §3.4, but such term does not change the coefficient of the leading area law term in a significant way.

It is worth considering the quantity $I^{(n)}_{A_1,A_2} = S^{(n)}_{A_1} + S^{(n)}_{A_2} - S^{(n)}_{A_1 \cup A_2}$ for the configurations of adjacent domains described in §3.3.1. Given the area law behaviour of $S^{(n)}_A$, it is easy to observe that $I^{(n)}_{A_1,A_2}$ displays an area law behaviour in terms of P_{shared}, namely

$$I^{(n)}_{A_1,A_2} \,=\, 2\tilde{a}_n \, P_{\text{shared}} + \dots \,, \tag{3.20}$$

Once the configuration of adjacent domains A_1 and A_2 has been chosen, we find it interesting to compare the non universal coefficients a_n and $\tilde{a}_n$ occurring in the area law terms of (3.18) and (3.20) respectively.

It is reasonable to expect that the area law term for $\mathcal{E}_n$ comes from effects localised in the neighbourhood of the curve $\partial A_1 \cap \partial A_2$. Thus, considering e.g. the configurations in Fig. 3.2 where the domain identified by the red circles is entirely surrounded by the one characterised by the blue dots (i.e. the configurations in the top left, bottom middle and bottom right panels), such term should be independent of the size of the domain identified by the blue dots. In the limit where this domain becomes the whole region complementary to the one identified by the red circles, one gets the bipartition of the ground state. These considerations suggest us that a_n in (3.18) is the same one occurring for a bipartition of the ground state, when the identity (1.80) can be applied. This implies that the following relation should hold

$$a_n = \begin{cases} \big(1 - n_o\big)\, \tilde{a}_{n_o} & \text{odd } n = n_o \,, \\ 2\big(1 - n_e/2\big)\, \tilde{a}_{n_e/2} & \text{even } n = n_e \,. \end{cases} \tag{3.21}$$

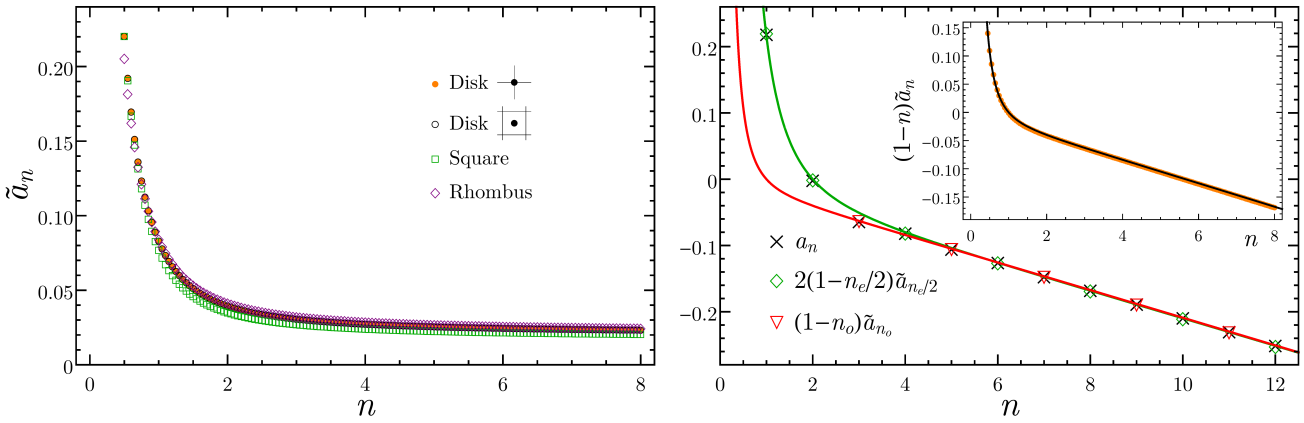

Figure 3.4: Left: The coefficient of the area law term in the Rényi entropies $S_A^{(n)}$ as function of n for domains with different shapes. centre The centres of the disks have been chosen both on the lattice site and in the centre of a plaquette. Here the edges of the square configuration are parallel to the vectors generating the lattice, while the rhombus configuration corresponds to the previous square configuration rotated by $\pi/4$ with respect to its centre. Right: Numerical check of (3.21) and (3.22) for the configuration in the bottom left panel of Fig. 3.2 with $R_{\rm in}/R_{\rm out} = 1/3$. Inset: The coefficient $(1-n)\tilde{a}_n$ as function of n for disks (the data are taken from the left panel with the same colour code). The black curve corresponds to the best fit of the numerical data through the function $f(n) = c_{-2}/n^2 + c_{-1}/n + c_0 + c_1 n$, constrained by the condition $f(1) = 0$. In the main plot the red curve is $f(n)$ obtained in the inset and the green one is $2f(n/2)$.

Notice that $a_2 = 0$, as expected. By employing the relation (3.21) and the replica limit (1.81), it is straightforward to find that the coefficient of the area law term in the logarithmic negativity in (3.16) is equal to the coefficient of the area law term in the Rényi entropy of order 1/2, namely

$$a \;=\; \tilde{a}_{1/2}\,. \tag{3.22}$$

In the right panel of Fig. 3.4 we show a numerical check of the relations (3.21) and (3.22) for the configuration in the bottom left panel of Fig. 3.2. In particular, the coincidence of the data points corresponding to $n = 1/2$ provides a check of (3.22). The solid curve in the inset is obtained by fitting the data with the function $f(n) = c_{-2}/n^2 + c_{-1}/n + c_0 + c_1 n$, where the parameters are constrained by the requirement that $f(1) = 0$. Thus, such fit has three independent parameters. As for the solid curves in the main plot, the red one is $f(n)$, namely the black curve found in the inset, while the green one is $2f(n/2)$.

This analysis has been performed also for other configurations as further checks of (3.21) and (3.22), finding the same qualitative behaviours.

3.4 Logarithmic term from the corner contributions

In this section we consider the subleading logarithmic term in $\mathcal{E}$ and $\mathcal{E}_n$ for adjacent domains, which occurs whenever the shared curve $\partial A_1 \cap \partial A_2$ contains some vertices, where its endpoints are included among them. For vertices corresponding to explementary angles, we provide some numerical evidence that the corner function of $\mathcal{E}$ is given by the corner function of the Rényi entropy of order 1/2.

3.4.1 Entanglement entropies

Let us consider the entanglement entropy S_A of a connected domain A whose boundary contains some vertices (see Figs. 3.2, 3.6 and 3.8 for examples). For large size of A, the leading term gives the area law behaviour. The occurrence of vertices in ∂A provides a subleading logarithmic term which is characterised by a corner function $\tilde{b}(\theta)$ as follows [147, 188, 189]

$$S_A = \tilde{a}\, P_A - \left(\sum_{\substack{\text{vertices} \\ \text{of } \partial A}} \tilde{b}(\theta_i) \right) \log P_A + \dots \qquad 0 < \theta_i \leqslant \pi \,, \tag{3.23}$$

where θ_i is the opening angle in A corresponding to the i-th vertex of ∂A and the dots denote subleading terms.

Since the logarithmic term is due to the corners, we have that $\tilde{b}(\pi) = 0$. From the general property that $S_A = S_B$ for pure states and a bipartite Hilbert space $\mathcal{H} = \mathcal{H}_A \otimes \mathcal{H}_B$, we have that $\tilde{b}(\theta) = \tilde{b}(2\pi - \theta)$, which tells us that $\tilde{b}(\theta)$ is defined for $0 < \theta \leqslant \pi$. The model dependent corner function $\tilde{b}(\theta)$ is universal, i.e. independent of the ultraviolet details of the regularisation. In the continuum limit, which is described by a $2+1$ dimensional CFT, the corner function $\tilde{b}(\theta)$ contains important information about the model. For instance, recently it has been found that the constant σ entering in the asymptotic behaviour $\tilde{b}(\theta) = \sigma(\pi - \theta)^2 + \dots$ as $\theta \to \pi$ at the leading order is related to the constant characterising the correlator $\langle T_{\mu\nu}(x) T_{\alpha\beta}(y) \rangle$ of the underlying CFT [154, 157]. The corner function $\tilde{b}(\theta)$ for the massless scalar has been studied by Casini and Huerta [147]. In the context of holography, by employing the prescription of [77, 78] for S_A, the corner function $\tilde{b}(\theta)$ has been studied e.g. in [86, 194–196].

We find it worth considering the mutual information (**??**) of two adjacent domains A_1 and A_2 when their boundaries contain some vertices. For the sake of simplicity, we focus on configurations such that either two or three curves meet at every vertex. Explicit examples are shown in Figs. 3.2, 3.6 and 3.8, where the adjacent domains are

identified by blue dots and red circles. In the scaling limit, when their sizes increase while the ratios among them are kept fixed, from (3.23) one finds that

$$I_{A_1,A_2} \,=\, 2\tilde{a}\, P_{\text{shared}} - \Bigg(\sum_{\substack{\text{vertices of} \\ \partial A_1 \cap \partial A_2}} \Big[\tilde{b}(\theta_i^{(1)}) + \tilde{b}(\theta_i^{(2)}) - \tilde{b}(\theta_i^{(1\cup 2)}) \Big] \Bigg) \log \ell + \dots \,, \qquad (3.24)$$

where ℓ is a parameter characterising the common size of the adjacent regions, $\theta_i^{(k)}$ is the angle in A_k and $\theta_i^{(1\cup 2)}$ the angle in $A_1 \cup A_2$ corresponding to the i-th vertex belonging to $\partial A_1 \cap \partial A_2$. In the simplest case where such vertex is not an endpoint of $\partial A_1 \cap \partial A_2$, it provides a bipartition of the angle of 2π and the corresponding contribution to the sum in (3.24) is $2\tilde{b}(\theta_i^{(1)}) = 2\tilde{b}(\theta_i^{(2)})$.

We find it instructive to consider explicitly the examples in Figs. 3.2 and 3.6. For the configurations shown in the top left, middle and right panel of Fig. 3.2, the sum within the parenthesis multiplying the logarithmic term in (3.24) is given by $8\tilde{b}(\pi/2)$, $8\tilde{b}(\pi/2)$ and $6\tilde{b}(\pi/2)$ respectively, while for the bottom middle and right panels of the same figure it reads $4\tilde{b}(\pi/4)+2\tilde{b}(\pi/2)$ and $2\tilde{b}(\pi/4)+4\tilde{b}(\pi/2)+2\tilde{b}(3\pi/4)$ respectively. As for the configurations of Fig. 3.6, such coefficient is $4\tilde{b}(\pi/4)-2\tilde{b}(\pi/2)$, $3\tilde{b}(\pi/4)+\tilde{b}(3\pi/4)-\tilde{b}(\pi/2)$ and $4\tilde{b}(\pi/2)$ for the top left, middle and right panels respectively, while it is given by $3\tilde{b}(\pi/4)+\tilde{b}(3\pi/4)-2\tilde{b}(\pi/2)$, $2\tilde{b}(\pi/2)$ and $2\tilde{b}(\pi/4)+2\tilde{b}(3\pi/4)-2\tilde{b}(\pi/2)$ for the bottom left, middle and right panels respectively. It is not difficult to get the coefficient of the logarithmic term also for the configurations in Fig. 3.8. Let us point out that for the one in the top left panel such coefficient is vanishing.

As for the Rényi entropies of domains with non smooth boundary, we have that

$$S_A^{(n)} = \tilde{a}_n\, P_A - \Bigg(\sum_{\substack{\text{vertices} \\ \text{of } \partial A}} \tilde{b}_n(\theta_i) \Bigg) \log P_A + \dots \,, \qquad (3.25)$$

where the corner function $\tilde{b}_n(\theta)$ depends on the order n and it provides $\tilde{b}(\theta)$ through the replica limit, i.e. $\lim_{n\to 1} \tilde{b}_n(\theta_i) = \tilde{b}(\theta_i)$. For the model we are dealing with, the corner function $\tilde{b}_n(\theta)$ has been found in [147]. A formula similar to (3.24) can be written for $I^{(n)}_{A_1,A_2}$, by just replacing $\tilde{a}$ with $\tilde{a}_n$ and $\tilde{b}(\theta)$ with $\tilde{b}_n(\theta)$.

3.4.2 Logarithmic negativity

Considering the scaling limit for the configurations of adjacent domains A_1 and A_2 in Figs. 3.2, 3.6 and 3.8 where ∂A_1 and ∂A_2 contain vertices, the expansion of the logarithmic negativity contains a subleading logarithmic term after the leading area law term. By analogy with the case of the entanglement entropy, it is reasonable to expect that the coefficient of the logarithmic term is obtained by summing the

contributions of the vertices occurring in ∂A_1 and ∂A_2. Extracting the coefficient of such subleading logarithmic term from the lattice numerical data is a delicate task.

Let us first discuss the method employed to get the numerical values presented in this section from the formulas discussed in §3.2. A first rough approach could consist in fitting the numerical data by a linear term, a logarithmic term and a constant one. Nevertheless, since the logarithmic contribution is tiny with respect to the linear one, its estimation can be spoiled by the occurrence of subleading lattice effects. In order to take them into account, we have inserted in our fitting analysis also some standard power law corrections, i.e. we have fitted our data with a function of the form $c_1\ell + c_{\log}\log(\ell) + c_0 + c_{-1}\ell^{-1} + \cdots + c_{-k_{\max}}\ell^{-k_{\max}}$ [147, 189], where ℓ is a characteristic length of P_{shared}. In particular, considering the domains identified by red circles in Figs. 3.2, 3.6 and 3.8, in each configuration ℓ corresponds to the edge for squares, to the shortest edge for the triangles, to the radius for the disks and to the height for the trapezoids. For each data set, in the plots we show the results of various fits performed in different ranges of ℓ, where each range is specified by the starting value ℓ_{start} and by the ending value ℓ_{end}. We fix some maximum exponent $k_{\max}$ and some ℓ_{start} by removing some initial points, which are strongly affected by lattice effects and therefore would need more corrections. Then, we plot the logarithmic coefficient obtained from different fits as a function of ℓ_{end}. The parameters $k_{\max}$, ℓ_{start} and the maximum value of ℓ_{end} are chosen in order to get a stable result from the fits in the whole range of ℓ_{end}. The logarithmic coefficient is estimated as the average of the fitted values within such range of ℓ_{end}. The error introduced through this procedure is estimated by taking the maximum deviation of the data from the average within this range of stability.

An important benchmark employed to test our numerical analysis is the mutual information of adjacent domains. In particular, we have considered the coefficient of the logarithmic term in the mutual information for the configurations in the top left, bottom middle and bottom right panels of Fig. 3.2, recovering the values of the corner function $\tilde{b}(\theta)$ for $\theta \in \{\pi/4, \pi/2, 3\pi/4\}$ available in the literature [147, 189, 200].

Let us consider the occurrence of a subleading logarithmic term due to corners in the logarithmic negativity of some configurations of adjacent domains. We first observe that the angles of A_1 and A_2 contributing to the logarithmic term in $\mathcal{E}$ are such that at least one of their sides belongs to $\partial A_1 \cap \partial A_2$, namely only the angles whose vertices lie on the curve $\partial A_1 \cap \partial A_2$ provide a non trivial logarithmic contribution. Also the endpoints of $\partial A_1 \cap \partial A_2$ have to be included among such vertices. This is expected from the guiding principle that the logarithmic negativity measures the entanglement between A_1 and A_2.

A way to check numerically this observation is to consider e.g. the coefficients of the logarithmic terms in $\mathcal{E}$ for the configurations in the top panels of Fig. 3.2. These configurations contain only three possible different contributions corresponding to

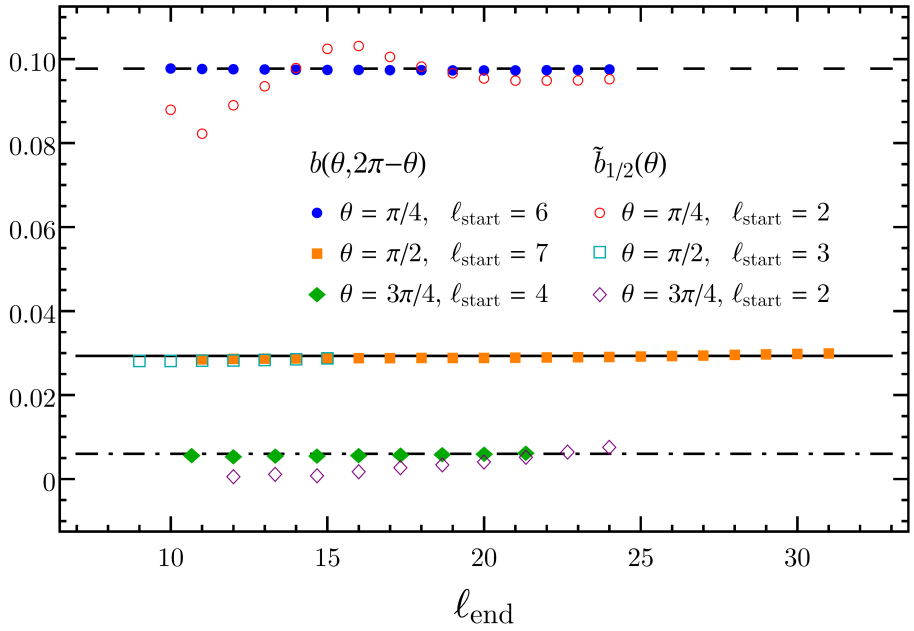

Figure 3.5: Stability analysis of the fitted values of the corner functions $b(\theta, 2\pi - \theta)$ and $\tilde{b}_{1/2}(\theta)$ for $\theta \in \{\pi/4, \pi/2, 3\pi/4\}$, as explained in §3.4.2. The configurations employed here are shown in the top left, bottom middle and bottom right panels of Fig. 3.2. The horizontal lines (with various dashing) correspond to the estimates obtained as explained in §3.4.2. The numerical values are $b(\pi/4, 7\pi/4) = 0.0977(3)$, $b(\pi/2, 3\pi/2) = 0.029(1)$ and $b(3\pi/4, 5\pi/4) = 0.0060(5)$.

this kind of vertices. Thus, one can easily solve the resulting linear system of three equations finding that the contribution coming from the four vertices which do not belong to $\partial A_1 \cap \partial A_2$ is much smaller than the other ones (by a factor of about 1/100). As further check that only the vertices lying on $\partial A_1 \cap \partial A_2$ (including its endpoints) contribute to the logarithmic term of $\mathcal{E}$, we have constructed another configuration of adjacent domains as follows: starting from a configuration like the one in the top right panel of Fig. 3.2 with $\ell_{\rm in}/\ell_{\rm out} = 1/3$ and dividing the domain corresponding to the blue dots along the diagonal with negative slope of $A_1 \cap A_2$, we have removed the upper triangle. In the resulting configuration $A_1 \cup A_2$ is a triangle and the subregion identified by the red circles is a square. Comparing the coefficients of the logarithmic term for this configuration and the one for the configuration in the top right panel of Fig. 3.2 with $\ell_{\rm in}/\ell_{\rm out} = 1/3$, we have found the same number within numerical errors.

Thus, the logarithmic negativity of adjacent domains whose boundaries share a curve containing some vertices, where its endpoints are counted among them, is given

by

$$\mathcal{E} \,=\, a\, P_{\text{shared}} - \Bigg(\sum_{\substack{\text{vertices of} \\ \partial A_1 \cap \partial A_2}} b(\theta_i^{(1)}, \theta_i^{(2)}) \Bigg) \log P_{\text{shared}} + \dots \,, \tag{3.26}$$

being $\theta_i^{(k)}$ the angle corresponding to the i-th vertex of $\partial A_1 \cap \partial A_2$ which belongs to A_k. In (3.26) we have assumed that either two or three curves meet at every vertex of $\partial A_1 \cap \partial A_2$, i.e. every vertex corresponds either to a bipartition ($\theta_i^{(1)} + \theta_i^{(2)} = 2\pi$) or to a tripartition ($\theta_i^{(1)} + \theta_i^{(2)} < 2\pi$) respectively of the angle of 2π. This assumption, which has been done also in (3.24), is verified for all the configurations in Figs. 3.2, 3.6 and 3.8.

From our numerical analysis, we find that the above considerations apply also for the quantity $\mathcal{E}_n$ defined in (1.77). Thus we have

$$\mathcal{E}_n \,=\, a_n\, P_{\text{shared}} - \Bigg(\sum_{\substack{\text{vertices of} \\ \partial A_1 \cap \partial A_2}} b_n(\theta_i^{(1)}, \theta_i^{(2)}) \Bigg) \log P_{\text{shared}} + \dots \,, \tag{3.27}$$

where the coefficient a_n has been already discussed in §3.3.2 and the corner function $b_n(\theta_i^{(1)}, \theta_i^{(2)})$ is related to the one occurring in the logarithmic term of (3.26) through the replica limit (1.81), namely $\lim_{n_e \to 1} b_{n_e}(\theta_i^{(1)}, \theta_i^{(2)}) = b(\theta_i^{(1)}, \theta_i^{(2)})$.

Among the vertices belonging to the curve $\partial A_1 \cap \partial A_2$ which contribute to the logarithmic term in (3.26) and (3.27), let us consider first the ones corresponding to pairs of explementary angles, i.e. the ones such that $\theta_i^{(1)} + \theta_i^{(2)} = 2\pi$. This kind of vertices occurs in all the panels of Fig. 3.2 except for the bottom left one (in particular, for the configurations in the top left, bottom middle and bottom right panels only this kind of vertices occurs), while it does not occur at all in the configurations of Fig. 3.6.

For these vertices we can make an observation similar to the one that leads to (3.21). Indeed, because of the local nature of the function $b_n(\theta_i, 2\pi - \theta_i)$, it is reasonable to assume that these vertices provide the same contribution given in the case of a bipartition of the ground state, when (1.80) holds. This observation leads us to propose the following relation between $b_n(\theta, 2\pi - \theta)$ and the corner function $\tilde{b}_n(\theta)$ entering in the Rényi entropies

$$b_n(\theta, 2\pi - \theta) = \begin{cases} \big(1 - n_o\big)\, \tilde{b}_{n_o}(\theta) & \text{odd } n = n_o \,, \\ 2\big(1 - n_e/2\big)\, \tilde{b}_{n_e/2}(\theta) & \text{even } n = n_e \,. \end{cases} \tag{3.28}$$

By employing the replica limit (1.81), the relation (3.28) allows to conclude that the corner function in the logarithmic negativity for this kind of vertices is equal to the corner function in the Rényi entropy of order 1/2, namely

$$b(\theta, 2\pi - \theta) = \tilde{b}_{1/2}(\theta) \,. \tag{3.29}$$

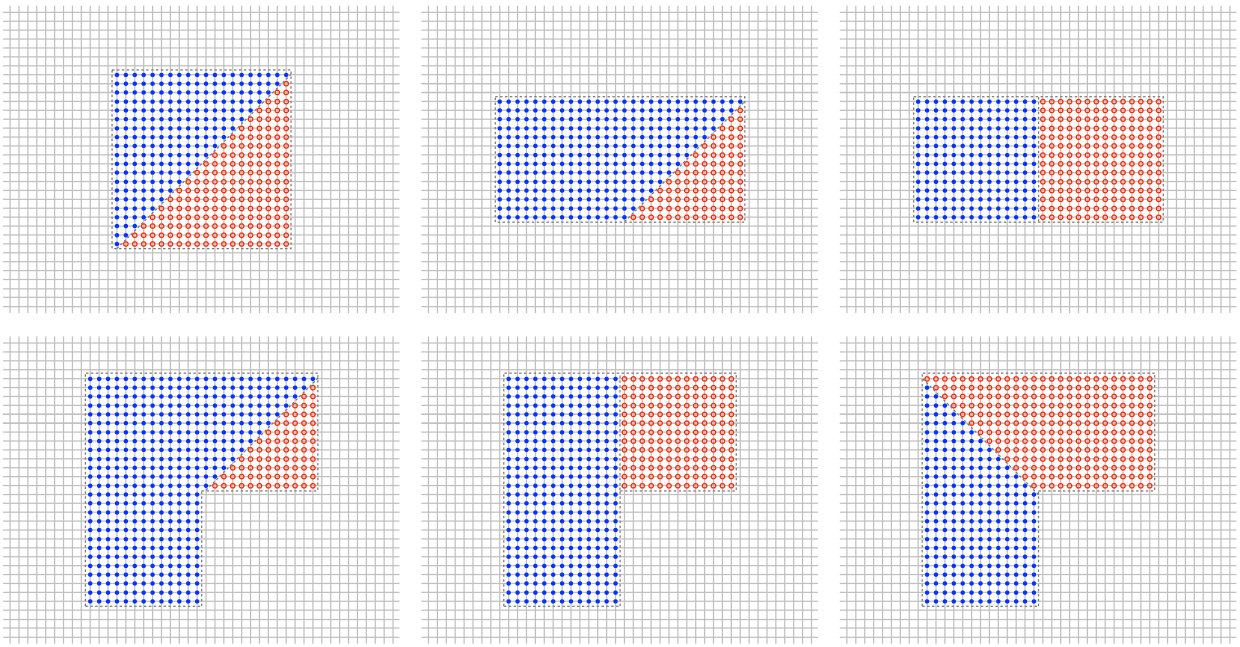

Figure 3.6: Configurations of adjacent domains on the lattice, identified by red circles and blue dots, which have been employed to find $b(\theta^{(1)}, \theta^{(2)})$ for some values of arguments such that $\theta^{(1)} + \theta^{(2)} < 2\pi$ (coloured markers in Fig. 3.7).

Numerical checks of the relation (3.29) for some values of θ are shown in Fig. 3.5. The values of $b(\theta, 2\pi - \theta)$ and $\tilde{b}_{1/2}(\theta)$ for $\theta \in \{\pi/4, \pi/2, 3\pi/4\}$ have been found by evaluating $\mathcal{E}$ and $I^{(1/2)}_{A_1,A_2}$ for the configurations shown in the top middle, bottom middle and bottom right panels of Fig. 3.2, where the curve $\partial A_1 \cap \partial A_2$ contains only the kind of vertices that we are considering. The numerical values obtained for $b(\theta, 2\pi - \theta)$ for the above opening angles are: $b(\pi/4, 7\pi/4) = 0.0977(3)$, $b(\pi/2, 3\pi/2) = 0.029(1)$ and $b(3\pi/4, 5\pi/4) = 0.0060(5)$. The corresponding numerical values obtained for $\tilde{b}_{1/2}(\theta)$ are less stable than the ones for $b(\theta, 2\pi - \theta)$. Nevertheless, they provide a reasonable check of (3.29).

An analytic expression for the function $\tilde{b}_{1/2}(\theta)$, which can be found by performing the analytic continuation $n \to 1/2$ of the formula for $\tilde{b}_n(\theta)$ obtained in [147], is not available. Considering the expansion of the corner function $\tilde{b}_n(\theta) = \sigma_n(\pi - \theta)^2 + \dots$ as $\theta \to \pi$, where the dots denote subleading contributions, in [200] it has been found that the leading term provides a lower bound, namely $\tilde{b}_n(\theta) \geqslant \tilde{b}^{\text{l.b.}}_n(\theta)$, where $\tilde{b}^{\text{l.b.}}_n(\theta) = \sigma_n(\theta - \pi)^2$. The coefficient σ_n has been computed for simple models like the Dirac fermion and the complex scalar for integer n (see e.g. Table 2 of [158]) and a duality between the free bosonic and fermionic contributions allows to get also $\sigma_{1/n}$ [158]. In particular, for the real free boson one gets $\sigma_{1/2} = \frac{1}{32\pi}$ (see Table 5 of

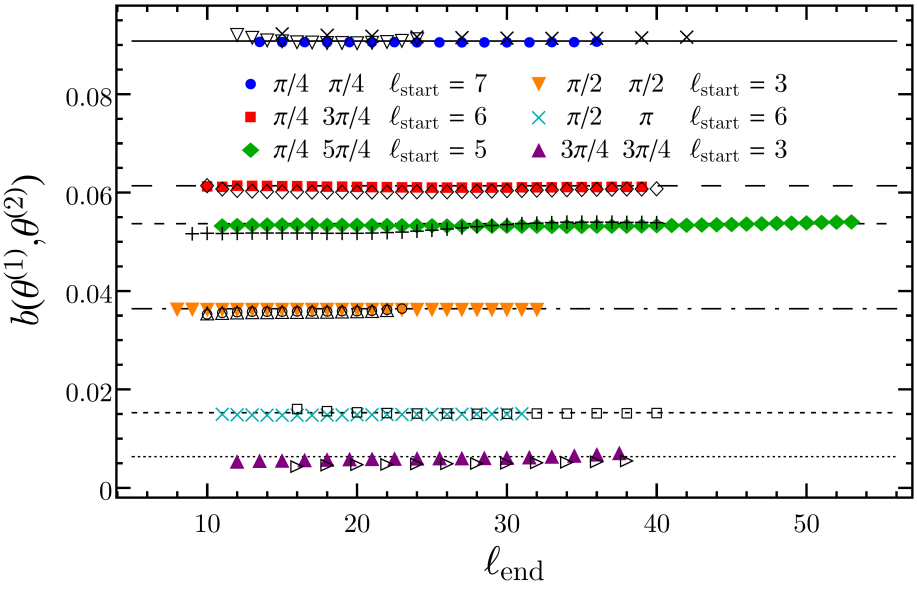

Figure 3.7: Stability analysis of the fitted values of the corner function $b(\theta^{(1)}, \theta^{(2)})$ for some pair of angles such that $\theta^{(1)} + \theta^{(2)} < 2\pi$. The data corresponding to coloured markers have been obtained by employing the configurations in Fig. 3.6, while the data corresponding to black markers have been found by using the configurations in Fig. 3.8 and the ones in the top middle and top right panels of Fig. 3.2. The horizontal lines (with various dashing) correspond to the estimates obtained as explained in §3.4.2. The numerical values are reported in (3.30).

[158]), which leads to the following lower bounds for $\tilde{b}_{1/2}(\theta)$ for the opening angles that we analysed: $\tilde{b}_n^{\rm l.b.}(\pi/4) = 0.0552$, $\tilde{b}_n^{\rm l.b.}(\pi/2) = 0.0245$ and $\tilde{b}_n^{\rm l.b.}(3\pi/4) = 0.00614$. Our numerical values for $b(\theta, 2\pi - \theta)$ are above these limiting values. The bound becomes stronger and stronger as the angle θ approaches π, as expected from the fact that the corner function decreases monotonically to zero. For $\theta = 3\pi/4$, our result satisfies the bound only once the estimated error is taken into account.

Let us consider the vertices corresponding to a tripartition of the angle 2π, for which $\theta_i^{(1)} + \theta_i^{(2)} < 2\pi$ and which are the endpoints of the curve $\partial A_1 \cap \partial A_2$ in the class of vertices that we are considering. For this kind of vertices the corner function $b_n(\theta_i^{(1)}, \theta_i^{(2)})$ depends on two independent variables. We have obtained its numerical values for some pairs of angles by employing the configurations in Fig. 3.6. The results are shown in Fig. 3.7 (coloured solid markers) and they are given by

$$\begin{array}{lll} b(\pi/4,\pi/4) = 0.0908(1) & b(\pi/4,3\pi/4) = 0.0614(3) & b(\pi/4,5\pi/4) = 0.0536(1) \\ b(\pi/2,\pi/2) = 0.0364(1) & b(\pi/2,\pi) = 0.0152(2) & b(3\pi/4,3\pi/4) = 0.0068(2)\,, \end{array} \tag{3.30}$$

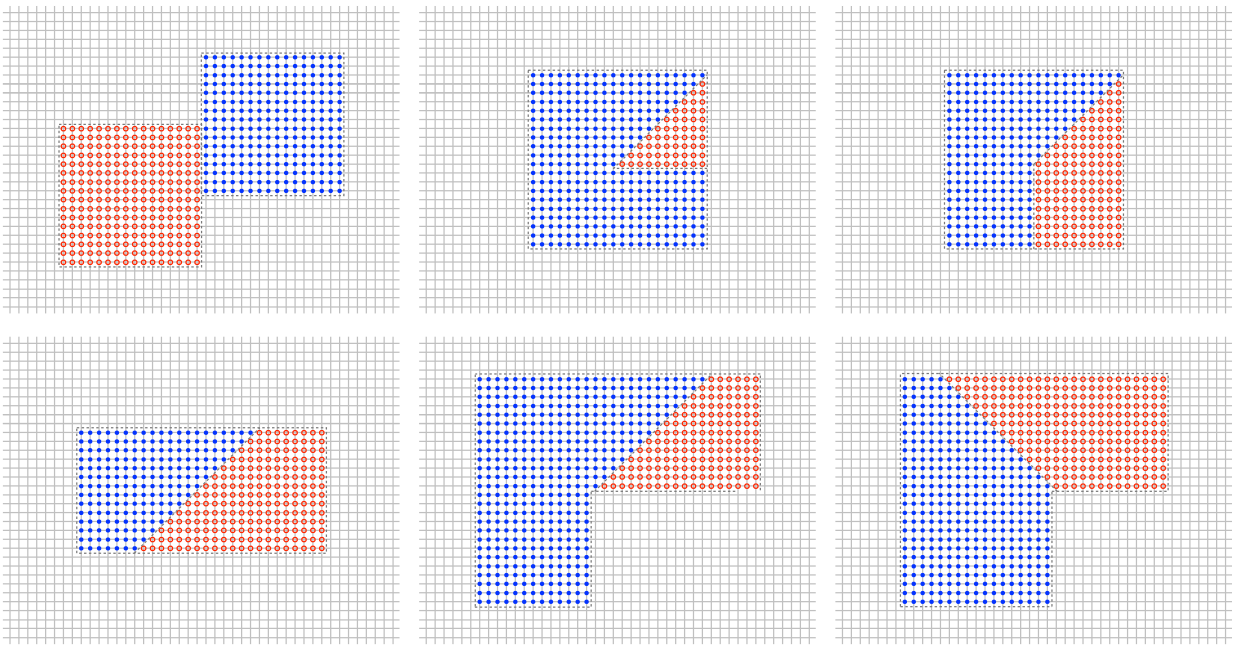

Figure 3.8: Configurations of adjacent domains on the lattice, identified by red circles and blue dots, which have been employed as crosschecks for the values of $b(\theta^{(1)}, \theta^{(2)})$ given in Fig. 3.5 and Fig. 3.7.

where the parenthesis denote the uncertainty on the last digit. In Fig. 3.7 the black markers correspond to the values obtained by employing all the configurations of Fig. 3.8 and the ones in the top middle and top right panels of Fig. 3.2.

Let us remark that the coefficient of the logarithmic term in the logarithmic negativity of the configuration in the top left panel of Fig. 3.8 is non zero, while it is vanishing in the mutual information of the same configuration, as already pointed out in §3.4.1. Moreover, such coefficient for the configuration shown in the the bottom left panel of Fig. 3.2 turns out to be zero within our numerical errors, both for the negativity and the mutual information, as expected from the fact that corners do not occur in the continuum limit.

In principle, our numerical analysis allows to find also $b_n(\theta_i^{(1)}, \theta_i^{(2)})$. Nevertheless, in order to check the relation (3.28) we need to know the unusual corrections [140] to the scaling in $2+1$ dimensions in order to perform a precise fitting analysis (see e.g. [159]).

3.4.3 Comments on the continuum limit

The continuum limit of the lattice model (3.2) considered throughout this chapter is described by the massless scalar field in $2+1$ dimensions, which is a CFT. Denoting by ε the UV cutoff that must be introduced to regularise the model, the logarithmic negativity of adjacent domains diverges when $\varepsilon \to 0$.

The numerical results on the lattice discussed above tell us that the expansion of the logarithmic negativity as $\varepsilon \to 0$ reads

$$\mathcal{E} \,=\, \alpha \, \frac{P_{\text{shared}}}{\varepsilon} - \Bigg(\sum_{\substack{\text{vertices of} \\ \partial A_1 \cap \partial A_2}} b(\theta_i^{(1)}, \theta_i^{(2)}) \Bigg) \log(P_{\text{shared}}/\varepsilon) + \dots \,, \tag{3.31}$$

where the coefficient α in front of the area law term is non universal. A similar expression can be written for $\mathcal{E}_n$ in (1.77), namely

$$\mathcal{E}_n \,=\, \alpha_n \, \frac{P_{\text{shared}}}{\varepsilon} - \Bigg(\sum_{\substack{\text{vertices of} \\ \partial A_1 \cap \partial A_2}} b_n(\theta_i^{(1)}, \theta_i^{(2)}) \Bigg) \log(P_{\text{shared}}/\varepsilon) + \dots \,, \tag{3.32}$$

where α_n is non universal as well. Instead, the corner functions $b(\theta_i^{(1)}, \theta_i^{(2)})$ and $b_n(\theta_i^{(1)}, \theta_i^{(2)})$ are independent of the UV details of the regularisation and therefore they are the most important quantities to study. In (3.31) and (3.32), like for their lattice versions (3.26) and (3.27), we have assumed that the vertices in ∂A_1 and ∂A_2 correspond either to a bipartition or to a tripartition of the angle of 2π.

The divergent terms in the $\varepsilon \to 0$ expansion of $\mathcal{E}$ and $\mathcal{E}_n$ are determined by local effects close to the curve $\partial A_1 \cap \partial A_2$, consistently with the intuition that the entanglement between A_1 and A_2 comes from the degrees of freedom living close to their shared boundary. This leads to relate the coefficients α and α_n in (3.31) and (3.32) to the area law coefficients $\tilde{\alpha}$ and $\tilde{\alpha}_n$ of S_A and $S_A^{(n)}$ like in (3.21) and (3.22). Notice that, whenever for the i-th vertex of $\partial A_1 \cap \partial A_2$ we have $\theta_i^{(1)} + \theta_i^{(2)} = 2\pi$, the relations (3.28) and (3.29) for the corner functions $b(\theta, 2\pi - \theta)$ and $b_n(\theta, 2\pi - \theta)$ hold also in the continuum limit. Instead, whenever the vertices correspond to partitions of the angle of 2π in three (i.e. $\theta_i^{(1)} + \theta_i^{(2)} < 2\pi$) or higher number of components, we expect that the corner functions occurring in $\mathcal{E}$ or $\mathcal{E}_n$ contain new information with respect to the corner functions entering in S_A or $S_A^{(n)}$.

It would be very interesting to find an analytic expression for the corner function $b(\theta, \gamma)$ for any pair of angles θ and γ, where we can assume $\theta \leqslant \gamma$. By considering only the few pairs of angles that we have studied on the lattice, we can make some observations about the behaviour of this corner function. For instance, when the two angles are equal, the function $b(\theta, \theta)$ is decreasing with $\theta \in (0, \pi]$ and $b(\pi, \pi) = 0$. Moreover, for fixed $\theta \leqslant \pi$, the function $b(\theta, \gamma)$ is decreasing with $\gamma \in (\theta, 2\pi - \theta)$. By

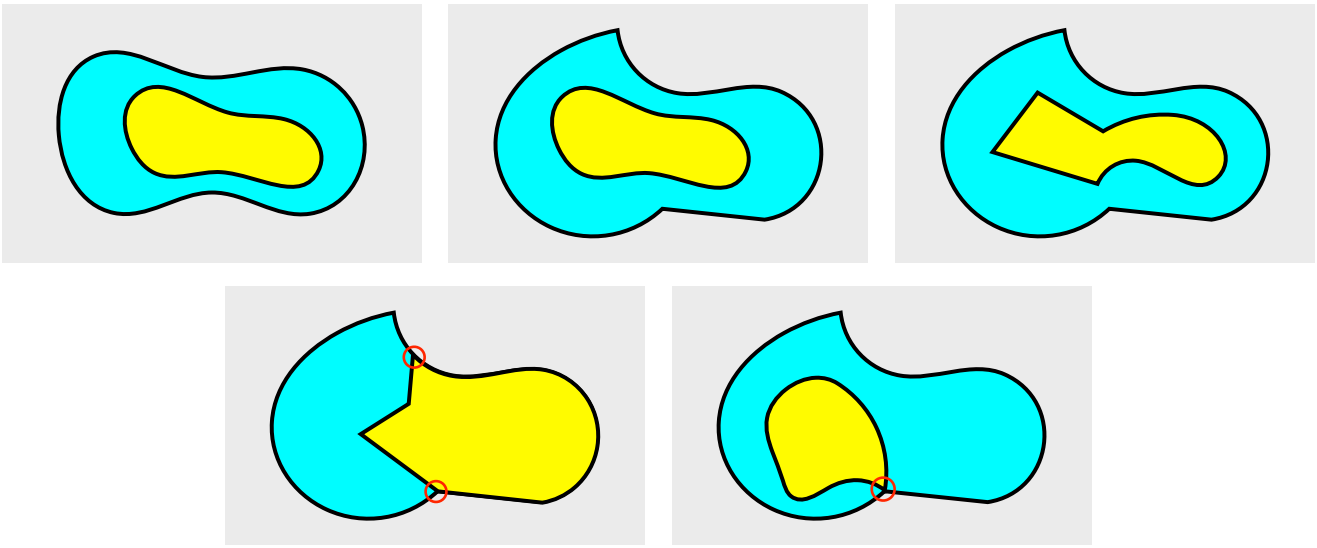

Figure 3.9: Configurations of adjacent domains A_1 and A_2 in the plane (the yellow and cyan regions). The grey part corresponds to the region B which has been traced out. The quantities $\mathcal{E}$ and $\mathcal{E}_n$ for the configurations in the top left and top middle panels do not contain a logarithmic term, while for the remaining ones such term is non vanishing. The vertices corresponding to a partition of the angle of 2π in three or four angles are highlighted with red circles.

comparing Fig. 3.7 with Fig. 3.5, one notices that this is not true anymore when γ is exactly $2\pi - \theta$. Such behaviour is not surprising because in this limit the boundaries of A_1 and A_2 merge, P_{shared} changes abruptly and therefore a continuous behaviour of the divergent terms in the logarithmic negativity is not expected.

In Fig. 3.9 we show some illustrative examples of configurations of adjacent regions in the plane. The grey region is associated to the part B, which has been traced out. Considering $\mathcal{E}$ and $\mathcal{E}_n$ between the yellow domain and the cyan domain, the expressions (3.31) and (3.32) can be employed for all the configurations in Fig. 3.9 except for the one in the bottom right panel, where the vertex highlighted by the red circle corresponds to a partition of the angle of 2π in four parts.

In the configurations shown in the top left and middle panels of Fig. 3.9 the curve $\partial A_1 \cap \partial A_2$ is smooth; therefore the logarithmic divergence does not occur in $\mathcal{E}$ and $\mathcal{E}_n$. Instead, in the remaining configurations the curve $\partial A_1 \cap \partial A_2$ contains vertices and the subleading logarithmic divergence occurs. As for the configuration in the top right panel, the coefficient of the logarithmic term of $\mathcal{E}$ and $\mathcal{E}_n$ is related to the corner functions $\tilde{b}(\theta)$ and $\tilde{b}_n(\theta)$ entering in the logarithmic term of S_A or $S_A^{(n)}$ respectively through (3.28) and (3.29). Thus, for the configurations in the top panels of Fig. 3.9

and assuming that only one scale ℓ occurs to determine the logarithmic term, one can construct the following UV finite quantity

$$\mathcal{E} - \frac{1}{2}\, I^{(1/2)}_{A_1,A_2}\,. \tag{3.33}$$

For the same configurations, also the following combinations, depending on the parity of the integer n, are UV finite

$$\mathcal{E}_{n_o} - \frac{1-n_o}{2}\, I^{(n_o)}_{A_1,A_2}\,, \qquad\qquad \mathcal{E}_{n_e} - \left(1-\frac{n_e}{2}\right) I^{(n_e/2)}_{A_1,A_2}\,. \tag{3.34}$$

The second expression in (3.34) provides (3.33) after the analytic continuation $n_e \to 1$. In a $2+1$ dimensional CFT, the quantities in (3.33) and (3.34) should give non trivial scale invariant functions of the parameters characterising the adjacent domains. For example, when the adjacent domains are given by a disk of radius R_{in} and an annulus surrounding it whose radii are $R_{\text{in}} < R_{\text{out}}$, the expression (3.33) should be a model dependent function of the ratio $R_{\text{in}}/R_{\text{out}}$. It would be very interesting to develop a method which allows to get an analytic expression for this function.

The configurations of adjacent domains shown in the bottom panels of Fig. 3.9 are more interesting because the corner functions corresponding to the vertices highlighted by the red circles is not related to the corner functions occurring in the entanglement entropies. Thus, because of such terms, we expect that the combinations in (3.33) and (3.34) diverge logarithmically for these configurations.

3.5 Conclusions

In this chapter we have investigated the logarithmic negativity $\mathcal{E}$ and the moments of the partial transpose for adjacent domains A_1 and A_2 in the ground state of a two dimensional harmonic square lattice with nearest neighbour spring-like interaction. The regime of massless oscillators in the thermodynamic limit has been considered.

By exploring various configurations of adjacent domains, we have shown that, at leading order for large domains, the logarithmic negativity and the quantity $\mathcal{E}_n$ introduced in (1.77) satisfy an area law in terms of the length of the shared curve $\partial A_1 \cap \partial A_2$, suggesting a relation between the coefficient of the area law term in these quantities and the coefficient of the area law term in the Rényi entropies.

A subleading universal logarithmic term occurs in $\mathcal{E}$ and $\mathcal{E}_n$ whenever the shared curve contains vertices, being its endpoints included among them. The values of the corner function of $\mathcal{E}$ have been obtained for some pairs of angles. For the vertices of $\partial A_1 \cap \partial A_2$ corresponding to pairs of explementary angles, we have proposed that the corner function of $\mathcal{E}_n$ is related to the corner function entering in the Rényi entropies [147]. This relation implies that the corner function of $\mathcal{E}$ for this kind of vertices

coincides with the corner function of the Rényi entropy of order 1/2. This statement has been supported by numerical evidences shown in Fig. 3.5.

As for the vertices of the curve $\partial A_1 \cap \partial A_2$ corresponding to a tripartition of the angle of 2π, their contribution to the logarithmic term in $\mathcal{E}$ and $\mathcal{E}_n$ is characterised by a new corner function which depends on two independent angular variables. The numerical values of this corner function for $\mathcal{E}$ have been given in (3.30) for some pair of angles (see also Fig. 3.7).

Let us conclude with some open questions. It would be interesting to provide further checks of (3.29). In particular, the analytic continuation to $n = 1/2$ of the corner function found by Casini and Huerta [147] should be performed. More importantly, a method should be found to compute analytically the corner functions $b(\theta, \gamma)$ and $b_n(\theta, \gamma)$ for the vertices partitioning the angle of 2π in three parts. By analogy with the results of [154, 157] obtained for the corner function of S_A, it could be interesting to study the corner function $b(\theta, \theta)$ for equal angles as $\theta \to \pi^-$. In order to extract reliable numerical results for the logarithmic term of $\mathcal{E}_n$ from the fit of the lattice data, the unusual corrections to the scaling must be studied, extending the analysis done by Cardy and Calabrese [140] in $1 + 1$ dimensions. Finally, it is worth studying the corner contributions to $\mathcal{E}$ and $\mathcal{E}_n$ for other models, both on the lattice and in the continuum.

Chapter 4

Comments on Entanglement Contour for Logarithmic Negativity

This chapter contains some preliminary results about the spatial distribution of entanglement entropy and negativity. This on-going project is in collaboration with Andrea Coser and Erik Tonni.

4.1 Introduction

Which real-space degrees of freedom contribute, and how much, to the entanglement of a region A with another region B? Is there a way to understand the spatial structure of entanglement? In 2004, Botero and Reznik [179] studied the spatial structure of vacuum entanglement for bosonic oscillators introducing the so called *mode participation function*. Ten years later, this lead Chen and Vidal [201] to introduce the *entanglement contour* in the context of fermionic modes. The bosonic case has then been studied by Frérot and Roscilde [202]. These concepts try to answer the above questions providing a decomposition into single site contributions for the entanglement entropy. As we already explained in §1.7, the area law (1.82) is understood as resulting from entanglement that involves degrees of freedom located near the boundary between regions A and B. Also intuitively, the logarithmic correction we described in §1.7 is argued to have its origin in contributions to entanglement from degrees of freedom that are further away from the boundary between A and B. The goal of this chapter is to discuss the contour, which is capable of testing the above intuitions [201]. With respect to the previous works, we study the contour for the harmonic chain in $1+1$-dimensions for disjoint intervals and try to extend it to the logarithmic negativity.

Given an entanglement measure E_A, the idea is to introduce a positive function, the *entanglement contour*, that assigns a real number $e_A(i) \geq 0$ to each lattice site i contained in region A such that

$$E_A = \sum_{i \in A} e_A(i)\,, \tag{4.1}$$

The entanglement contour quantifies how much the degrees of freedom in site i contributes to the entanglement between A and B. In [201], Chen and Vidal listed some properties that should characterize the entanglement contour

(i) Positivity: $e_A(i) \geq 0\,.$

(ii) Sum rule: $\sum_{i \in A} e_A(i) = E_A\,.$

(iii) Symmetry: if G is a symmetry of ρ_A, that is $G\rho_A G^\dagger = \rho_A$, and G exchanges site i with site j, then $e_A(i) = e_A(j)\,.$

(iv) Invariance under local unitary transformations: if two states are connected by a unitary transformation $U_{A'}$ that acts on a subset $A' \subseteq A$ of sites in A, then $e_A(A')$ must be the same for both states.

Moreover, some upper and lower bounds on the entanglement contour are required by the above authors but since they are too technical and not relevant for our discussion, we refer the reader to [201] for a detailed explanation.

For bipartite pure states we will consider the entanglement contour for the entanglement entropy (*entanglement entropy contour*), i.e. $S_A = \sum_{i \in A} s_A(i)$,where $s_A(i)$ quantifies how much the site i contributes to the entanglement between A and its complement. For mixed states we will focus on the contour for the logarithmic negativity (*entanglement negativity contour*), i.e. $\mathcal{E} = \sum_{i \in A} \varepsilon(i)$, where $\varepsilon(i)$ measures the weight of the site i in the negativity between A_1 and A_2 (as usual $A = A_1 \cup A_2$) that are embedded in a larger region B.

4.2 Entanglement entropy contour for free fermions

The determination of the entanglement structure of a given quantum state is a complicated problem. However, things are simplified if we consider a pure Gaussian state, which can be shown to be equivalent to products of pairs of entangled modes [203, 204]. In the following construction, as described in [201], we will deal with a Gaussian quantum state ρ for a set of N fermonic modes. The Hamiltonian of the fermionic system is quadratic and we can think about ρ as its ground state.

Let us consider a fermionic lattice system made of N sites characterized by a set of N fermionic annihilation operators b_i, $i = 1, \ldots, N$ such that

$$\{b_i^\dagger, b_j\} = \delta_{ij}\,, \quad \{b_i, b_j\} = 0\,. \tag{4.2}$$

There are two Majorana operators $\psi_{i,1}$ and $\psi_{i,2}$ associated to each site i, defined by

$$\psi_{i,1} \equiv \frac{b_i + b_i^\dagger}{\sqrt{2}}\,, \quad \psi_{i,2} \equiv \frac{b_i - b_i^\dagger}{i\sqrt{2}}\,. \tag{4.3}$$

It is easy to check that $\{\psi_{i,\alpha}, \psi_{j,\beta}\} = \delta_{ij}\delta_{\alpha\beta}$. Now, let us consider the usual bipartition of our lattice system in a region A of N_A sites and its complement B. In this case the reduced density matrix $\rho_A = \mathrm{Tr}_B\,\rho$ is completely characterized by its correlation matrix Γ_A. In terms of the Majorana modes we can write it as

$$(\Gamma_A)_{i,\alpha;j,\beta} = -\mathrm{i}\langle[\psi_{i,\alpha}, \psi_{j,\beta}]\rangle\,, \quad i, j = 1, \ldots, N_A\,. \tag{4.4}$$

Γ_A is antisymmetric and therefore there exists an orthogonal matrix such that

$$O^T \Gamma_A O = \Lambda_A, \qquad \Lambda_A = \bigoplus_{k=1}^{N_A} \begin{pmatrix} 0 & \mu_k \\ -\mu_k & 0 \end{pmatrix}, \tag{4.5}$$

with $-1 \leq \mu_k \leq 1$. The matrix Λ_A can be diagonalized by of the unitary matrix

$$W = \frac{1}{\sqrt{2}} \bigoplus_{k=1}^{N_A} \begin{pmatrix} 1 & -\mathrm{i} \\ -\mathrm{i} & 1 \end{pmatrix}. \tag{4.6}$$

The following matrix $\frac{\mathbb{I}+\mathrm{i}\Gamma_A}{2}$ can be diagonalized using both O and W

$$\frac{\mathbb{I} + \mathrm{i}\Gamma_A}{2} = \langle \psi_{i,\alpha}\psi_{j,\beta}\rangle = OW \left(\bigoplus_{k=1}^{N_A} \begin{pmatrix} \frac{1+\mu_k}{2} & 0 \\ 0 & \frac{1-\mu_k}{2} \end{pmatrix} \right) W^\dagger O^T. \tag{4.7}$$

These considerations lead us to write the entanglement entropy of this fermionic system in the following useful form

$$S_A^f = \mathrm{Tr}(f(\Gamma_A)) = \sum_{k=1}^{N_A} S^f(\mu_k)\,, \tag{4.8}$$

where

$$f(\Gamma_A) = -\frac{\mathbb{I} + \mathrm{i}\Gamma_A}{2} \log\left(\frac{\mathbb{I} + \mathrm{i}\Gamma_A}{2}\right) . \tag{4.9}$$

and

$$S^f(\mu_k) = -\frac{1+\mu_k}{2} \log\left(\frac{1+\mu_k}{2}\right) - \frac{1-\mu_k}{2} \log\left(\frac{1-\mu_k}{2}\right) , \tag{4.10}$$

We can now define the delocalized Majorana modes $\phi_{k,\beta}$ as

$$\phi_{k,\beta} \equiv \sum_{i=1}^{N_A} \sum_{\alpha=1}^{2} (O^T)_{k,\beta;i;\alpha} \psi_{i,\alpha} \, . \tag{4.11}$$

This orthogonal transformation connects the delocalized modes $\phi_{k,\beta}$ with the real space modes $\psi_{i,\alpha}$. For each site i, these orthogonal transformations can be used to define the *mode participation function* $\mathcal{P}^k(i)$

$$\mathcal{P}^k(i) \equiv \frac{1}{2} \sum_{\alpha,\beta=1}^{2} (O_{i,\alpha;k,\beta})^2 \, , \tag{4.12}$$

which reflects the weight that the pair of delocalized Majorana modes $\phi_{k,1}$ and $\phi_{k,2}$ have in the Majorana modes $\psi_{i,1}$ and $\psi_{i,2}$ on site i. Since for this fermionic systems $\mathcal{P}^k(i)$ is by definition positive $\mathcal{P}^k(i) \geq 0$ and $\sum_i^{N_A} \mathcal{P}^k(i) = 1$, it can be interpreted as a probability. From it, we can define the entanglement entropy contour as

$$s_A^f(i) = \sum_{i=1}^{N_A} \mathcal{P}^k(i) S^f(\mu_k) \, . \tag{4.13}$$

We can easily see that the entanglement entropy contour for fermions $s_A^f(i)$ is positive, being a weighted sum of $\mathcal{P}^k(i)$ and $S^f(\mu_k)$, which is positive in the range $-1 \leq \mu_k \leq 1$. The contour (4.13) is obtained by inserting the projector onto site i, that is $M^{(i)} = \sum_{\alpha=1,2} |i,\alpha\rangle \langle i,\alpha|$

$$s_A^f(i) = \mathrm{Tr}(M^{(i)} f(\Gamma_A)). \tag{4.14}$$

This form is extremely useful in order to prove the property listed in the introduction of this chapter.

4.3 Entanglement entropy contour for free bosons

In this section we will consider a Gaussian quantum state ρ given by the ground state of N bosonic modes [179]. The canonical variables can be collected into the following vector

$$\eta = (q, p)^T \, , \tag{4.15}$$

where $q = (q_1, q_2, \cdots, q_N)^T$ and $p = (p_1, p_2, \cdots, p_N)^T$. The canonical commutation relations give

$$[\eta_\alpha, \eta_\beta] = iJ_{\alpha\beta}\,, \tag{4.16}$$

where J is the following matrix

$$J = \begin{pmatrix} 0 & \mathbb{I}_N \\ -\mathbb{I}_N & 0 \end{pmatrix}\,. \tag{4.17}$$

A $(2N \times 2N)$-matrix S, with entries in $\mathbb{R}$, is said to be part of the (real) symplectic group $Sp(2N, \mathbb{R})$ if and only if $SJS^T = J$. A Gaussian quantum state ρ for a set of N modes is uniquely characterized by the first and second moments of η, which are $\langle\eta\rangle$ and $\langle\eta\eta^T\rangle$ respectively. For simplicity we consider the case with $\langle\eta\rangle = 0$ and take care only of the second moment, the so-called *covariance matrix*

$$M = Re\,\langle\eta\eta^T\rangle\,. \tag{4.18}$$

Under a symplectic transformation $\tilde{\eta} = S\eta$, a Gaussian state characterized by a covariance matrix M gets mapped to another Gaussian state characterized by the covariance matrix $\tilde{M} = SMS^T$.

An important tool in our discussion is the *Williamson theorem* [205]: if M is symmetric and positive definite, a symplectic transformation S always exists that brings M to the normal form

$$W = D \oplus D = SMS^T\,, \tag{4.19}$$

where $D = diag(\lambda_1, \lambda_2, \cdots, \lambda_N)$. The elements λ_i for $i = 1, \cdots, N$, are called the *symplectic eigenvalues* of M. They must be greater than or equal to $1/2$, according to Eq. (4.16), which is nothing else than the uncertainty principle. With the symplectic transformation that diagonalizes W we can define a new set of modes, *Williamson modes*, $\tilde{\eta} = S\eta$ and decompose the components of $\tilde{\eta}$ into creation and annihilation operators

$$\tilde{q}_k = \frac{\tilde{a}_k^\dagger + \tilde{a}_k}{\sqrt{2}}\,, \quad \tilde{p}_k = i\frac{\tilde{a}_k^\dagger - \tilde{a}_k}{\sqrt{2}}\,. \tag{4.20}$$

Suppose now to partition our system of oscillators in two sets, one of $N_A < N$ sites and the complement. The reduced density matrix of the region A can be factorized as follows [178, 186]

$$\rho_A = \bigotimes_{k=1}^{N_A} \rho_k\,, \quad \rho_k = (1 - e^{-\beta_k})\, e^{-\beta_k \tilde{n}_k}\,, \tag{4.21}$$

where $\tilde{n}_k = \tilde{a}_k^\dagger \tilde{a}_k$ is the number operator. The Boltzmann factor β_k is related to the symplectic eigenvalues λ_k via the relation

$$\beta_k = \log\frac{\lambda_k + 1/2}{\lambda_k - 1/2} \quad \Leftrightarrow \lambda_k = \frac{1}{2}\coth\left(\frac{\beta_k}{2}\right)\,. \tag{4.22}$$

Now, because the eigenvalues of ρ_k are

$$m_n^{(k)} = (1 - e^{-\beta_k})\, e^{-\beta_k n}\,, \quad n = 0, 1, \dots\,, \tag{4.23}$$

we can easily calculate the entanglement entropy

$$S_A = \sum_{k=1}^{N_A} \rho_k \log \rho_k = \sum_{k=1}^{N_A} \sum_{n=0}^{\infty} m_n^{(k)} \log m_n^{(k)}\,. \tag{4.24}$$

Applying (4.22) and (4.23), the entanglement entropy can be expressed in terms of the symplectic eigenvalues as

$$S_A = \sum_{i \in A} S(\lambda_i)\,, \quad S(\lambda) = \left(\lambda + \frac{1}{2}\right) \log\left(\lambda + \frac{1}{2}\right) - \left(\lambda - \frac{1}{2}\right) \log\left(\lambda - \frac{1}{2}\right)\,. \tag{4.25}$$

The local covariant matrix of the subsystem A is defined as follows

$$M_A = \langle \eta_A \eta_A^T \rangle = \begin{pmatrix} \langle q_i\, q_j \rangle & \langle q_i\, p_j \rangle \\ \langle p_i\, q_j \rangle & \langle p_i\, p_j \rangle \end{pmatrix}\,, \quad i, j \in A\,. \tag{4.26}$$

It is convenient to introduce

$$\mathbb{Q} = \langle q\, q^T \rangle\,, \quad \mathbb{P} = \langle p\, p^T \rangle\,, \tag{4.27}$$

which are symmetric matrices, $\mathbb{Q} = \mathbb{Q}^T$ and $\mathbb{P} = \mathbb{P}^T$. In this thesis we will deal only with Gaussian states for which $\langle q\, p^T \rangle = 0$ and therefore we can write

$$M_A = \langle \eta_A \eta_A^T \rangle = \begin{pmatrix} \langle q_i\, q_j \rangle & 0 \\ 0 & \langle p_i\, p_j \rangle \end{pmatrix}\,, \quad i, j \in A\,. \tag{4.28}$$

Since the local covariance matrix M_A is block diagonal, its symplectic eigenvalues can be obtained from the square root of the doubly degenerate spectrum of the matrix

$$-\,(J_A M_A)^2 = \begin{pmatrix} \mathbb{P}_A\, \mathbb{Q}_A & 0 \\ 0 & \mathbb{Q}_A\, \mathbb{P}_A \end{pmatrix}\,. \tag{4.29}$$

In other words, the symplectic eigenvalues are given by the square root of the eigenvalues of $\mathbb{P}_A\, \mathbb{Q}_A$ (or $\mathbb{Q}_A\, \mathbb{P}_A$, being that $\mathbb{Q}_{\mathbb{A}}\, \mathbb{P}_{\mathbb{A}} = (\mathbb{P}_{\mathbb{A}}\, \mathbb{Q}_{\mathbb{A}})^T$). How do the local modes contribute to each of the collective Williamson modes? This can be answered by studying the symplectic transformation $\tilde{\eta} = S\eta$ between the local and global modes. In particular we want to directly relate the symplectic transformation to the eigenvectors of $\mathbb{P}_A\, \mathbb{Q}_A$ (or $\mathbb{Q}_A\, \mathbb{P}_A$). Since we previously set $\langle p\, q \rangle = 0$, the symplectic transformations do not mix the q's and p's, so we can write

$$\tilde{q}_A = U\, q_A\,, \quad \tilde{p}_A = V\, p_A \quad U\, V^T = 1\,, \tag{4.30}$$

where the last condition guarantees that the transformation is symplectic. Now, say D_A the diagonal matrix with the symplectic eigenvalues of M_A. Thus D_A may be written as

$$D_A = U\,\mathbb{Q}_A\,U^T = V\,\mathbb{P}_A\,V^T\,. \tag{4.31}$$

where for clearness we emphasize that the above expressions are not equations for the eigenvalues of $\mathbb{Q}$ and $\mathbb{P}$, since $U^T \neq U$ and $V^T \neq V$. They just follow from Eq. 4.29 and $SJS^T = J$. Let $u^{(m)}$ and $v^{(m)}$ be right eigenvectors of $\mathbb{P}_A\,\mathbb{Q}_A$ and $\mathbb{Q}_A\,\mathbb{P}_A$, respectively. corresponding to the symplectic eigenvalue λ_m, so that

$$(\mathbb{P}_A\,\mathbb{Q}_A)\,u^{(m)} = \lambda_m^2 u^{(m)}\,, \quad (\mathbb{Q}_A\,\mathbb{P}_A)\,v^{(m)} = \lambda_m^2 v^{(m)}\,. \tag{4.32}$$

It is convenient to introduce the normalization

$$u^{(m)T} v^{(m)} = 1\,. \tag{4.33}$$

It is then possible to see that

$$v^{(m)} = c_m \mathbb{Q}_A u_{(m)}\,, \quad u^{(m)} = d_m \mathbb{P}_A v^{(m)}\,, \tag{4.34}$$

where the proportionally constant c_m, d_m must satisfy the condition $c_m d_m = 1/\lambda_m^2$. A natural choice to make is $c_m = d_m = \lambda_m^{-1}$, implying that $u^{(m)}$ and $v^{(m)}$ must be normalized so that

$$v^{(m)T} \mathbb{P}_A v^{(m)} = u^{(m)T} \mathbb{Q}_A u^{(m)} = \lambda_m\,. \tag{4.35}$$

Since $\mathbb{Q}_A$ and $\mathbb{P}_A$ are symmetric, $u^{(m)}$ and $v^{(m)}$ are respectively the right and left eigenvectors of $\mathbb{P}_A\,\mathbb{Q}_A$. This implies, together with (4.33), the following spectral decomposition and orthogonality condition

$$\mathbb{P}_A\,\mathbb{Q}_A = \sum_m \lambda_m^2 u^{(m)} v^{(m)T}\,, \quad u^{(m)T} v^{(n)} = \delta_{mn}\,. \tag{4.36}$$

Using Eqs. (4.34) and the orthogonality condition above, we finally arrive at the following condition

$$v^{(m)T} \mathbb{P}_A v^{(n)} = u^{(m)T} \mathbb{Q}_A u^{(n)} = \lambda_m \delta_{mn}\,. \tag{4.37}$$

We can now build the symplectic transformation matrix U. Let Φ_i be a column vector with all entries set to zero except the ith one. One can then verify by direct substitution that the matrices

$$U = \sum_m \Phi_m u^{(m)T}\,, \quad V = \sum_m \Phi_m v^{(m)T}\,, \tag{4.38}$$

satisfy Eq. (4.31). It is now interesting to express the relation between the local and collective phase-space (global) modes as

$$\tilde{q}_A^{(m)} = \sum_{i\in A} u_i^{(m)} q_i \,, \quad \tilde{p}_A^{(m)} = \sum_{i\in A} v_i^{(m)} p_i \,. \tag{4.39}$$

Now, if the local site creation operator is defined as

$$a_i = \frac{1}{2}[\xi q_i + \xi_i^{-1} p_i] \,, \tag{4.40}$$

where ξ is some arbitrary dimensional parameter, the creation operator for the m-th Williamson can be expanded as

$$\tilde{a}_m = \frac{1}{2}\sum_{i\in A}\left[(\xi_i^{-1}u_i^{(m)} + \xi_i v_i^{(m)})a_i + (\xi_i^{-1}u_i^{(m)} - \xi_i v_i^{(m)})a_i^\dagger\right] . \tag{4.41}$$

This expression can be recast into a more convenient form

$$\tilde{a}_m = \sum_i \sqrt{\mathcal{P}^{(m)}(i)}\,[\cosh\, \tau_i^{(m)} a_i + \sinh\, \tau_i^{(m)} a_i^\dagger] \,, \tag{4.42}$$

where

$$\mathcal{P}^{(m)}(i) \equiv u_i^{(m)} v_i^{(m)} \tag{4.43}$$

and

$$\tau^{(m)}(i) \equiv \tanh^{-1}\left(\frac{u_i^{(m)} - \xi_i^2 v_i^{(m)}}{u_i^{(m)} + \xi_i^2 v_i^{(m)}}\right) . \tag{4.44}$$

From (4.33) one can easily check that $\sum_i \mathcal{P}^{(m)}(i) = 1$. For each mode m, the function $\mathcal{P}^{(m)}(i)$ captures the weight of the local site participation and for this reason is called *mode participation function.*

In Fig. 4.1, it is shown the 3D plot of the mode participation function $\mathcal{P}^m(i)$ of the entanglement entropy of a single interval of length $\ell_A = N_A = 60$ in a periodic chain of total length $L = N = 300$ for the free massless boson. The modes are ordered according to their corresponding eigenvalue, from the greatest to the lowest. One can appreciate how for the dominant mode $\mathcal{P}^{(m)}(i)$ has two peaks close to the boundary between A and B, while the less relevant mode has a peak in the center of the interval.

4.3.1 Estimating the central charge form the entanglement entropy contour

In [201], Vidal and Chen proposed the following ansatz for the entanglement contour of one interval in $1+1$ dimensions for free fermions

$$s_A(i) = \frac{c}{3}\frac{\ell/2}{(\ell - i - 1/2)(i + 1/2)} \,. \tag{4.45}$$

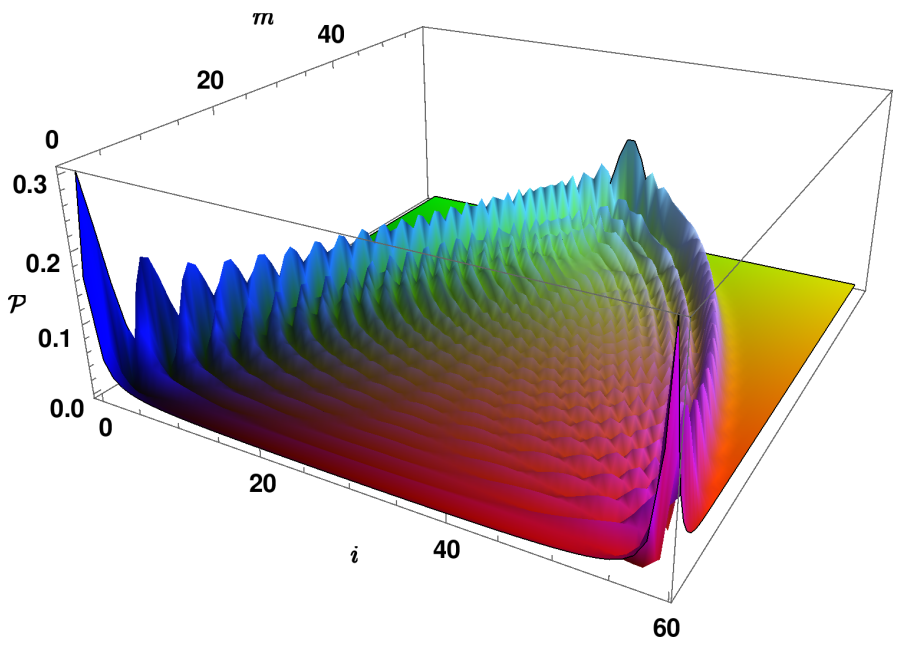

Figure 4.1: The mode participation function $\mathcal{P}^m(i)$ for the entanglement entropy of a single interval of length $N_A = 60$ in a periodic chain of total length $N = 300$ for the free massless boson. The mode participation function, as said in the main text, gives a measure of how much the ith site of the subregion A contributes to the m-mode. The modes are ordered according to their corresponding eigenvalue, from the greatest to the lowest. One can appreciate how for the first dominant mode $\mathcal{P}^{(m)}(i)$ has two peak close to the boundary between A and B, while the less relevant mode has a peak in the center of the interval.

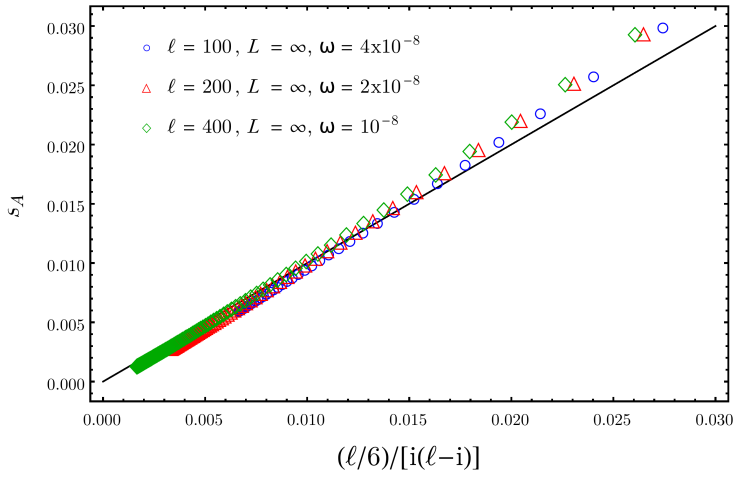

Figure 4.2: Entanglement entropy contour $s_A(i)$ of three different intervals of length $\ell = 100, 200, 400$ in an infinite harmonic chain (thermodynamic limit) plotted against Eq. (4.45) with $c = 1$ ($\omega\ell = 4 \cdot 10^{-10}$ is kept fixed). The black line represents $c = 1$.

where $\ell = N_A$ is the length of the interval A, and $i = 0, \dots, \ell - 1$, labels its sites. This formula is compatible with the entanglement entropy when the large ℓ limit is taken and we can replace the sum over sites by an integral

$$\sum_{i=0}^{\ell-1} s_A(i) = \frac{c}{3} \sum_{j=1/2}^{\ell-1/2} \frac{\ell}{2(\ell-j)j} = \frac{c}{6} \int_{\frac{1}{2\ell}}^{\frac{2\ell-1}{2\ell}} \frac{dx}{x(1-x)} = \frac{c}{3} \log \ell + O(1)\,. \tag{4.46}$$

Considering our bosonic oscillators in the thermodynamic limit, in Fig. 4.2, we plot the entanglement contour of an interval of length ℓ, keeping $\omega\ell = 4 \cdot 10^{-6}$ fixed. The black line is Eq. (4.45) with $c = 1$, the central charge of the underline CFT. The estimation works, but is not as accurate as the one for fermions shown in Fig. 6 of [201]. Note that we had to compute the entanglement profile for a single region, while using entanglement entropy to find c requires a large number of subregions. Notice that Eq. (4.45) corresponds to the entanglement temperature $\beta(x)$ for one interval in one dimension [206, 207]

$$H_A = \int_A \beta(x) T_{00}(x)\,, \quad H_A = -\log \rho_A\,, \tag{4.47}$$

where H_A is the entanglement Hamiltonian and T_{00} is the energy density. In our preliminary study we wanted to push forward this analogy and check if it was correct also for finite systems with periodic boundary conditions (PBC). In [207], the entanglement temperature for this case is written and simply consists in taking Eq. (4.45)

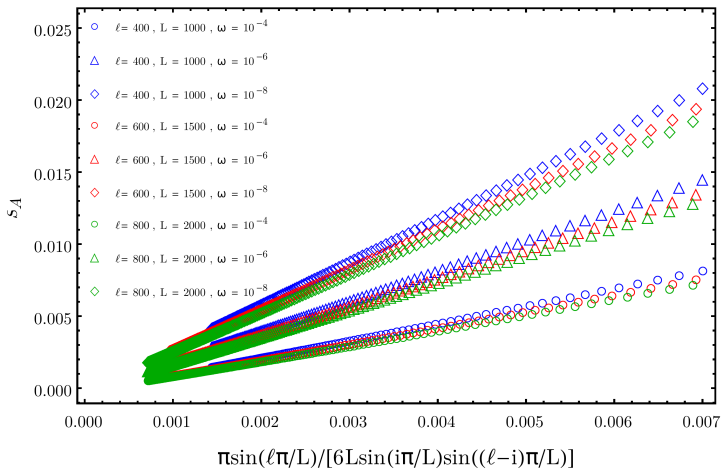

Figure 4.3: Entanglement entropy contour of an interval of length $\ell = 80$ in a chain of length $L = N = 200$, plotted with respect to the finite size version of Eq. (4.45). The three main lines corresponds to different masses $\omega = 10^{-4}$ (blue), 10^{-6} (red), 10^{-8} (green). The three different markers corresponds to different $\ell = 400, 600, 800$, keeping fixed the ratio $\ell/L = 2/5$. A dependence on the mass is evident.

and substitute $\ell \to L/\pi \sin(\ell\pi/L)$, $(\ell - i - 1/2) \to L/\pi \sin((\ell - i - 1/2)\pi/L)$ and $(i + 1/2) \to L/\pi \sin((i + 1/2)\pi/L)$. However, in the case of finite size systems and PBC, as shown in Fig. 4.3, the estimation of the central charge seems not to work properly. We numerically checked three different small masses $m = 10^{-4}, 10^{-6}, 10^{-8}$ and three different $\ell = 400, 600, 800$ keeping $\ell/L = 2/5$ fixed. It is easy to notice that none of the slopes is one. Moreover, they are all different and a dependence on the small mass is evident. This remains an open problem in our preliminary analysis.

4.3.2 Positivity of the entanglement entropy contour for bosons

As already mentioned in §4.1, the entanglement contour was first introduced in [201] to decompose the bipartite entanglement entropy of lattice free fermions between two extended regions A and B into different contributions, each from single site in A. By construction, as described in §4.2, both the participation function and the contour for fermions are positive and therefore this is in agreement with the properties required in [201] and listed in §4.1. In §4.3, the mode participation function of bosonic Gaussian oscillators was introduced and also numerically studied when A is a single interval. In [202], Frérot and Roscilde generalized the notion of contour to the entanglement of any quadratic (bosonic or fermionic) lattice Hamiltonian. In their work they pointed out the possibility that the contour for bosons might be negative,

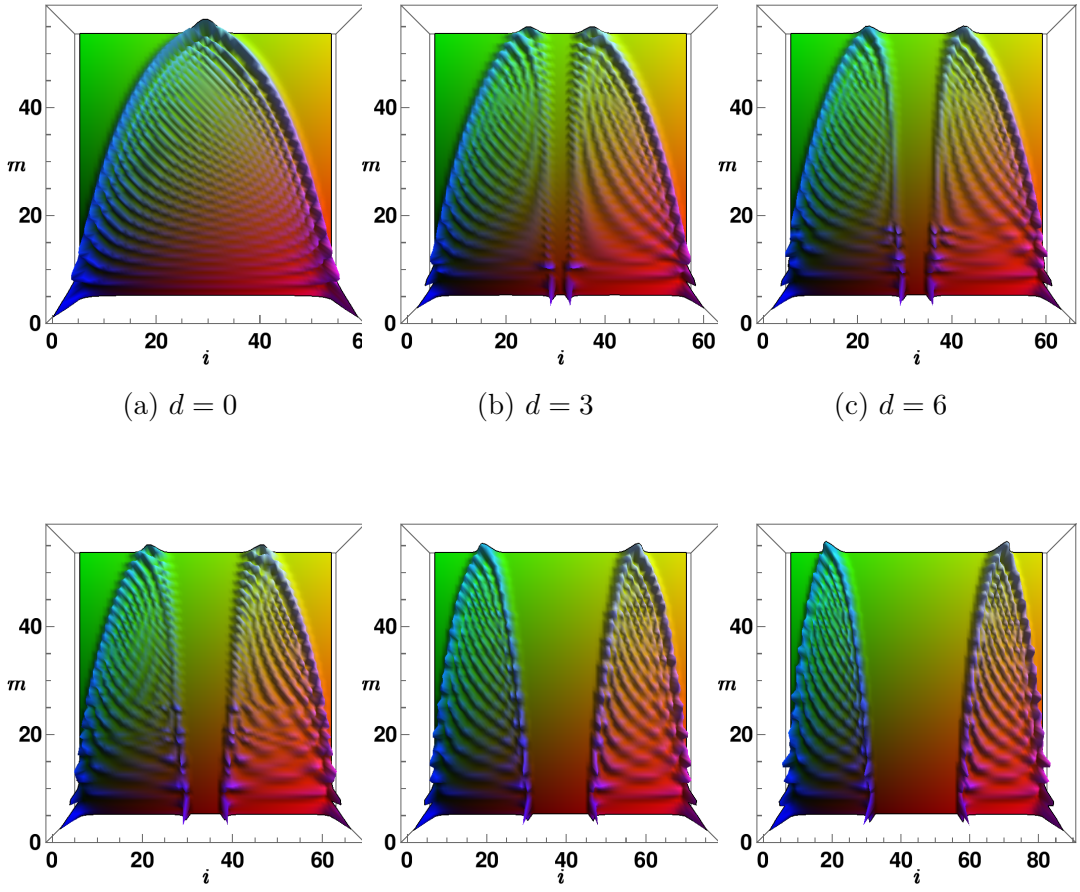

(a) $d = 0$ (b) $d = 3$ (c) $d = 6$

(d) $d = 9$ (e) $d = 18$ (f) $d = 30$

Figure 4.4: Mode participation function of a subsystem A composed by two disjoint intervals (each of length $\ell_A = N_A = 30$ in a chain of $L = N = 300$). The different subfigures represent six different distances d between the two intervals. $\mathcal{P}^{(m)}(i)$ exhibits negative values (see Fig. 4.5 (a)), differently from the well behaved case of one interval. For small distances d, the profile of one interval feels the presence of the other, while for far enough distances each profile becomes symmetric, as if the other interval were not present.

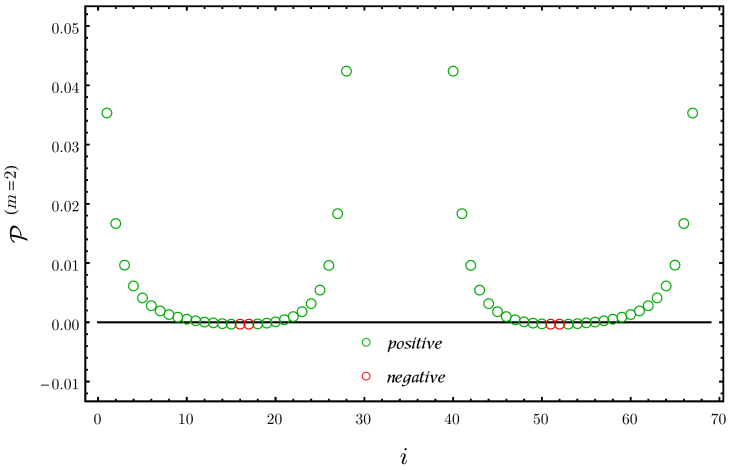

(a) $\mathcal{P}^{(m=2)}(i)$, $d = 9$

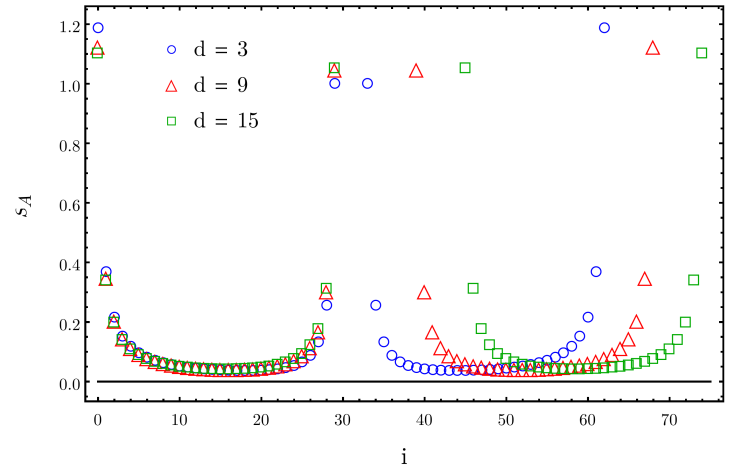

(b) $\varepsilon(i)$, $d = 3, 9, 15$

Figure 4.5: (a) it is plotted the mode $m = 2$ participation function of entanglement entropy of two equal disjoint intervals of length $N_A = 30$ and separation $d = 9$ in a chain $N = 300$. The red circles correspond to negative values of $\mathcal{P}^{(m=2)}(i)$. In (b) it is shown the entanglement entropy contour for disjoint $(d = 3, 9, 15)$ intervals.

since the mode participation function gains a minus sign compared to the one for fermions (see Eq. (22) of [202]).

In this section we will list our preliminary results about the entanglement entropy contour for bosons. First, we numerically check (in our $1+1$ harmonic chain) that for configurations in which A is composed by just one interval, the mode participation function (and therefore the contour) is positive. On the contrary, when A is made by two disjoint intervals may be that the mode participation function shows some negative values. However, the contour turns out to be always positive in all the numerical examples of disjoint intervals we considered. In this section we will discuss in more details the case of the two intervals, which is not present in the literature and prove the positivity of the entanglement entropy contour for bosons. Let us first start with some preliminary steps.

The entanglement entropy (4.25) can be written in the following form which is more suitable for our discussion

$$S_A = \mathrm{Tr}(f(\sqrt{\mathbb{Q}_A\,\mathbb{P}_A})), \quad i = 1, \dots \ell_A, \tag{4.48}$$

where

$$f(x) = (x+1/2)\log(x+1/2) - (x-1/2)\log(x-1/2). \tag{4.49}$$

The contour can be obtained by inserting in the trace a projector on the i-th site, $M^{(i)} = |i\rangle\langle i|$. Thus, we have

$$s_A(i) = \mathrm{Tr}(M^{(i)} f(\sqrt{\mathbb{Q}_A\,\mathbb{P}_A})), \quad i = 1, \dots, N_A. \tag{4.50}$$

To see this, let us recall that the matrices $\sqrt{\mathbb{Q}_A\,\mathbb{P}_A}$ and $\sqrt{\mathbb{P}_A\,\mathbb{Q}_A}$ can be diagonalized as

$$V^{-1}\sqrt{\mathbb{Q}_A\,\mathbb{P}_A}V = D\,, \quad U^{-1}\sqrt{\mathbb{P}_A\,\mathbb{Q}_A}U = D\,, \tag{4.51}$$

where V and U are the real invertible matrices introduce in Eq. (4.30). We recall that they are not orthogonal because $\sqrt{\mathbb{Q}_A\,\mathbb{P}_A}$ is not symmetric. The matrices V and U are related by $V^T = U^{-1}$. D is the diagonal matrix with the $\lambda_k \geq 1/2$ on its main diagonal. Since f in (4.49) is analytic, it can be written as an infinite sum of powers and therefore

$$f(\sqrt{\mathbb{Q}_A\,\mathbb{P}_A}) = f(VDV^{-1}) = Vf(D)V^{-1}\,. \tag{4.52}$$

Now, $f(D)$ is diagonal with the diagonal elements the $S(\lambda_k) = f(\lambda_k)$'s. The r.h.s. of (4.50) becomes

$$\begin{aligned}\mathrm{Tr}(M^{(i)} f(\sqrt{\mathbb{Q}_A\,\mathbb{P}_A})) &= \mathrm{Tr}(M^{(i)} V f(D) U^T) = \sum_{jlk} M^{(i)}_{jl} V_{lk} f(\lambda_k) U_{jk} \\ &= \sum_{jlk} \delta_{ij}\delta_{il} v^{(k)}_l u^{(k)}_j S(\lambda_k) = \sum_k v^{(k)}_i u^{(k)}_i S(\lambda_k) = \sum_k \mathcal{P}^k(i) S(\lambda_k),\end{aligned} \tag{4.53}$$

where we used that $\mathcal{P}^k(i) = v_i^{(k)} u_i^{(k)}$ is the mode participation function defined in (4.43). In Fig. 4.4, plot the participation function of a subsystem A composed by two disjoint intervals (each of length $\ell_A = N_A = 30$ in a chain of $L = N = 300$). The different subfigures represent different distances d between the two intervals. For close intervals (small d) the profile of one interval feels the presence of the other, while for far enough distances each profile become symmetric, as if the other interval was not present. As described at the beginning of this section, in general the mode participation function for bosons might be negative. Numerically we checked different configurations for the $1+1$ harmonic chain: single intervals and disjoint intervals. In the former case, we do not find any negative value for the mode participation function, while in the latter some negative values emerge. However, while the mode participation function is sometimes negative (see Fig. 4.5 (a)), the contour obtained is numerically always positive (Fig. 4.5 (b)). This can be prove also in a rigorous way, as follows.

The eigenvalues of $\sqrt{\mathbb{Q}_A \mathbb{P}_A}$ are $\lambda_k \geq 1/2$ and $f(x) \geq 0$ for $x \geq 0$. Therefore, $f(\sqrt{\mathbb{Q}_A \mathbb{P}_A}) \geq 0$. Since $M^{(i)}$ is a projector, it is symmetric and positive definite, and therefore $M^{(i)} \sqrt{\mathbb{Q}_A \mathbb{P}_A} M^{(i)}$ is positive definite too and have positive trace. Finally, since $(M^{(i)})^2 = M^{(i)}$, we have $\mathrm{Tr}(M^{(i)} f(\sqrt{\mathbb{Q}_A \mathbb{P}_A})) = \mathrm{Tr}(M^{(i)} f(\sqrt{\mathbb{Q}_A \mathbb{P}_A}) M^{(i)}) \geq 0$. Thus, we conclude that the entanglement entropy contour is always positive.

The same proof holds also in the case of the contour for Rényi entropies, which is defined as follows

$$s_A^{(n)}(i) = \sum_{m \in A_k} \mathcal{P}^m(i) S_A^{(n)}(\lambda_m)\,, \quad S_A^{(n)}(\lambda) = \frac{1}{n-1} \log \left[\left(\lambda + \frac{1}{2}\right)^n - \left(\lambda - \frac{1}{2}\right)^n \right], \tag{4.54}$$

being that the mode participation function $\mathcal{P}^m(i)$ is the same as for the entanglement entropy and the function $S_A^{(n)}(x) \geq 0$ for $x \geq 0$.

4.4 Negativity contour: an ansatz

In this section we try to implement the same approach used for the entanglement entropy contour in order to find a definition of the contour for the logarithmic negativity. Let us consider a chain of N bosonic oscillators in the ground state, which is a pure Gaussian state. We now take a set of $N_A \leq N$ sites and bipartite it in two subsets N_{A_1} and N_{A_2}, i.e. $N_{A_1} + N_{A_2} = N_A$. In this framework, the logarithmic negativity ca be written as

$$\mathcal{E} = \sum_{k=1}^{N_A} \mathcal{E}(\nu_k), \qquad \mathcal{E}(\nu_k) = -\log \left[\left| \nu_k + \frac{1}{2} \right| - \left| \nu_k - \frac{1}{2} \right| \right] = \log \max \left[1, \frac{1}{2\nu_k} \right], \tag{4.55}$$

where the $\nu_k > 0$ are the symplectic eigenvalues of $\sqrt{\mathbb{Q}_A \tilde{\mathbb{P}}_A}$, being $\tilde{\mathbb{P}}_A \equiv \mathbb{R}_{A_2} \mathbb{P}_A \mathbb{R}_{A_2}$, where $\mathbb{R}_{A_2}$ is the matrix introduced in Eq.(3.12).

Inspired by the procedure described above for the mode participation function, let us introduce the following mode participation function for the negativity

$$\tilde{\mathcal{P}}^m(i) = \tilde{u}_i^{(m)} \tilde{v}_i^{(m)} \,, \tag{4.56}$$

where now $\tilde{v}_i^{(m)}$ and $\tilde{u}_i^{(m)}$ are the eigenvectors of $\tilde{\mathbb{P}}_A \mathbb{Q}_A$ and $\mathbb{Q}_A \tilde{\mathbb{P}}_A$, respectively. The contour of the negativity, similarly to the entanglement entropy case, can be defined as

$$\varepsilon(i) = \sum_{m=1}^{N_A} \tilde{\mathcal{P}}^m(i) \mathcal{E}(\nu_m) \,. \tag{4.57}$$

Being that $\sum_{i \in A} \tilde{\mathcal{P}}^m(i) = 1$, we recover the first equation of (4.55), as expected.

4.4.1 Negativity contour in the pure case

Let us consider the case of a pure state $\rho = |\Psi\rangle \langle\Psi|$ acting on a bipartite Hilbert space, where $B = 0$ ($A = A_1 \cup A_2$, $S_A = 0$). In this case we remind that the relation between logarithmic negativity and 1/2-Rényi entropy

$$\mathcal{E} = S_{A_1}^{(1/2)} = S_{A_2}^{(1/2)} \tag{4.58}$$

holds and the moments of the partial transpose are related to the Rényi entropies as follows [95, 96]

$$\mathrm{Tr}\left(\rho^{T_2}\right)^n = \begin{cases} \mathrm{Tr}\, \rho_{A_2}^{n_o} & \text{odd } n = n_o \,, \\ \left(\mathrm{Tr}\, \rho_{A_2}^{n_e/2}\right)^2 & \text{even } n = n_e \,. \end{cases} \tag{4.59}$$

It is important to underline that this result depends on the parity of n. From this relation, by employing that $S_{A_1}^{(n)} = S_{A_2}^{(n)}$ for pure state, we obtain

$$\mathcal{E}^{(n_o)} = \left(\frac{1 - n_o}{2}\right) \left(S_{A_1}^{(n_o)} + S_{A_2}^{(n_o)}\right) \tag{4.60}$$

$$\mathcal{E}^{(n_e)} = \left(1 - \frac{n_e}{2}\right) \left(S_{A_1}^{(n_e/2)} + S_{A_2}^{(n_e/2)}\right) \,, \tag{4.61}$$

where $S_{A_k}^{(n)}$ has support only in A_k, $k = 1, 2$. Suppose now that $N_{A_1} \leq N_{A_2}$, it is useful for our discussion remind that, being in a pure state, the symplectic eigenvalues of D_{A_2} are the same of D_{A_1} plus a number $N_{A_2} - N_{A_1}$ of 1/2, which do not contribute. For the $N_{A_2} + N_{A_1}$ symplectic eigenvalues of the partial transpose, we can divide them in those less then 1/2, denoted by $\nu_k^<$, those greater then 1/2, denoted by $\nu_k^>$, and those equal to 1/2, namely $\nu_{1/2}$. The latter are exactly $N_{A_2} - N_{A_1}$ and do not contribute

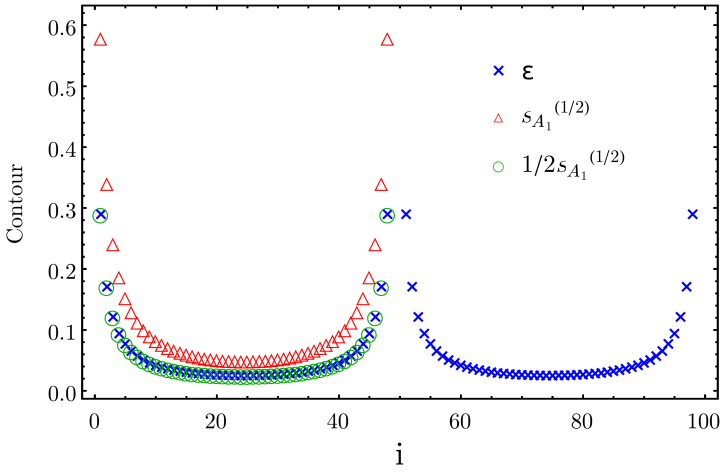

(a) equal intervals

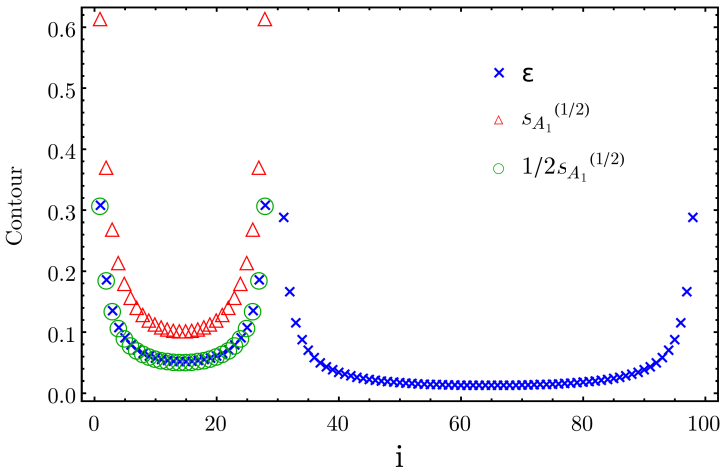

(b) different intervals

Figure 4.6: In this figure, Eq. (4.69) is plotted with $n_e = 1$. We can see that, when $B = 0$, the well known relation between negativity and Rényi entropy $S^{(1/2)}$ holds site by site.

to the moments of the partial transpose. This suggests the existence of a relation between the ν's and the λ's different from 1/2, or in an equivalent way between the eigenvalues of the partial transpose and the partial density matrix (different from 0). In other words the negativity spectrum is not independent from the entanglement spectrum [208]. Starting from Eq. (4.61), we can write

$$\sum_{k=1}^{N_A} \log\left[\left(\nu_k+\frac{1}{2}\right)^{n_e}-\left(\nu_k-\frac{1}{2}\right)^{n_e}\right] = 2\sum_{k=1}^{N_{A_1}} \log\left[\left(\lambda_k+\frac{1}{2}\right)^{n_e}-\left(\lambda_k-\frac{1}{2}\right)^{n_e}\right], \tag{4.62}$$

from which

$$\left[\left(\nu_k^{<}+\frac{1}{2}\right)^{n_e}-\left(\nu_k^{<}-\frac{1}{2}\right)^{n_e}\right]\left[\left(\nu_k^{>}+\frac{1}{2}\right)^{n_e}-\left(\nu_k^{>}-\frac{1}{2}\right)^{n_e}\right] \tag{4.63}$$

$$= \left[\left(\lambda_k+\frac{1}{2}\right)^{n_e}-\left(\lambda_k-\frac{1}{2}\right)^{n_e}\right]^2, \tag{4.64}$$

and after some algebra it is easy to obtain the following relations

$$\nu_k^{<} = \lambda_k - \sqrt{\lambda_k^2-\frac{1}{4}} \tag{4.65}$$

$$\nu_k^{>} = \lambda_k + \sqrt{\lambda_k^2-\frac{1}{4}}\,. \tag{4.66}$$

These equations are nothing else that Eq. (11) of [208] written in terms of symplectic eigenvalues. Eq. (11) of [208] was found from Eq. (4.59) using the Schmidt decomposition of an arbitrary bipartite pure state.

We recall that the contour for Rényi entropies was defined in Eq.(4.54) and the one for the moments of the partial transpose is

$$\varepsilon^{(n)}(i) = \sum_{m\in A} \tilde{\mathcal{P}}^m(i)\mathcal{E}^{(n)}(\nu_m)\,, \quad \mathcal{E}^{(n)}(\nu) = -\log\left[\left(\nu+\frac{1}{2}\right)^{n}-\left(\nu-\frac{1}{2}\right)^{n}\right]. \tag{4.67}$$

As it is shown in Fig. 4.6, the negativity contour, when restricted to sites in region A_k, $k=1,2$, coincides site by site with half of the contour of the 1/2-Rényi entropy in region A_k. This means that Eq. (4.58) is true also locally, namely site by site

$$\varepsilon(i) = \frac{1}{2}\left(\delta_{i\in A_1}\, s_{A_1}(i) + \delta_{i\in A_2}\, s_{A_2}(i)\right), \tag{4.68}$$

where $\delta_{i\in A_k}=1$ if $i\in A_k$, zero otherwise. We also checked the same relation for the contour of the moments. This allows us to write

$$\varepsilon^{(n_e)}(i) = \left(1-\frac{n_e}{2}\right)\left(\delta_{i\in A_1}\, s_{A_1}^{(n_e/2)}(i) + \delta_{i\in A_2}\, s_{A_2}^{(n_e/2)}(i)\right), \quad \forall i\in A \tag{4.69}$$

$$\varepsilon^{(n_o)}(i) = \left(\frac{1-n_o}{2}\right)\left(\delta_{i\in A_1}\, s_{A_1}^{(n_o)}(i) + \delta_{i\in A_2}\, s_{A_2}^{(n_o)}(i)\right), \quad \forall i\in A\,. \tag{4.70}$$

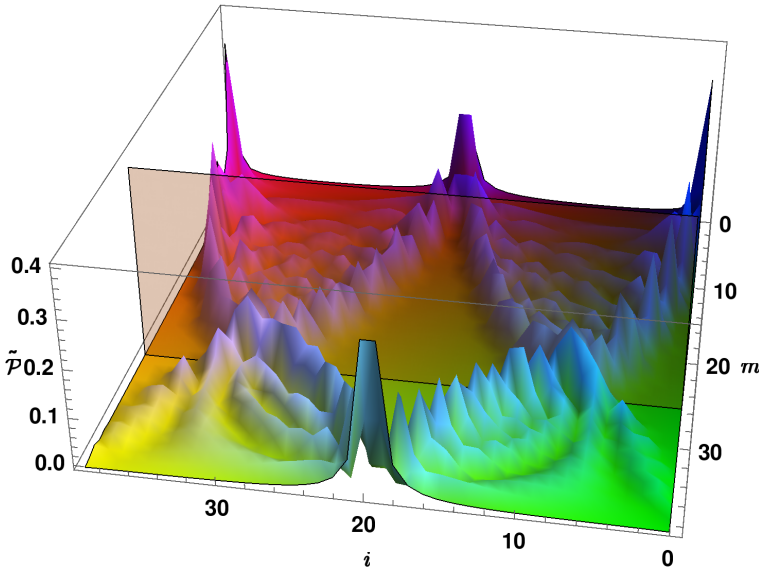

Figure 4.7: $\tilde{\mathcal{P}}^m(i)$ versus sites and modes for the negativity of two equal and adjacent intervals ($N_{A_1} = N_{A_2} = 20$, chain of $N = 200$ sites). The subregion B that was traced out is not plotted and the transparent plane separates modes corresponding to symplectic eigenvalues $\nu_m < 1/2$ (front of the plot), which contributes to the negativity, from modes corresponding to $\nu_m > 1/2$ (back of the plot), which do not contribute in Eq. (4.55). The main contribution to negativity comes form the sites which are close to the boundary between A_1 and A_2, while sites close to B do not partecipate. For what concerns the moments of the partial transpose, where also the eigenvalues $\nu_m > 1/2$ enter into the game, one can observe that they receive contributions also from the back part of the plot. That is the reason why they have with B an area law (see also [164])

4.4.2 Negative values in the logarithmic negativity contour

One can try to prove the positivity of the negativity contour following the same logic we used for the entanglement case. However, this approach fails. The starting point for the proof of the positivity of the entanglement contour for bosons was Eq. (4.50). One can write the contour for negativity, Eq. (4.57), in the same form of Eq. (4.50) for the entanglement contour and obtain

$$\varepsilon(i) = \mathrm{Tr}\left(M^{(i)} g\left(\sqrt{\mathbb{Q}_A\, \tilde{\mathbb{P}}_A}\right)\right), \tag{4.71}$$

where we recall that $M^{(i)} = |i\rangle\langle i|$ is the projector on the i-th site. Now

$$g(x) = -\log\left[\left|x+\frac{1}{2}\right| - \left|x-\frac{1}{2}\right|\right] . \tag{4.72}$$

This function is not analytic (due to the presence of the absolute value) and therefore we cannot prove that the negativity contour is positive by the straightforward generalization of the proof discussed in §4.3.2 for the entanglement entropy contour for bosons.

In Fig. 4.7 it is shown $\tilde{\mathcal{P}}^m(i)$ versus sites and modes for the negativity of two equal and adjacent intervals ($N_{A_1} = N_{A_2} = 20$, chain of $N = 200$ sites). The subregion B that was traced out is not plotted and the transparent plane separates modes corresponding to symplectic eigenvalues $\nu_m < 1/2$ (front of the plot), which contribute to the negativity, from modes corresponding to $\nu_m > 1/2$ (back of the plot), which do not contribute in Eq. (4.55). One can easily see that the main contribution to negativity comes form the sites which are close to the boundary between A_1 and A_2, while sites close to B provide a very small relative contribution. For what concerns the moments of the partial transpose, where also the eigenvalues $\nu_m > 1/2$ enter into the game, one can observe that they receive contributions also from the back part of the plot. That is the reason why they exhibit an area law behavior with B (see also [164]).

In Fig. 4.8 we plot the mode participation function $\tilde{\mathcal{P}}^m(i)$ for two disjoint intervals with increasing distance between them. It is natural to compare this figure with Fig. 4.4, where for $d = 30$ the profiles of the two intervals were completely symmetric, as if the presence of one interval does not influence the profile of the other. Now, for what concerns $\tilde{\mathcal{P}}^m(i)$ relative to the modes corresponding to $\nu_m > 1/2$ (lower part) it seems as each profile is not affected by the presence of the other, while for $\tilde{\mathcal{P}}^m(i)$ relative to $\nu_m < 1/2$ (upper part) the profile of one interval still feels the presence of the other. Numerically, using the harmonic chain in $1+1$-dimensions we tested several configurations where the subregions A_1 and A_2 were adjacent or disjoint intervals. The mode participation function $\tilde{\mathcal{P}}^m(i)$ shows negative values, both for adjacent and disjoint intervals. This miss fact was also present in $\mathcal{P}^m(i)$ for disjoint intervals (see Fig. 4.5 (a)), but we proved that the entanglement contour $s_A(i) = \sum_m \mathcal{P}^m(i) S(\lambda_m)$ is positive (also for Rényi entropies), as shown also numerically in Fig. 4.5 (b). Moreover, we numerically had evidence that not only the mode participation function but also the contour for negativity shows up negative values, in particular close to the boundary with the traced out region B, both for adjacet (see Fig. 4.9 (a)) and disjoint intervals (see Fig. 4.9 (b)).

In Fig. 4.9 (a), it is plotted the contour for the negativity between two equal adjacent intervals of length $N_A = N_B = 40$ in a chain of $N = 400$ oscillators. As expected, the contour has a peak close to the boundary shared by the two intervals

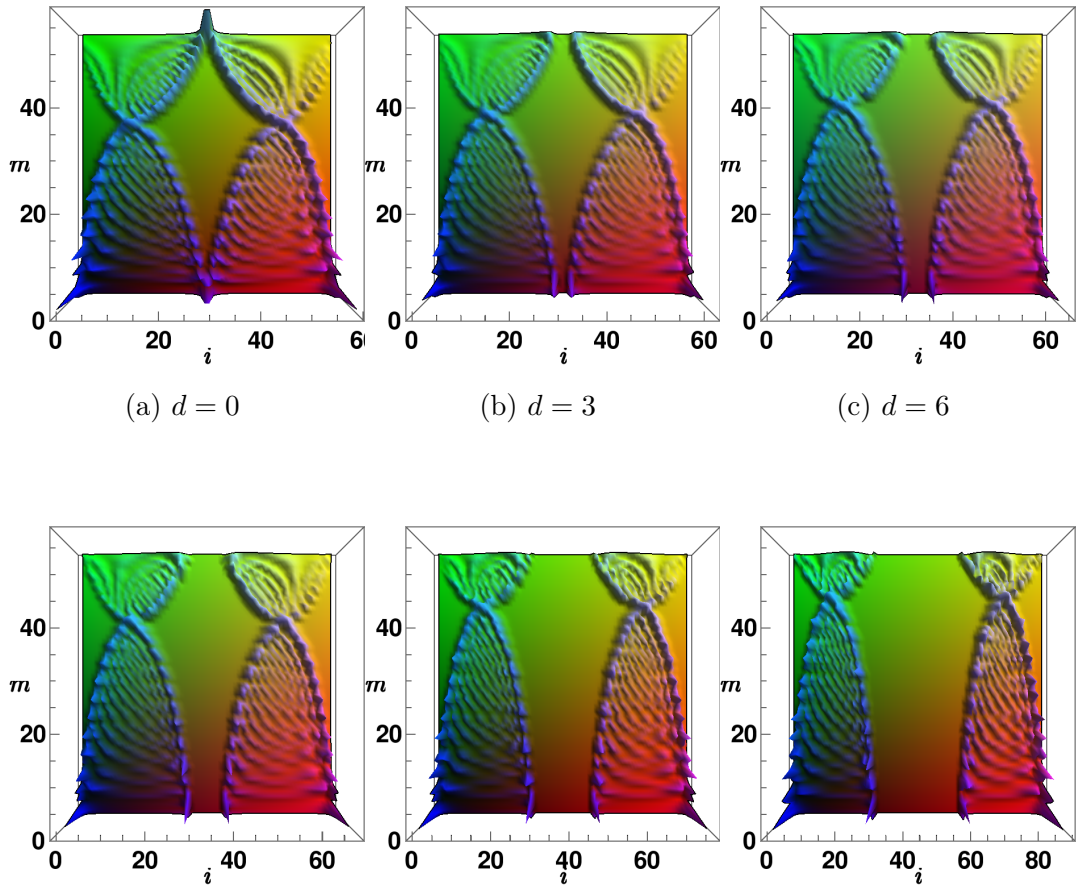

(a) $d = 0$ (b) $d = 3$ (c) $d = 6$

(d) $d = 9$ (e) $d = 18$ (f) $d = 30$

Figure 4.8: In this three figures we are considering the participation function for the negativity of a subsystem A composed by two disjoint intervals (each of length $\ell_A = N_A = 30$ in a chain of $L = N = 300$). It is natural to compare this figure with Fig. 4.4, where for $d = 30$ the profiles of the two intervals were completely symmetric, as if the presence of one interval does not influence the profile of the other.

and it then decreases while reaching the opposite endpoints. However, in red are underlined the undesired negative values. The same happens also for the case of disjoint intervals, as shown in red in Fig. 4.9 (b).

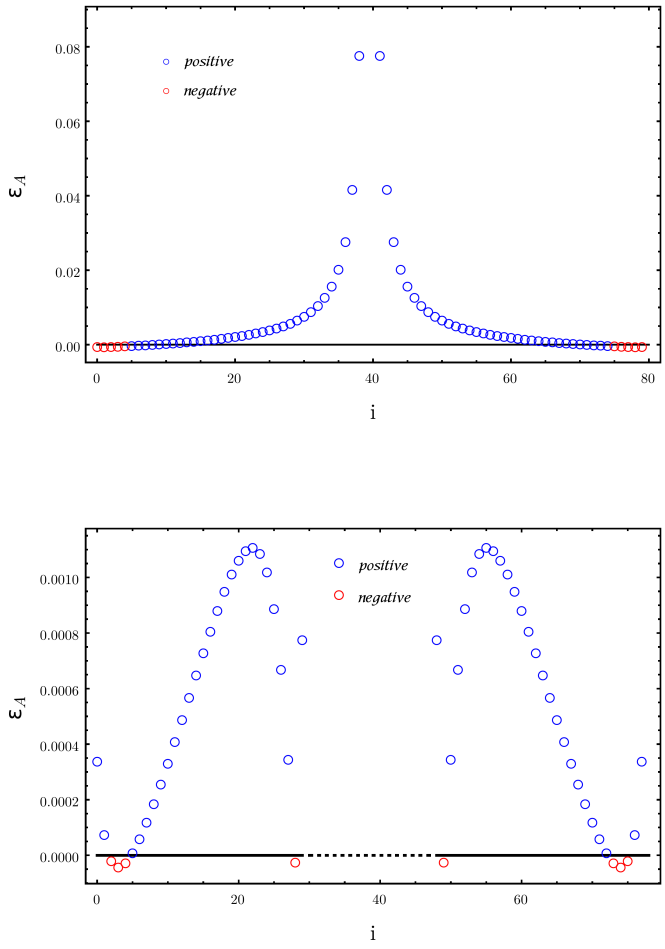

Figure 4.9: In (a) it is plotted the contour for the negativity between two equal adjacent intervals of length $N_A = N_B = 40$ in a chain of $N = 400$ oscillators. The contour has a peak close to the boundary shared by the two intervals and it decreases while reaching B. Negative values occur for sites close to B region. The same miss fact happens in (b), where the intervals are disjoint.

In Fig. 4.10 we consider the case of adjacent intervals, focussing on the region close to B where the logarithmic negativity contour becomes negative. In the scaling limit the negative values do not disappear.

This miss fact invalidates the interpretation of the contour [201], which was

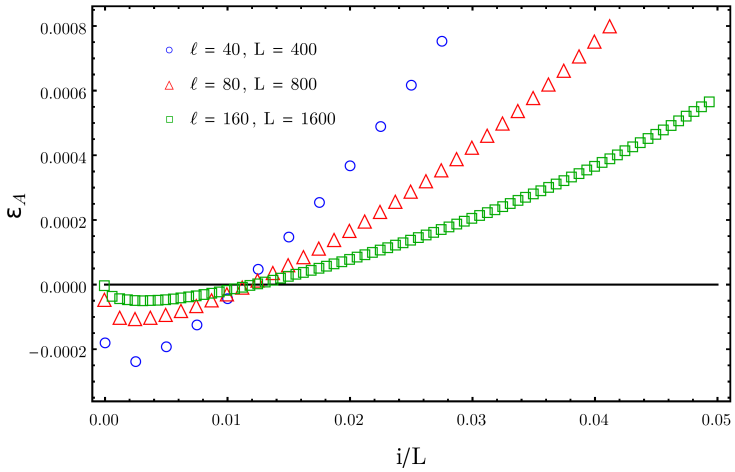

Figure 4.10: The scaling limit of the contour for the negativity between two equal adjacent intervals for the region where the contour becomes negative. The length of the intervals is 1/10 the length of the whole system.

thought to be a quantifier of how much the degrees of freedom in the ith site contribute to the entanglement between the two regions A_1 and A_2.

Conclusions

Entanglement negativity has drawn a lot of attention in the last years as a very useful tool to quantify entanglement between separated regions or in general mixed states of quantum many-body systems. The entanglement entropy computed for disjoint regions only measures the amount of entanglement between the union of the intervals with the rest of the system. If one needs the entanglement shared by the disjoint regions, which are in general left in a mixed state after the rest is traced out, the entanglement entropy is no longer useful, and other measures must be used. The definition of the negativity makes it a computable measure of entanglement [31] also in many-body systems, and we saw that it can be computed in QFT, at least in principle, using the replica trick [95, 96]. However, the analytic continuations leading to analytic expressions for the entanglement entropy and the logarithmic negativity of disjoint regions can be very difficult to perform, even for simple CFTs.

In Chap. 2 we studied this problem numerically for the CFTs given by the free massless boson (compactified or in the decompactification regime) or by the Ising model, where $\mathrm{Tr}\,\rho_A^n$ for a generic number of disjoint intervals [70, 71, 94] and $\mathrm{Tr}(\rho_{A_1\cup A_2}^{T_2})^n$ are known analytically [95–98].The numerical extrapolations have been performed through a method based on rational interpolations, which has been first employed in this context by [171]. Its reliability has been checked by reproducing the existing results found from the corresponding lattice models through various techniques like exact diagonalizations [63, 94] and Tree Tensor Networks [64]. In our analysis, we observed that for the entanglement entropy one finds the same curve through different extrapolations already with small values of the degrees p and q of the polynomials occurring in the numerator and in the denominator respectively of the rational interpolation. Instead, for the logarithmic negativity higher values of p and q are needed for the regime of distant intervals, where it falls off faster than any power. Extrapolations having higher values of q are more efficient in providing the expected result, but they can show some spurious behaviour in some parts of the domain. Our numerical analysis has been limited both by our computational resources (in the evaluation of the Riemann theta functions for large matrices) and by the features of the model (e.g.

for the logarithmic negativity of distant intervals). These obstacles prevented us to treat some interesting cases like the logarithmic negativity of two disjoint intervals for the compact boson and for the Ising model because high values of n are needed to get convincing extrapolations. We remark that lattice results for $\mathcal{E}(x)$ have been found in [97] for the Ising model through Tree Tensor Networks, while for the compact boson they are not available in the literature (see [122] for $\widetilde{R}_3$ obtained through Quantum Monte Carlo).

When singularities in n occur (see e.g. [65, 209, 210]), the numerical method adopted in Chap. 2 is not expected to be stable and to reproduce the correct analytical continuation. However, a more detailed analysis of the behaviour of the method in these cases would be interesting and should be addressed in the future. As for the one dimensional systems that have been considered, given the good agreement with the lattice results, a posteriori we expect that there are no singularities in the ranges of n that have been explored.

The rational interpolation method has been also employed to address some cases whose corresponding lattice results are not available in the literature (e.g. the $U(1)$ gauge theory in $2+1$ dimensions has been studied in [171] and the case of three disjoint intervals for the Ising model in §2.3). Thus, it is a useful tool that could be used in future studies to find numerically the entanglement entropy and the logarithmic negativity of disjoint regions (or for single regions whenever the analytic continuation is difficult to obtain) for other interesting situations like e.g. for CFTs in higher dimensions [87, 88, 90, 92] and in the context of the holographic correspondence [77, 78, 80–86], which has interesting connections with the MERA tensor network technique [149, 211–217].

In Chap. 3 we have investigated the logarithmic negativity $\mathcal{E}$ and the moments of the partial transpose for adjacent domains A_1 and A_2 in the ground state of a two dimensional harmonic square lattice with nearest neighbour spring-like interaction. The regime of massless oscillators in the thermodynamic limit has been considered.

By exploring various configurations of adjacent domains, we have shown that, at leading order for large domains, the logarithmic negativity and the quantity $\mathcal{E}_n$ introduced in (1.77) satisfy an area law in terms of the length of the shared curve $\partial A_1 \cap \partial A_2$, suggesting a relation between the coefficient of the area law term in these quantities and the coefficient of the area law term in the Rényi entropies.

A subleading universal logarithmic term occurs in $\mathcal{E}$ and $\mathcal{E}_n$ whenever the shared curve contains vertices, being its endpoints included among them. The values of the corner function of $\mathcal{E}$ have been obtained for some pairs of angles. For the vertices of $\partial A_1 \cap \partial A_2$ corresponding to pairs of explementary angles, we have proposed that the corner function of $\mathcal{E}_n$ is related to the corner function entering in the Rényi entropies [147]. This relation implies that the corner function of $\mathcal{E}$ for this kind of vertices coincides with the corner function of the Rényi entropy of order $1/2$. This statement

has been supported by numerical evidences.

As for the vertices of the curve $\partial A_1 \cap \partial A_2$ corresponding to a tripartition of the angle of 2π, their contribution to the logarithmic term in $\mathcal{E}$ and $\mathcal{E}_n$ is characterized by a new corner function which depends on two independent angular variables. The numerical values of this corner function for $\mathcal{E}$ have been given in (3.30) for some pair of angles (see also Fig. 3.7).

In this context, It would be interesting to provide further checks of (3.29). In particular, the analytic continuation to $n = 1/2$ of the corner function found by Casini and Huerta [147] should be performed. More importantly, a method should be found to compute analytically the corner functions $b(\theta, \gamma)$ and $b_n(\theta, \gamma)$ for the vertices partitioning the angle of 2π in three parts. By analogy with the results of [154, 157] obtained for the corner function of S_A, it could be interesting to study the corner function $b(\theta, \theta)$ for equal angles as $\theta \to \pi^-$. In order to extract reliable numerical results for the logarithmic term of $\mathcal{E}_n$ from the fit of the lattice data, the unusual corrections to the scaling must be studied, extending the analysis done by Cardy and Calabrese [140] in $1 + 1$ dimensions. Finally, it is worth studying the corner contributions to $\mathcal{E}$ and $\mathcal{E}_n$ for other models, both on the lattice and in the continuum. In general, the study of negativity in higher dimensions, where few results are available [124, 125], still remains an open problem. In particular not much has been investigated in higher dimensional QFT [218], unlike for the entanglement entropy, the Rényi entropies and the mutual information where some important results have been found [87, 92, 93, 219].

In Chap. 4 we discussed some preliminary results about the spatial distribution of entanglement entropy, which was first studied in [179, 201, 202], and logarithmic negativity. The concept of contour may be a very useful tool in the understanding of the corresponding entanglement measure. However, its definition and the related mode participation function have to be better understood. In the case of entanglement entropy of a free bosonic theory, we showed that negative values appear in the mode participation function for disjoint intervals. Nevertheless, the entanglement contour is always positive. For logarithmic negativity, the situation gets worse. The mode participation function that we have introduced by a naive generalization of the one occurring for the entanglement entropy still have negatives values, but now also the contour presents them in particular close to the boundary between A and B. Presumably in the case of negativity a new definition is necessary for the contour and only a more detailed analysis may give the answer.

Finally, let us mention that a holographic description of negativity is still lacking, even if some steps have been made in that direction [132, 133]. A deeper analysis of this issue could lead to interesting results on the connections between quantum information and quantum gravity.

Acknowledgements

Siccome una delle funzioni della memoria è il dimenticare, spero che questa non si attivi proprio ora. Cercherò di ringraziare le persone che hanno avuto un significato in questa esperienza a Trieste.

Ringrazio sia il settore di Particle Physics, nel quale sono novello entrato in SISSA, sia quello che mi ha accolto successivamente, Statistical Physics. Da entrambi ho cercato di imparare qualcosa, senza dover cambiare piano. Ringrazio Erik, per due ragioni. La prima è legata al fatto che è stato il mio supervisor da cui ho cercato di imparare l'arte della ricerca. L'altra è il fatto di avermi, forse all'inizio forzatamente, introdotto alle simulazioni numeriche e la programmazione. Solo ora ho scoperto che questo mi ha aperto nuove porte ed avventure.

Un ringraziamento particolare va ad Andrea, amico dai tempi di Padova e collaboratore scientifico. Mi ha insegnato tanto e con altrettanta pazienza. Ho imparato con lui i primi codici ed eseguito con lui infiniti check. Ringrazio anche Piermarco, leading-expert triestino per Evolver, che mi è stato di grande aiuto.

In SISSA ho svolto praticamente tutte le attività consentite e di conseguenza conosciuto molte persone speciali e condiviso con loro bellissimi momenti. Nei pochi minuti prima della stampa della tesi, fatico a ricordarle e citarle tutte.

C'è sicuramente Silvia, amica rossa, intelligente e complice. Rappresentanti insieme per tre anni. Lunghe sedute in Senato, due Direttori, vicende occulte. Insieme a lei ho pensato Shiriki e con questo concluso il master MCA, le serate a Paluzza e la soprattutto la California.

C'è Matteo, grande amico da tempo con il quale ci siamo un po'sostenuti a vicenda. L'ufficio 414 era per me la quotidianità quando era in SISSA. I soprannomi in mensa, le confidenze ed i sogni per il futuro. Lui però è friulano, enigmatico, saggio e di poche parole. Tutto questo spesso collide con la mia personalità, ma abbiamo imparato a convivere. Belli i tempi di Padova, quando eravamo ancora amici. Sempre dell'ufficio 414, cito Nicola e Guglielemo complici in molte occasioni e pause caffè. Ringrazio anche le bresciane Cristina ed Elena, poi Clara e le ragazze di neuroscienze con cui ho condiviso serate e feste SISSA.

Poi c'è Ivan, una persona speciale e generosa. Un grande. Come dice Serguey, una forza della natura. E'la persona con cui ho passato più tempo in questi anni. Tante serate con lui, dal periodo del Costa alle vacanze sul Garda. Le domeniche in SISSA, infinite. Le domenica in SISSA in cui poi ci si guardava e si scappava a volare o si prendeva Giulia e si andava all'avventura. La collezione di bottiglie che ha reso famoso il nostro ufficio e tante altre cose.

C'è da menzionare anche Giulia, altrimenti si offende. La più bionda ed elegante di Trieste è stata preziosa in questi anni. Conosciuta per un imbroglio, si è rivelata una sorpresa. Guai se non ti ricordi quella volta alla fontana. Giulia, abbiamo ancora un anno a Trieste quindi non piangere che c'è tempo per scrivere ancora qualche riga. Un grazie anche a Linda e Jasmine.

Ringrazio anche Gianni, con cui ho condiviso momenti difficili e frustrazione; passeggiate, illy e cocktail in locali di un certo livello. Ringrazio Arseni che ha sentito i miei lamenti per giorni, ma ha sempre detto le parole giuste (nel suo italiano perfetto ovviamente) e sopportato la coppia De Nobili - Girardi nello stesso ufficio. C'è anche Paola, un appoggio soprattutto nell'ultimo difficile periodo. Solare, entusiasta e divertente da stuzzicare. Bellissimo in Giappone. Prima di conoscermi era una ragazza semplice, ora solo sushi, Chanel e taxi. Hai ancor tempo per peggiorare. Ringrazio anche Alessio, riscoperto recentemente e con cui ci siamo sostenuti a vicenda in questi ultimi due strani mesi. Per Aurora vale lo stesso, un grazie anche a te. Un grazie anche a tutti gli amici con cui ho iniziato questa esperienza: Mauro, Bruno, Giovanni ed Elena. Poi c'è Stefano, coinquilino speciale, soprano e nemico del narcisismo e portatore della filosofia Enjoyce.

Un ringraziamento speciale, che esce dai confini di Trieste, va ai miei genitori e la nonna Lida. La fretta con cui sto scrivendo queste ultime righe non mi permette di esprimere esaustivamente il loro aiuto, sia economico che morale, durante l'arco di tutti questi anni. La Mamma ha espresso tutte le sue forze e sacrifici per sostenermi. Di più era impossibile. Il Papà mi ha dato utili consigli e permesso di realizzare quella che è forse la mia più grande passione e sfogo insostituibile in questi anni: stare in aria.

Ringrazio Simona, Olga, Enrico e tutto lo staff di SISSA for School. Esperienza fantastica che consiglio a tutti gli studenti della scuola. Ringrazio Sofia, mia compagna di palcoscenico nell'ultima parte di questa avventura.

In ultimo ringrazio la SISSA come istituzione. E'stata fonte di gioie e dolori, un posto incredibile, come Trieste. Ho imparato molto grazie a tutte le esperienze che mi ha consentito di fare, anche quelle extra-scientifiche. Continuerò anche quest'anno a imparare da lei, sempre cose nuove, sempre cose diverse. Ringrazio anche il mio ufficio, proprio vicino al terrazzo. Bastava un pizzico di fantasia per sentirsi in volo.

Lo so, sto dimenticando molte persone. Anche ora, come sempre, è una corsa. La Scienza ha bisogno di tempo e la fretta se la sta mangiando.

Bibliography

[1] E. Schrödinger, Math. Proc. Cambridge Philos. Soc. **31**, 555 (1935).

[2] A. Einstein, B. Podolsky, and N. Rosen, Physical Review **47**, 777 (1935).

[3] E. H. Lieb and D. W. Robinson, Commun. Math. Phys. **28**, 251 (1972).

[4] J. S. Bell, Physics **1**, 195 (1964).

[5] C. H. Bennett, G. Brassard, C. Crépeau, R. Jozsa, A. Peres, and W. K. Wootters, Phys. Rev. Lett. **70**, 1895 (1993).

[6] C. H. Bennett, D. P. DiVincenzo, J. A. Smolin, and W. K. Wootters, Phys. Rev. A **54**, 3824 (1996).

[7] M. B. Plenio and S. Virmani, Quant. Inf. Comp. **7**, 25 (2005).

[8] R. Horodecki, P. Horodecki, M. Horodecki, and K. Horodecki, Rev. Mod. Phys. **81**, 865 (2009).

[9] C. H. Bennett, D. P. DiVincenzo, C. A. Fuchs, T. Mor, E. Rains, P. W. Shor, J. A. Smolin, and W. K. Wootters, Phys. Rev. A **59**, 1070 (1999).

[10] E. M. Rains, Phys. Rev. A **60**, 173 (1999).

[11] E. Rains, IEEE Trans. Inf. Theory **47**, 2921 (2001).

[12] A. Peres, Phys. Rev. Lett. **77**, 1413 (1996).

[13] P. Horodecki, Phys. Lett. A **232**, 333 (1997).

[14] M. Horodecki, P. Horodecki, and R. Horodecki, Phys. Rev. Lett. **80**, 5239 (1998).

[15] C. Holzhey, F. Larsen, and F. Wilczek, Nucl. Phys. B **424**, 443 (1994).

[16] G. Vidal, J. Mod. Opt. **47**, 355 (2000).

[17] C. H. Bennett, H. J. Bernstein, S. Popescu, and B. Schumacher, Phys. Rev. A **53**, 2046 (1996).

[18] V. Vedral, M. B. Plenio, M. A. Rippin, and P. L. Knight, Phys. Rev. Lett. **78**, 2275 (1997).

[19] V. Vedral and M. B. Plenio, Phys. Rev. A **57**, 1619 (1998).

[20] M. A. Nielsen, Phys. Rev. Lett. **83**, 436 (1999).

[21] P. M. Hayden, M. Horodecki, and B. M. Terhal, J. Phys. A **34**, 6891 (2001).

[22] W. Wootters, Quant. Inf. Comp. **1**, 27 (2001).

[23] L. Amico, R. Fazio, A. Osterloh, and V. Vedral, Rev. Mod. Phys. **80**, 517 (2008).

[24] J. Eisert, M. Cramer, and M. B. Plenio, Rev. Mod. Phys. **82**, 277 (2010).

[25] P. Calabrese, J. Cardy, and B. Doyon, J. Phys. A **42**, 500301 (2009).

[26] E. H. Lieb and M. B. Ruskai, Phys. Rev. Lett. **30**, 434 (1973).

[27] E. H. Lieb, J. Math. Phys. **14**, 1938 (1973).

[28] A. Rényi, *Probability theory* (North-Holland, 1970).

[29] J. Eisert and M. B. Plenio, J. Mod. Opt. **46**, 145 (1999).

[30] K. Życzkowski, P. Horodecki, A. Sanpera, and M. Lewenstein, Phys. Rev. A **58**, 883 (1998).

[31] G. Vidal and R. F. Werner, Phys. Rev. A **65**, 032314 (2002).

[32] M. Horodecki, P. Horodecki, and R. Horodecki, Phys. Lett. A **223**, 1 (1996).

[33] R. Simon, Phys. Rev. Lett. **84**, 2726 (2000).

[34] M. B. Plenio, Phys. Rev. Lett. **95**, 090503 (2005).

[35] J. Lee, M. S. Kim, Y. J. Park, S. Lee, J. Mod. Opt. **47**, 2151 (2000).

[36] J. Eisert, "Entanglement in quantum information theory", PhD thesis (2001), arXiv:quant-ph/0610253.

[37] H. He and G. Vidal, Phys. Rev. A **91**, 012339 (2015).

[38] Y. C. Ou and H. Fan, Phys. Rev. A **75**, 062308 (2007).

[39] A. A. Belavin, A. M. Polyakov, and A. B. Zamolodchikov, Nucl. Phys. B **241**, 333 (1984).

[40] S. Sachdev, *Quantum phase transitions* (Cambridge University Press, 2001).

[41] P. Di Francesco, D. Sénéchal, and P. Mathieu, *Conformal field theory* (Springer, 1997).

[42] P. Ginsparg, *Applied Conformal Field Theory*, lecture notes, arXiv:hep-th/9108028, Les Houches, July 1988.

[43] I. T. Todorov, M. C. Mintchev, and V. B. Petkova, *Conformal invariance in quantum field theory* (Scuola normale superiore Pisa, 1978).

[44] P. Calabrese and A. Lefevre, Phys. Rev. A **78**, 032329 (2008).

[45] P. Calabrese and J. Cardy, J. Stat. Mech. P06002 (2004).

[46] P. Calabrese and J. Cardy, J. Phys. A **42**, 504005 (2009).

[47] B. Groisman, S. Popescu, and A. Winter, Phys. Rev. A **72**, 032317 (2005).

[48] M. Nielsen and I. Chuang, *Quantum Computation and Quantum Information* (Cambridge University Press, 2000).

[49] M. M. Wolf, F. Verstraete, M. B. Hastings, and J. I. Cirac, Phys. Rev. Lett. **100**, 070502 (2008).

[50] P. Ruggiero, V. Alba, and P. Calabrese, arXiv:1609.01287 (2016).

[51] L. Dixon, D. Friedan, E. Martinec, and S. Shenker, Nucl. Phys. B **282**, 13 (1987).

[52] A. Zamolodchikov, Nucl. Phys. B **285**, 481 (1987).

[53] L. Alvarez-Gaumé, G. Moore, and C. Vafa, Commun. Math. Phys. **106**, 1 (1986).

[54] E. Verlinde and H. Verlinde, Nucl. Phys. B **288**, 357 (1987).

[55] V. G. Knizhnik, Commun. Math. Phys. **112**, 567 (1987).

[56] M. Bershadsky and A. Radul, Int. J. Mod. Phys. A **02**, 165 (1987).

[57] R. Dijkgraaf, E. Verlinde, and H. Verlinde, Commun. Math. Phys. **115**, 649 (1988).

[58] L. Alvarez-Gaumé, J.-B. Bost, G. Moore, P. Nelson, and C. Vafa, Commun. Math. Phys. **112**, 503 (1987).

[59] J. D. Fay, *Theta Functions on Riemann Surfaces*, Vol. 352, Lecture Notes in Mathematics (Springer Berlin Heidelberg, 1973).

[60] D. Mumford, *Tata lectures on theta II*, Vol. 43 (Springer, 2007).

[61] J.-I. Igusa, *Theta Functions* (Springer Berlin Heidelberg, Berlin, Heidelberg, 1972).

[62] M. Caraglio and F. Gliozzi, JHEP **11** (2008) 076.

[63] S. Furukawa, V. Pasquier, and J. Shiraishi, Phys. Rev. Lett. **102**, 170602 (2009).

[64] V. Alba, L. Tagliacozzo, and P. Calabrese, Phys. Rev. B **81**, 060411 (2010).

[65] F. Gliozzi and L. Tagliacozzo, J. Stat. Mech. P01002 (2010).

[66] M. Fagotti and P. Calabrese, J. Stat. Mech. P04016 (2010).
[67] V. Alba, L. Tagliacozzo, and P. Calabrese, J. Stat. Mech. P06012 (2011).
[68] M. Fagotti, EPL **97**, 17007 (2012).
[69] M. A. Rajabpour and F. Gliozzi, J. Stat. Mech. P02016 (2012).
[70] P. Calabrese, J. Cardy, and E. Tonni, J. Stat. Mech. P11001 (2009).
[71] P. Calabrese, J. Cardy, and E. Tonni, J. Stat. Mech. P01021 (2011).
[72] H. Casini, C. D. Fosco, and M. Huerta, J. Stat. Mech. P07007 (2005).
[73] P. Calabrese, J. Stat. Mech. P09013 (2010).
[74] M. Headrick, Phys. Rev. D **82**, 126010 (2010).
[75] M. Headrick, A. Lawrence, and M. Roberts, J. Stat. Mech. P02022 (2013).
[76] B. Chen and J.-J. Zhang, JHEP **11** (2013) 164.
[77] S. Ryu and T. Takayanagi, Phys. Rev. Lett. **96**, 181602 (2006).
[78] S. Ryu and T. Takayanagi, JHEP **08** (2006) 045.
[79] T. Nishioka, S. Ryu, and T. Takayanagi, J. Phys. A **42**, 504008 (2009).
[80] V. E. Hubeny and M. Rangamani, JHEP **03** (2008) 006.
[81] E. Tonni, JHEP **05** (2011) 004.
[82] P. Hayden, M. Headrick, and A. Maloney, Phys. Rev. D **87**, 046003 (2013).
[83] T. Faulkner, arXiv:1303.7221 (2013).
[84] T. Hartman, arXiv :1303.6955 (2013).
[85] T. Faulkner, A. Lewkowycz, and J. Maldacena, JHEP **11** (2013) 074.
[86] P. Fonda, L. Giomi, A. Salvio, and E. Tonni, JHEP **02** (2014) 005.
[87] J. Cardy, J. Phys. A **46**, 285402 (2013).
[88] H. Casini and M. Huerta, JHEP **03** (2009) 048.
[89] H. Casini and M. Huerta, Class. Quant. Grav. **26**, 185005 (2009).
[90] N. Shiba, JHEP **07** (2012) 100.
[91] L. Y. Hung, R. C. Myers, M. Smolkin, and A. Yale, JHEP **12** (2011) 047.
[92] H. J. Schnitzer, arXiv:1406.1161 (2014).
[93] C. A. Agón, I. Cohen-Abbo, and H. J. Schnitzer, arXiv:1505.03757 (2015).
[94] A. Coser, L. Tagliacozzo, and E. Tonni, J. Stat. Mech. P01008 (2014).
[95] P. Calabrese, J. Cardy, and E. Tonni, Phys. Rev. Lett. **109**, 130502 (2012).
[96] P. Calabrese, J. Cardy, and E. Tonni, J. Stat. Mech. P02008 (2013).

[97] P. Calabrese, L. Tagliacozzo, and E. Tonni, J. Stat. Mech. P05002 (2013).

[98] V. Alba, J. Stat. Mech. P05013 (2013).

[99] A. Coser, E. Tonni, and P. Calabrese, J. Stat. Mech. P033116 (2016).

[100] A. Coser, E. Tonni, and P. Calabrese, J. Stat. Mech. P053109 (2016).

[101] C. Herzog and Y. Wang, J. Stat. Mech. P073102 (2016).

[102] P. Calabrese, J. Cardy, and E. Tonni, J. Phys. A **48**, 015006 (2015).

[103] V. Eisler and Z. Zimborás, New J. Phys. **17**, 53048 (2015).

[104] A. Coser, E. Tonni, and P. Calabrese, J. Stat. Mech. P08005 (2015).

[105] P. Chang and W. Xueda, Phys. Rev. B **93**, 195140 (2016).

[106] F. O. Blondeau, O. Castro-Alvaredo, and B. Doyon, J. Phys. A **49**, 125401 (2016).

[107] A. Coser, E. Tonni, and P. Calabrese, J. Stat. Mech. P12017 (2014).

[108] V. Eisler and Z. Zimborás, New J. Phys. **16**, 123020 (2014).

[109] M. Hoogeveen and B. Doyon, Nucl. Phys. B **898**, 78–112 (2015).

[110] X. Wen, P.-Y. Chang, and S. Ryu, Phys. Rev. B **92**, 075109 (2015).

[111] E. S. Sørensen, M.-S. Chang, N. Laflorencie, and I. Affleck, J. Stat. Mech. P08003 (2007).

[112] A. Bayat, P. Sodano, and S. Bose, Phys. Rev. B **81**, 064429 (2010).

[113] P. Sodano, A. Bayat, and S. Bose, Phys. Rev. B **81**, 100412 (2010).

[114] A. Bayat, S. Bose, P. Sodano, and H. Johannesson, Phys. Rev. Lett. **109**, 066403 (2012).

[115] H. Wichterich, J. Molina-Vilaplana, and S. Bose, Phys. Rev. A **80**, 010304 (2009).

[116] J. Anders and A. Winter, Quant. Inf. Comp. **8**, 10 (2007).

[117] J. Anders, Phys. Rev. A **77**, 062102 (2008).

[118] A. Ferraro, D. Cavalcanti, A. García-Saez, and A. Acín, Phys. Rev. Lett. **100**, 080502 (2008).

[119] D. Cavalcanti, A. Ferraro, A. García-Saez, and A. Acín, Phys. Rev. A **78**, 012335 (2008).

[120] H. Wichterich, J. Vidal, and S. Bose, Phys. Rev. A **81**, 032311 (2010).

[121] A. Bayat, S. Bose, and P. Sodano, Phys. Rev. Lett. **105**, 187204 (2010).

[122] C.-M. Chung, V. Alba, L. Bonnes, P. Chen, and A. M. Läuchli, Phys. Rev. B **90**, 064401 (2014).

[123] C. De Nobili, A. Coser, and E. Tonni, J. Stat. Mech. P06021 (2015).

[124] C. Castelnovo, Phys. Rev. A **88**, 042319 (2013).

[125] C. Castelnovo, Phys. Rev. A **89**, 042333 (2014).

[126] Y. A. Lee and G. Vidal, Phys. Rev. A **88**, 042318 (2013).

[127] R. A. Santos, V. Korepin, and S. Bose, Phys. Rev. A **84**, 062307 (2011).

[128] R. A. Santos and V. E. Korepin, J. Phys. A **45**, 125307 (2012).

[129] X. Wen, S. Matsuura, and S. Ryu, Phys. Rev. B **93**, 245140 (2016).

[130] V. Eisler and Z. Zimboras, Phys. Rev. B **93**, 115148 (2016).

[131] N. Sherman, T. Devakul, M. B. Hastings, and R. R. P. Singh, Phys. Rev. E **93**, 022128 (2016).

[132] M. Rangamani and M. Rota, JHEP **10** (2014) 060.

[133] M. Kulaxizi, A. Parnachev, and G. Policastro, JHEP **09** (2014) 010.

[134] L. Bombelli, R. K. Koul, J. Lee, and R. D. Sorkin, Phys. Rev. D **34**, 373 (1986).

[135] M. Srednicki, Phys. Rev. Lett. **71**, 666 (1993).

[136] C. Callan and F. Wilczek, Phys. Lett. B **333**, 55 (1994).

[137] M. B. Hastings, J. Stat. Mech. P08024 (2007).

[138] B.-Q. B.-Q. Jin and V. E. Korepin, J. Stat. Phys. **116**, 79 (2004).

[139] P. Calabrese, M. Campostrini, F. Essler, and B. Nienhuis, Phys. Rev. Lett. **104**, 095701 (2010).

[140] J. Cardy and P. Calabrese, J. Stat. Mech. P04023 (2010).

[141] J. Cardy, J. Stat. Mech. P10004 (2010).

[142] M. M. Wolf, Phys. Rev. Lett. **96**, 010404 (2006).

[143] H.-Q. Zhou, T. Barthel, J. O. Fjærestad, and U. Schollwöck, Phys. Rev. A **74**, 050305 (2006).

[144] D. Gioev and I. Klich, Phys. Rev. Lett. **96**, 100503 (2006).

[145] M. B. Plenio, J. Eisert, J. Dreißig, and M Cramer, Phys. Rev. Lett. **94**, 060503 (2005).

[146] E. Fradkin and J. E. Moore, Phys. Rev. Lett. **97**, 050404 (2006).

[147] H. Casini and M. Huerta, Nucl. Phys. B **764**, 183 (2007).

[148] L. Tagliacozzo, G. Evenbly, and G. Vidal, Phys. Rev. B **80**, 235127 (2009).

[149] B. Swingle, arXiv:1010.4038 (2010).

[150] A. B. Kallin, K. Hyatt, R. R. Singh, and R. G. Melko, Phys. Rev. Lett. **110**, 135702 (2013).

[151] A. B. Kallin, E. M. Stoudenmire, P. Fendlet, R. R. P. Singh, and R. G. Melko, J. Stat. Mech. P06009 (2014).

[152] J. Helmes and S. Wessel, Phys. Rev. B **89**, 245120 (2014).

[153] E. M. Stoudenmire, P. Gustainis, R. Johal, S. Wessel, and R. G. Melko, Phys. Rev. B **90**, 245106 (2014).

[154] P. Bueno, R. C. Myers, and W. W. Krempa, Phys. Rev. Lett. **115**, 021602 (2015).

[155] N. Laflorencie, D. J. Luitz, and F. Alet, Phys. Rev. B. **92**, 115126 (2015).

[156] P. Bueno and R. C. Myers, JHEP **1512** (2015) 168.

[157] P. Bueno and R. C. Myers, JHEP **1508** (2015) 068.

[158] P. Bueno, R. C. Myers, and W. W. Krempa, JHEP **1509** (2015) 091.

[159] S. Sahoo, E. M. Stoudenmire, J. M. Stephan, T. Devakul, R. R. P. Singh, and R. G. Melko, Phys. Rev. B **93**, 085120 (2016).

[160] J. Maldacena, Adv. Theor. Math. Phys. **2**, 231 (1998).

[161] M. Headrick and T. Takayanagi, Phys. Rev. D **76**, 106013 (2007).

[162] A. Lewkowycz and J. Maldacena, JHEP **08** (2013) 090.

[163] K. Brakke, *Surface Evolver*, http://www.susqu.edu/brakke/evolver/evolver.html.

[164] C. De Nobili, A. Coser, and E. Tonni, J. Stat. Mech. P083102 (2016).

[165] F. Iglói and I. Peschel, EPL **89**, 40001 (2010).

[166] F. C. Alcaraz, M. I. n. Berganza, and G. Sierra, Phys. Rev. Lett. **106**, 201601 (2011).

[167] M. Ibáñez Berganza, F. C. Alcaraz, and G. Sierra, J. Stat. Mech. P01016 (2012).

[168] L Taddia, J. C. Xavier, F. C. Alcaraz, and G Sierra, Phys. Rev. B **88**, 075112 (2013).

[169] F. H. L. Essler, A. M. Läuchli, and P. Calabrese, Phys. Rev. Lett. **110**, 115701 (2013).

[170] T Pálmai, Phys. Rev. B **90**, 161404 (2014).

[171] C. A. Agón, M. Headrick, D. L. Jafferis, and S. Kasko, Phys. Rev. D **89**, 025018 (2014).

[172] S. Marcovitch, A. Retzker, M. B. Plenio, and B. Reznik, Phys. Rev. A **80**, 012325 (2009).

[173] W. H. Press, S. A. Teukolsky, W. T. Vetterling, and B. P. Flannery, *Numerical recipes, 3rd edition. The art of scientific computing* (Cambridge University Press, 2007).

[174] J. L. Cardy, O. A. Castro-Alvaredo, and B. Doyon, J. Stat. Phys. **130**, 129 (2007).

[175] T. Giamarchi, *Quantum physics in one dimension* (Oxford University Press, New York, 2004).

[176] I. Peschel and M.-C. Chung, J. Phys. A **32**, 8419 (1999).

[177] K. Audenaert, J. Eisert, M. B. Plenio, and R. F. Werner, Phys. Rev. A **66**, 042327 (2002).

[178] I. Peschel, J. Phys. A **36**, L205 (2003).

[179] A. Botero and B. Reznik, Phys. Rev. A **70**, 052329 (2004).

[180] M. Cramer, J. Eisert, M. B. Plenio, and J. Dreißig, Phys. Rev. A **73**, 012309 (2006).

[181] I. Peschel and V. Eisler, J. Phys. A **42**, 504003 (2009).

[182] P. Calabrese and F. H. L. Essler, J. Stat. Mech. P08029 (2010).

[183] R. Sorkin, *10th Int. Conf. on General Relativity and Gravitation (Padova, 4-9 July 1983) vol II, p734 (contributed paper)*, talk at KITP Conference "Closing the Entanglement Gap", 2015.

[184] T. Barthel, M. Chung, and U. Schollwoeck, Phys. Rev. A **74**, 022329 (2006).

[185] M. Huerta, Phys. Rev. B **710**, 691 (2012).

[186] G. Vidal, J. I. Latorre, E. Rico, and A. Kitaev, Phys. Rev. Lett. **90**, 227902 (2003).

[187] J. I. Latorre, E. Rico, and G. Vidal, Quant. Inf. Comp. **4**, 26 (2003).

[188] H. Casini, M. Huerta, and L. Leitao, Nucl. Phys. B **814**, 594 (2009).

[189] H. Casini and M. Huerta, J. Phys. A **42**, 504007 (2009).

[190] S. Humeniuk and T. Roscilde, Phys. Rev. B **86**, 235116 (2012).

[191] J. Stéphan, S. Furukawa, G. Misguich, and V. Pasquier, Phys. Rev. B **80**, 184421 (2009).

[192] R. Singh, R. Melko, and J. Otimaa, Phys. Rev. B **86**, 075106 (2012).

[193] T. Devakul and R. Singh, Phys. Rev. B **90**, 064424 (2014).

[194] N. Drukker, D. Gross, and H. Ooguri, Phys. Rev. D **60**, 125006 (1999).

[195] T. Hirata and T. Takayanagi, JHEP **02** (2007) 042.

[196] P. Fonda, D. Seminara, and E. Tonni, JHEP **12** (2015) 037.

[197] H. Casini, M. Huerta, R. C. Myers, and A. Yale, arXiv:1506.06195 (2015).

[198] J. Cardy, *Closing the entanglement gap: Quantum information, quantum matter and quantum fields,* talk at KITP Conference "Closing the Entanglement Gap", 2015.

[199] B. Swingle, arXiv:1209.3304 (2013).

[200] P. Bueno and W. Witczak-Krempa, Phys. Rev. B **93**, 045131 (2016).

[201] Y. Chen and G. Vidal, J. Stat. Mech. P10011 (2014).

[202] I. Frérot and T. Roscilde, Phys. Rev. B **92**, 115129 (2015).

[203] A. Botero and B. Reznik, Phys. Lett. A **67**, 052311 (2003).

[204] A. Botero and B. Reznik, Phys. Lett. A **331**, 39 (2004).

[205] J. Williamson, American Journal of Mathematics **58**, 141 (1936).

[206] H. Casini, M. Huerta, and R. C. Myers, JHEP **05** (2011) 036.

[207] G. Wong, I. Klich, L. A. P. Zayas, and D. Vaman, JHEP **12** (2013) 020.

[208] P. Ruggiero, V. Alba, and P. Calabrese, arXiv:1607.02992 (2016).

[209] M. P. Zaletel, J. H. Bardarson, and J. E. Moore, Phys. Rev. Lett. **107**, 020402 (2011).

[210] A. Chandran, V. Khemani, and S. L. Sondhi, Phys. Rev. Lett. **113**, 060501 (2014).

[211] G. Vidal, Phys. Rev. Lett. **99**, 220405 (2007).

[212] G. Vidal, "Entanglement Renormalization: an introduction", in *Understanding quantum phase transitions* (Lincoln D. Carr (Taylor and Francis, Boca Raton, 2010, 2009), pp. 1–24.

[213] G. Evenbly and G. Vidal, J. Stat. Phys. **145**, 891 (2011).

[214] S. Singh and G. Vidal, Phys. Rev. B **88**, 121108 (2013).

[215] R. N. C. Pfeifer, G. Evenbly, and G. Vidal, Phys. Rev. A **79**, 040301 (2009).

[216] G. Evenbly and G. Vidal, "Quantum Criticality with the Multi-scale Entanglement Renormalization Ansatz", in *Strongly correlated systems*, Vol. 176 (Springer, 2013), pp. 99–130.

[217] J. Molina-Vilaplana and P. Sodano, JHEP **10** (2011) 011.

[218] E. Perlmutter, M. Rangamani, and M. Rota, arXiv:1506.01679 (2015).

[219] N. Shiba, JHEP **12** (2014) 152.